

UCSF

UC San Francisco Electronic Theses and Dissertations

Title

Dissecting cortical astrocyte network dynamics using all-optical approaches

Permalink

<https://escholarship.org/uc/item/82b6m0m5>

Author

Cahill, Michelle Kimberly

Publication Date

2023

Peer reviewed|Thesis/dissertation

Dissecting cortical astrocyte network dynamics using all-optical approaches

by
Michelle Kimberly Cahill

DISSERTATION
Submitted in partial satisfaction of the requirements for degree of
DOCTOR OF PHILOSOPHY

in
Neuroscience

in the
GRADUATE DIVISION
of the
UNIVERSITY OF CALIFORNIA, SAN FRANCISCO

Approved:

DocuSigned by:

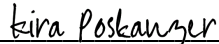


A996F2A5C1214BE...

Kevin Bender

Chair

DocuSigned by:



DocuSigned by: 496...

Kira Poskanzer



DocuSigned by: 405...

Felice Dunn



DocuSigned by: 4AF406E430B7472...

Massimo Scanziani

Committee Members

Copyright 2023

by

Michelle Kimberly Cahill

Dedication

In loving memory of my dad, James “Slater” Cahill

Acknowledgements

Getting my PhD has been a long and winding road, and there are many people I would like to thank for their guidance and support over the past seven years. First and foremost, I would like to thank Kira Poskanzer, my PhD advisor and mentor. It has been an absolute joy and privilege to work with and learn from you. You are a brilliant, resourceful scientist who is bold, and seemingly fearless, in your scientific pursuits. Thank you for teaching me how to engage with data, especially when results were unexpected and surprising, for coaching me to be a better writer and figure maker and for creating a lab environment in which every idea and perspective was valued. Above all, thank you for being an incredibly kind and empathetic mentor. So much life happens in the time it takes to get a PhD, and you have been there, responding with thoughtfulness and compassion, every step of the way. I hope to pay this forward one day; I will strive to mentor with as much intention, understanding and dedication as you have shown me these past seven years.

Thank you to my qualifying exam and thesis committee members, Kevin Bender, Felice Dunn, Massimo Scanziani, Anna Molofsky and Susan Voglmaier. Thank you for your scientific guidance in shaping and re-shaping my project at critical points during this process. Thank you to my NSF grant writing mentors, Felice Dunn and Holly Ingraham. Thank you for your insights on crafting a compelling, cohesive proposal and for the countless drafts you both edited. Thank you to my rotation mentors, Jeanne Paz, Dev Manoli and Eric Ullian. Thank you for welcoming me into your labs and shaping my first year of grad school. Finally, thank you to Eric Huang, my mentor before I began grad school. Eric, you were instrumental in preparing me for this endeavor, and without you, I don't think I'd be where I am today. Thank you for giving me so

many opportunities at the very beginning of my scientific career, from advocating for me to speak at conferences to giving me the opportunity write and review papers with you. Thank you for kindling my interest in glia and for your continued guidance as I navigated my PhD.

Thank you to our Neuroscience Graduate Program administrators, Pat Veitch and Lucita Nacionales. Thank you for all that you do for our program, for always answering emails quickly and thoroughly, and for knowing who to contact at UCSF for almost anything.

Thank you to all members of the Poskanzer Lab, both present and past. To Max Collard, thank you for your collaboration and analytical rigor over the past few years. Your analysis on the GABA/glutamate uncaging project made the work significantly stronger and more interesting. To Charlotte Taylor and Drew Willoughby, thank you for the great discussion you bring to lab meeting, the critical eye you bring to data and the calmness, stability and humor you both bring to lab. Thank you to Vincent Tse for sectioning and staining so many mouse brains and for always being game to create and implement new analysis techniques in Fiji. To our other lab technicians, Sae Yokoyama, Gregory Chin, Nicole DelRosso, Cameron Holman, Cass Gastelum and Nicole Werner, thank you for piloting new techniques, keeping the lab running smoothly and taking such good care of our mouse colony. To Michael Reitman, thank you for the great discussions in lab that helped me see how my data fit into the bigger picture. To Caitlin Durkee, thank you for your wealth of astrocyte knowledge and the positive, can-do attitude you brought to the bench. To Alba Peinado, thank you for patiently teaching me about optics, for exemplifying what it means to be a meticulous, careful problem solver and for chatting on countless runs and walks. To Silvia Pittolo, thank you for troubleshooting all things slice-related with me, for teaching me about pharmacology and for all of the discussions that sparked new experiments and analysis. Finally, to Trisha Vaidyanathan, thank you so much for your scientific

guidance, reassurance and friendship throughout my time in the Poskanzer Lab. Whenever I didn't know what to do during grad school, I just turned to you and followed your example, so thank you for paving the way. Alba, Silvia and Trisha, I feel so fortunate to have you as my role models. Thank you for making my time in lab such a joy.

Thank you to the class of 2016 and the graduate students of the Neuroscience program. To Anna Lipkin, thank you for believing in me in times when I didn't believe in myself. I'm inspired by your love for and commitment to science. To Victoria Turner, David Taylor, Marc Turner, Hannah Graham, and Anna Lipkin, thank you for your comradery and friendship throughout grad school. To the graduate students in the classes above us, specifically, Stephanie Holden, Lindsay Osso, Stefan Lemke, Leah Dorman, Selin Schamiloglu, Match McGregor, Frances Cho, and Trisha Vaidyanathan, thank you for making our graduate program such a warm and welcoming place.

I would also like to thank my support system that extends far beyond UCSF. To Katie Mowris, thank you for your fierce friendship and support over the past 20+ years. To the Pires family, Tony, Wendy, Caroline and Tom, thank you for welcoming me into your family, for cheering me on and for providing scientific guidance and advice whenever I've asked for it. To my extended family, both near and far, thank you for your steady support and for always being interested in my academic pursuits. I would specifically like to thank my great aunt, Beverly Faye Wu. Thank you for getting together for lunch and dinner every few month over the past 12 years. Catching up with you always brightens my day.

To my brother Chris Cahill, thank you for shaping me into the person I am today. From you I have learned to tackle problems, to be resilient and to be a fierce competitor. To my sister-in-law, Ashley Keeley, thank you for being incredibly kind and always showing up when it

counts the most. Finally, to my mom and dad, Eloise Shoong-Cahill and Slater Cahill, thank you for being my biggest supporters and cheerleaders. You have always stood behind me, lifting me up during the lows and celebrating with me during the highs. I cannot thank you enough for all of your unconditional love and support. Dad, I wish you were here to celebrate this milestone with us, but I carry you with me in everything I do.

Last, but certainly not least, to my fiancé Chris Pires, thank you for everything that you do to brighten my life. Thank you for helping me to keep everything in perspective when things haven't gone according to plan and for pushing me when I've been stuck. Thank you for celebrating all of the milestones, big and small, that make up this process and for bringing humor and lightness to our lives every day. I'm so lucky to have you by my side. I love you.

Contributions

Chapter 1 is written by Michelle K. Cahill.

Chapter 2 is reproduced in entirety, with the exception of a few excluded sections, from:

Wang, Y., DelRosso, N.V., Vaidyanathan, T.V., Cahill, M.K., Reitman, M.E., Pittolo, S., Mi, X., Yu, G., Poskanzer, K.E., Accurate quantification of astrocyte and neurotransmitter fluorescence dynamics for single-cell and population-level physiology, Nature Neuroscience, 22 (11) (2019), 1936–1944. <https://doi.org/10.1038/s41593-019-0492-2>.

K.E.P and G.Y. conceived and designed the study. Y.W. and G.Y. designed and implemented the AQUA algorithm, software, and simulations. N.V.D. analyzed all imaging data and provided critical conceptual input to software design. T.V. carried out GluSnFR experiments; M.K.C. performed *ex vivo* Ca²⁺, GABASnFR, and GluSnFR experiments; M.R. performed *in vivo* Ca²⁺ imaging experiments; and S.P. performed GRAB-NE experiments. X.M. implemented the Java version of the software, and built and tested the 3D prototype. K.E.P supervised the experimental team. G.Y. supervised the computational team. Y.W., N.V.D., K.E.P, and G.Y. wrote the manuscript with input from all authors.

Chapter 3 is reproduced in entirety from the following article, currently in revision:

Cahill, M.K., Collard, M., Tse, V., Reitman, M.E., Etchenique, R., Kirst, C., Poskanzer, K.E., Network-level encoding of local neurotransmitters in cortical astrocytes, bioRxiv. (2023). <https://doi.org/10.1101/2023.12.01.568932>.

M.K.C. and K.E.P. conceptualized the project and designed the experiments. M.K.C. performed all *ex vivo* imaging experiments. K.E.P., M.K.C., and M.C. conceptualized the data analysis, and M.K.C. and M.C. performed data analysis with assistance from C.K. V.T. performed IHC, confocal imaging, and related fixed tissue image analysis. M.E.R. performed *in vivo* 2P experiments and related image analysis. R.E. helped with resources related to photoactivatable compounds. M.K.C. and K.E.P. wrote the initial draft, and edited and revised the paper. M.C. contributed to writing the initial draft of the paper and subsequent versions. K.E.P. supervised the research.

Chapter 4 is reproduced in entirety from:

Cahill, M.K., Perez, Y.R., Larphaveesarp, A., Etchenique, R., Poskanzer, K.E., A photoactivatable norepinephrine for probing adrenergic neural circuits, bioRxiv, (2023). <https://doi.org/10.1101/2023.11.13.566764>.

K.E.P. and R.E. conceptualized the project and designed the experiments. Y.R.P. and R.E. synthesized the chemical compound. M.K.C. performed the electrophysiology and photoactivation experiments, and A.L. prepared the acute slices containing locus coeruleus. M.K.C. performed the data analysis, with supervision from K.E.P. M.K.C. and K.E.P. wrote the initial draft, and edited and revised the paper. R.E. contributed to writing the initial draft of the paper and subsequent versions. K.E.P. and R.E. supervised the research.

Dissecting cortical astrocyte network dynamics using all-optical approaches

Michelle Kimberly Cahill

Abstract

Astrocytes—the most abundant non-neuronal cell type in the mammalian brain—are integral circuit components that respond to and modulate neuronal activity. While astrocytes are electrically silent, they display highly dynamic intracellular Ca^{2+} activity. As such, measuring Ca^{2+} dynamics has become the primary method for studying astrocyte physiology. Astrocyte Ca^{2+} activity is highly heterogeneous and occurs across multiple spatiotemporal scales: from fast, subcellular activity to slow, synchronized activity that percolates across connected astrocyte networks. Additionally, astrocyte network Ca^{2+} activity influences a wide range of processes including sleep-wake dynamics, decision making and motor learning. While astrocyte network activity has important implications for neuronal circuit function, it remains unclear if particular neurotransmitter inputs contribute to specific aspects of astrocyte network activity. The primary focus of this dissertation is to investigate input-response dynamics in cortical astrocytes, linking specific neurotransmitter or neuromodulatory inputs to specific astrocyte Ca^{2+} activity. In Chapter 2, we introduce a new analysis software, AQuA, to accurately quantify heterogeneous Ca^{2+} activity, which is essential for studying the nuances of astrocyte responses to different inputs. In Chapter 3, we use two-photon Ca^{2+} imaging of astrocytes while mimicking neurotransmitter inputs. We find that brief, subcellular inputs of GABA and glutamate lead to widespread, long-lasting Ca^{2+} responses within a connected astrocyte network. Further, we find that propagative events differentiate astrocyte network responses to these two major neurotransmitters. In Chapter 4, we expand our toolkit for probing input-response dynamics by

introducing a new photoactivatable compound for the release of the neuromodulator norepinephrine. Together, our results demonstrate that local, transient neurotransmitter inputs are encoded by broad cortical astrocyte networks over the course of minutes, contributing to accumulating evidence that significant astrocyte-neuron communication occurs across slow, network-level spatiotemporal scales.

Table of Contents

<i>Chapter 1: Introduction</i>	1
A defined framework for input-response dynamics in neurons	1
A brief history of glia	2
Astrocyte form and function	2
Input-response dynamics in cortical astrocytes	5
Expanding the toolkit for probing astrocyte responses to inputs	6
References	8
<i>Chapter 2: Accurate quantification of astrocyte and neurotransmitter fluorescence dynamics for single-cell and population-level physiology</i>	15
Abstract	15
Introduction.....	15
Results.....	18
Discussion	31
Methods.....	35
Figures.....	49
References.....	72
<i>Chapter 3: Network-level encoding of local neurotransmitters in cortical astrocytes</i>	76
Abstract	76
Introduction.....	77
Results.....	78
Discussion	87
Methods.....	89

Figures.....	112
Tables	133
References.....	154
<i>Chapter 4: A photoactivatable norepinephrine for probing adrenergic neural circuits</i>	162
Abstract.....	162
Introduction.....	163
Results.....	165
Discussion.....	168
Methods.....	169
Figures.....	172
References.....	174

List of Figures

Chapter 2:

Figure 2.1. AQuA-based event detection.	49
Figure 2.2. Performance comparison among image-analysis methods.....	51
Figure 2.3. AQuA features capture heterogeneities among single astrocytes.....	53
Figure 2.4. AQuA resolves astrocytic Ca^{2+} propagation directionality across scales.	54
Figure 2.5. AQuA-based detection of extracellular dynamics via astrocytic and neuronal expression of genetically encoded neurotransmitter sensors.	56
Extended Data Figure 2.1: Eight steps in the AQuA algorithm.	57
Extended Data Figure 2.2: Schematic illustration of three major modules in AQuA algorithm.....	58
Extended Data Figure 2.3: Limitations of thresholding-based analysis.....	60
Extended Data Figure 2.4: AQuA detects ground truth events across three types of simulated data.	62
Extended Data Figure 2.5: Event counts under different SNRs.....	63
Extended Data Figure 2.6: Peer method performance on growing and moving propagation types.....	64
Extended Data Figure 2.7: AQuA features enable detailed Ca^{2+} activity plots.....	65
Extended Data Figure 2.8: Distribution of Ca^{2+} event features.	67
Extended Data Figure 2.9: Cluster analysis on features generated from three spatial footprint methods.....	68
Extended Data Figure 2.10: Defining Ca^{2+} bursts.	69

Extended Data Figure 2.11: Comparison of AQuA and Caltracer for event detection of astrocytic GluSnFR signals..... 70

Extended Data Figure 2.12: AQuA performance on simulated 3D datasets. 71

Chapter 3:

Figure 3.1. Direct GABAergic and glutamatergic receptor activation drive distinct astrocyte Ca²⁺ activity..... 112

Figure 3.2. Subcellular, spatiotemporally restricted release of NTs increases Ca²⁺ activity within directly stimulated astrocytes. 113

Figure 3.3. Subcellular release of GABA and glutamate increases Ca²⁺ activity in the local astrocyte network via Cx43..... 115

Figure 3.4. Propagative activity distinguishes astrocyte network responses to GABA and glutamate..... 117

Extended Data Figure 3.1: Different responses to activation of astrocytic glutamatergic and GABAergic receptors via pharmacological bath-application. 119

Extended Data Figure 3.2: Characterization of, and controls for, increased Ca²⁺ activity in astrocytes directly stimulated by NT uncaging..... 122

Extended Data Figure 3.3: Confirmation of Cx43 knockdown and network-level controls after NT uncaging. 124

Extended Data Figure 3.4: Change in individual astrocyte Ca²⁺ event features post NT-uncaging..... 126

Extended Data Figure 3.5: Validating changes in propagative event activity following NT-uncaging 127

Extended Data Figure 3.6: Static activity changes in the local astrocyte network are similar in response to GABA and glutamate.....	130
Extended Data Figure 3.7: Individual neighboring astrocytes exhibit variable Ca ²⁺ responses across multiple rounds of glutamate uncaging.....	131
Chapter 4:	
Figure 4.1: Photorelease of RuBi-NE specifically increases local [NE].	172

List of Tables

Chapter 2:

Extended Data Table 2.1. Parameter setting for AQUA	43
---	----

Chapter 3:

Extended Data Table 3.1. Statistics for Fig. 3.1c.....	133
Extended Data Table 3.2. Statistics for Fig. 3.1e–h.....	134
Extended Data Table 3.3. Statistics for Extended Data Fig. 3.1d.....	135
Extended Data Table 3.4. Statistics for Extended Data Fig. 3.1g.....	136
Extended Data Table 3.5. Statistics for Extended Data Fig. 3.2b.....	137
Extended Data Table 3.6. Statistics for Fig. 3.3h.....	138
Extended Data Table 3.7. Statistics for Extended Data Fig. 3.3g, h.....	139
Extended Data Table 3.8. Statistics for Fig. 3.4b.....	140
Extended Data Table 3.9. N for Fig. 3.4f, h, j, k and Extended Data Fig. 3.6.....	141
Extended Data Table 3.10. Statistics for Fig. 3.4f, j and Extended Data Fig. 3.6b–c.....	142
Extended Data Table 3.11. N for Fig. 3.4m	144
Extended Data Table 3.12. Statistics for Extended Data Fig. 3.4a	145
Extended Data Table 3.13. Statistics for Extended Data Fig. 3.4b.....	148
Extended Data Table 3.14. Statistics for Extended Data Fig. 3.7d.....	151

Chapter 1:

Introduction

A defined framework for input-response dynamics in neurons

A set of defined rules governing neuronal input-output relationships is a cornerstone of neuroscience. Given a specific excitatory or inhibitory neurotransmitter (NT) input, post-synaptic membrane potential changes that lead to action potentials can be accurately predicted. Synaptic release of glutamate, the major excitatory neurotransmitter in the central nervous system (CNS), leads to neuronal depolarization, while synaptic release of γ -aminobutyric acid (GABA), the major inhibitory neurotransmitter in the CNS, leads to neuronal hyperpolarization. These inputs, causing subthreshold depolarization and hyperpolarization, sum over specific time periods and spatial territories to shape the activity of individual cells. If the membrane potential reaches a certain depolarized threshold, the neuron will fire an action potential, relaying the received signal onto other neurons in the circuit via release of neurotransmitters. This framework of input-response dynamics in neurons lays out how different scales of activity, from subcellular synaptic activity to population-level neuronal network activity, are linked to one another, and it forms a foundation for understanding how the brain functions. However, neurons are not the only cell type in the nervous system that sense neurotransmitters. Glia, a diverse class of non-neuronal cells in the CNS, express numerous receptors for neurotransmitters and neuromodulators¹⁻⁴. Yet, the set of rules governing input-response relationships in glia is poorly defined.

A brief history of glia

In 1856, the pathologist Rudolph Virchow used the term *neuroglia* to describe the tissue that exists between neuronal cells. Virchow wrote, “This connective substance forms a sort of cement (neuroglia) in the brain, spinal cord, and higher sensory nerves, in which the nervous elements are embedded.”³ Over the subsequent decades, careful observation of CNS tissue from multiple organisms led to the understanding that neuroglia tissue is made up of multiple cell types with distinct morphologies³. The most abundant of these glial cell types in the mammalian brain are astrocytes, which were first drawn by Otto Deiters in a manuscript published in 1865. The characteristic star-shape of these cells, with numerous fine branches or processes radiating out from a cell body, earned these cells the name *astrocyte*, coined by Michael von Lenhossek in 1893³. While observation of unstained and stained tissue led to an initial understanding of astrocyte morphology, the function of these cells remained elusive⁵, and the idea, that glia were simply the “cement” or “glue” passively holding neurons in place, persisted.

Astrocyte form and function

Since astrocytes were first observed over 150 years ago, much has been learned about their multitude of functions, which map onto their unique morphology. Advances in microscopy and techniques to label cells have revealed that astrocytes have a highly complex structure^{6–10}, consisting of many fine branches that are in close contact with synapses^{6,11}. Further, it’s estimated that an individual astrocyte contacts > 100,000 synapses⁷ and individual astrocytes are physically connected to one another via gap junctions¹², tiling the entire CNS^{7,13}. As such, astrocytes are well-positioned to regulate neuronal activity across multiple spatial scales.

Indeed, astrocytes respond to and modulate neuronal activity via increases in intracellular calcium (Ca^{2+}). Many neurotransmitters and neuromodulators, including glutamate^{14,15}, GABA^{16–18}, norepinephrine^{19–22}, dopamine²³ and histamine²⁴, act on G-protein coupled receptors (GPCRs) expressed by astrocytes^{1,2} to mobilize intracellular Ca^{2+} via release from internal stores, such as the endoplasmic reticulum. Astrocyte Ca^{2+} dynamics are highly heterogeneous²⁵, spanning multiple spatiotemporal scales. Spatially, astrocyte Ca^{2+} activity has been observed at the level of subcellular compartments confined to regions $\sim 1\mu\text{m}$ ^{210,15,26–28}, at the level of individual cells, $\sim 50\mu\text{m}$ in diameter^{23,25}, and at the level of astrocyte networks, extending hundreds of microns^{19,20,29–31}. Temporally, astrocyte activity has been shown to occur over the timeframe of milliseconds^{27,28}, seconds^{27,28,30,31}, and minutes^{18,30}. In addition to varying in area and duration, astrocyte Ca^{2+} events also vary in their degree of propagation. Some Ca^{2+} events are static, staying in a single location, while other events propagate within or between cells²⁵, traveling along the reticular meshwork of fine astrocyte processes¹⁰.

This heterogeneous Ca^{2+} activity has been linked to a wide range of functions that modulate synaptic activity. One critical function of astrocytes is removal of excess neurotransmitter from the synaptic cleft via transporter uptake^{32,33}. The trafficking of neurotransmitter transporters into and away from the astrocyte membrane is Ca^{2+} dependent³⁴ and crucial for tight temporal control of synaptic transmission. Another Ca^{2+} dependent function of astrocytes is maintenance of extracellular ion concentrations^{35–37}, primarily regulation of extracellular potassium (K^+). Astrocytes rapidly uptake extracellular K^+ via inward rectifying K^+ channels^{38,39} and the activity of the Na^+ , K^+ -ATPase³⁷. The resulting decrease in extracellular K^+ leads to neuronal hyperpolarization and decreased synaptic activity³⁷. In addition to regulating extracellular neurotransmitter and ion concentrations, astrocyte Ca^{2+} signaling is linked to release

or modulation of “gliotransmitters” such as glutamate^{40,41}, ATP/adenosine^{15,16} and D-serine^{42,43}. Depending on the gliotransmitter released and the site of action, these outputs can either facilitate^{15,41,43} or inhibit^{16,40} synaptic activity.

Because astrocytes contact many thousands of synapses and astrocyte Ca^{2+} activity spans multiple spatial scales, astrocyte Ca^{2+} activity not only modulates individual synapses, but also modulates the activity of large ensembles of neurons. Population-level astrocyte Ca^{2+} activity is important for shifting neuronal circuit activity into a synchronized state^{44,45}. As such, astrocyte Ca^{2+} activity is involved in regulating sleep-wake dynamics^{46,47} and in resynchronizing neuronal activity after periods of high arousal²².

While increases in astrocyte Ca^{2+} activity have been linked to this myriad of diverse, and sometimes opposing, functions, how the same second messenger triggers distinct functional outputs in response to different inputs remains unknown. One intriguing possibility is that there is an astrocyte Ca^{2+} code, in which specific spatiotemporal patterns of Ca^{2+} activity link specific inputs to functional outputs. Until recently, it was difficult to explore this possibility because the astrocyte field did not have a good way to quantify complex Ca^{2+} dynamics. Most analysis methods took a region-of-interest (ROI) based approach, measuring Ca^{2+} fluctuations from static, pre-determined regions^{18,19,28,30}. These ROI-based analysis methods pool together all Ca^{2+} activity within a defined region regardless of the different sizes of Ca^{2+} events or how they move within and beyond an individual ROI. In Chapter 2, we introduce a new analysis software package, AQuA, for quantifying astrocyte Ca^{2+} activity and heterogeneous fluorescent signals, more broadly²⁵. We apply probability theory, machine learning and computational optimization to develop an algorithm which detects Ca^{2+} activity as discrete events and records biologically relevant spatiotemporal features of each event, independent of ROIs. This analysis software is a

publicly available tool, with user-friendly interfaces in both MATLAB and Fiji, that is now widely used to dissect astrocyte Ca^{2+} dynamics both *ex vivo* and *in vivo*, moving the field one step closer to understanding the complex astrocyte Ca^{2+} code.

Input-response dynamics in cortical astrocytes

Accurate quantification of astrocyte Ca^{2+} activity via AQuA is central to the work presented in Chapter 3, where we investigate input-response dynamics in cortical astrocytes. Our goal here was to build an input framework governing transient and sustained cortical astrocyte Ca^{2+} activity at three spatial scales: subcellular, single cell and network. Because the majority of cortical neurons release either glutamate or GABA, we took a physiologically relevant and comparative approach, focusing on astrocyte responses to these two major neurotransmitters. We use *ex vivo* and *in vivo* two-photon (2P) Ca^{2+} imaging of astrocytes while mimicking neuronal neurotransmitter inputs at multiple spatiotemporal scales.

To mimic subcellular neurotransmitter inputs, we use 2P photo-release (“uncaging”) of caged neurotransmitter^{15,48–53}. We utilized a class of caged compounds (with ruthenium bipyridine [RuBi] backbones), bound to either GABA^{54,55} or glutamate^{55,56}. In the bound form, the neurotransmitter cannot bind to receptors, and is thus, not biologically active. Upon exposure to one-photon (1P) blue light (446–486 nm) or the equivalent 2P wavelength (800nm), neurotransmitter is released from the RuBi backbone, free to bind to receptors. The spatiotemporal dynamics of neurotransmitter uncaging can be tuned by the size, intensity and duration of the light beam. Additionally, neurotransmitter can be released in this manner without mechanically disturbing the tissue, which itself can modulate cellular activity⁵⁷.

Using 2P uncaging of RuBi-GABA and RuBi-glutamate, we are able to stimulate the same subcellular location of individual astrocytes with each neurotransmitter, in sequence. With this strategy, the imaging/uncaging paradigm is the same for both GABA and glutamate. This comparative approach allows us to record activity changes that are common to both neurotransmitter inputs, as well as activity changes that are unique to each input, as we observe how activity changes both within the directly stimulated astrocyte and within the connected astrocyte network. Our results link specific excitatory and inhibitory neurotransmitter inputs to specific astrocyte Ca^{2+} activity and map the scales over which astrocytes could exert effects on neuronal circuitry.

Expanding the toolkit for probing astrocyte responses to inputs

As discussed in the previous section, the light-activatable RuBi compounds were central to probing input-response dynamics in cortical astrocytes in Chapter 3. Crucially, the uncaging properties for GABA and glutamate are comparable, as both neurotransmitters are caged by a common chemical backbone. The suite of RuBi-compounds bound to neurotransmitters extends beyond GABA and glutamate and includes serotonin⁵⁸, dopamine⁵⁹ and nicotine⁶⁰. In Chapter 4, we introduce the addition of norepinephrine to the list of neurotransmitters and neuromodulators bound to a RuBi backbone. We describe the synthesis and chemical properties of RuBi-norepinephrine (RuBi-NE) and validate the 1P release of norepinephrine using whole-cell patch clamp electrophysiology in acute mouse brain slices. Because astrocyte network Ca^{2+} dynamics are largely influenced by the neuromodulator norepinephrine^{19,20,22,61}, this photoactivatable compound will likely prove useful for further dissection of astrocyte physiology. Probing astrocyte responses to multiple neuromodulators, as was done in response to GABA and

glutamate, will further develop the framework for input-response dynamics in astrocytes, which could help build a consistent model for astrocytic modulation of neuronal activity.

References

1. Farhy-Tselnicker, I. *et al.* Activity-dependent modulation of synapse-regulating genes in astrocytes. *eLife* **10**, (2021).
2. Srinivasan, R. *et al.* New transgenic mouse lines for selectively targeting astrocytes and studying calcium signals in astrocyte processes in situ and in vivo. *Neuron* **92**, 1181–1195 (2016).
3. *Neuroglia*. (Oxford University Press, 2004).
doi:10.1093/acprof:oso/9780195152227.001.0001.
4. Porter, J. T. & McCarthy, K. D. Astrocytic neurotransmitter receptors in situ and in vivo. *Prog. Neurobiol.* **51**, 439–455 (1997).
5. Ramón y Cajal, S. *Histologie de systeme nerveux de l’homme et des vertebrae*. (1911).
6. Grosche, J. *et al.* Microdomains for neuron-glia interaction: parallel fiber signaling to Bergmann glial cells. *Nat. Neurosci.* **2**, 139–143 (1999).
7. Bushong, E. A., Martone, M. E., Jones, Y. Z. & Ellisman, M. H. Protoplasmic astrocytes in CA1 stratum radiatum occupy separate anatomical domains. *J. Neurosci.* **22**, 183–192 (2002).
8. Bushong, E. A., Martone, M. E. & Ellisman, M. H. Maturation of astrocyte morphology and the establishment of astrocyte domains during postnatal hippocampal development. *Int. J. Dev. Neurosci.* **22**, 73–86 (2004).
9. Wilhelmsson, U. *et al.* Redefining the concept of reactive astrocytes as cells that remain within their unique domains upon reaction to injury. *Proc Natl Acad Sci USA* **103**, 17513–17518 (2006).

10. Arizono, M. *et al.* Structural basis of astrocytic Ca²⁺ signals at tripartite synapses. *Nat. Commun.* **11**, 1906 (2020).
11. Witcher, M. R., Kirov, S. A. & Harris, K. M. Plasticity of perisynaptic astroglia during synaptogenesis in the mature rat hippocampus. *Glia* **55**, 13–23 (2007).
12. Pannasch, U. *et al.* Astroglial networks scale synaptic activity and plasticity. *Proc Natl Acad Sci USA* **108**, 8467–8472 (2011).
13. Livet, J. *et al.* Transgenic strategies for combinatorial expression of fluorescent proteins in the nervous system. *Nature* **450**, 56–62 (2007).
14. Tang, W. *et al.* Stimulation-evoked Ca²⁺ signals in astrocytic processes at hippocampal CA3-CA1 synapses of adult mice are modulated by glutamate and ATP. *J. Neurosci.* **35**, 3016–3021 (2015).
15. Panatier, A. *et al.* Astrocytes are endogenous regulators of basal transmission at central synapses. *Cell* **146**, 785–798 (2011).
16. Serrano, A., Haddjeri, N., Lacaille, J.-C. & Robitaille, R. GABAergic network activation of glial cells underlies hippocampal heterosynaptic depression. *J. Neurosci.* **26**, 5370–5382 (2006).
17. Kang, J., Jiang, L., Goldman, S. A. & Nedergaard, M. Astrocyte-mediated potentiation of inhibitory synaptic transmission. *Nat. Neurosci.* **1**, 683–692 (1998).
18. Mariotti, L., Losi, G., Sessolo, M., Marcon, I. & Carmignoto, G. The inhibitory neurotransmitter GABA evokes long-lasting Ca(2+) oscillations in cortical astrocytes. *Glia* **64**, 363–373 (2016).
19. Ding, F. *et al.* α 1-Adrenergic receptors mediate coordinated Ca²⁺ signaling of cortical astrocytes in awake, behaving mice. *Cell Calcium* **54**, 387–394 (2013).

20. Paukert, M. *et al.* Norepinephrine controls astroglial responsiveness to local circuit activity. *Neuron* **82**, 1263–1270 (2014).
21. Mu, Y. *et al.* Glia Accumulate Evidence that Actions Are Futile and Suppress Unsuccessful Behavior. *Cell* **178**, 27–43.e19 (2019).
22. Reitman, M. E. *et al.* Norepinephrine links astrocytic activity to regulation of cortical state. *Nat. Neurosci.* **26**, 579–593 (2023).
23. Pittolo, S. *et al.* Dopamine activates astrocytes in prefrontal cortex via α 1-adrenergic receptors. *Cell Rep.* **40**, 111426 (2022).
24. Vaidyanathan, T. V. The role of cortical astrocytes in sleep regulation. (University of California, San Francisco, 2021).
25. Wang, Y. *et al.* Accurate quantification of astrocyte and neurotransmitter fluorescence dynamics for single-cell and population-level physiology. *Nat. Neurosci.* **22**, 1936–1944 (2019).
26. Zheng, K. *et al.* Time-Resolved Imaging Reveals Heterogeneous Landscapes of Nanomolar Ca^{2+} in Neurons and Astroglia. *Neuron* **88**, 277–288 (2015).
27. Bindocci, E. *et al.* Three-dimensional Ca^{2+} imaging advances understanding of astrocyte biology. *Science* **356**, (2017).
28. Di Castro, M. A. *et al.* Local Ca^{2+} detection and modulation of synaptic release by astrocytes. *Nat. Neurosci.* **14**, 1276–1284 (2011).
29. Nimmerjahn, A., Mukamel, E. A. & Schnitzer, M. J. Motor behavior activates Bergmann glial networks. *Neuron* **62**, 400–412 (2009).
30. Srinivasan, R. *et al.* Ca^{2+} signaling in astrocytes from $\text{Ip}3\text{r}2(-/-)$ mice in brain slices and during startle responses in vivo. *Nat. Neurosci.* **18**, 708–717 (2015).

31. Sekiguchi, K. J. *et al.* Imaging large-scale cellular activity in spinal cord of freely behaving mice. *Nat. Commun.* **7**, 11450 (2016).
32. Rothstein, J. D. *et al.* Knockout of glutamate transporters reveals a major role for astroglial transport in excitotoxicity and clearance of glutamate. *Neuron* **16**, 675–686 (1996).
33. Oliet, S. H., Piet, R. & Poulain, D. A. Control of glutamate clearance and synaptic efficacy by glial coverage of neurons. *Science* **292**, 923–926 (2001).
34. Michaluk, P., Heller, J. P. & Rusakov, D. A. Rapid recycling of glutamate transporters on the astroglial surface. *eLife* **10**, (2021).
35. Higashi, K. *et al.* An inwardly rectifying K(+) channel, Kir4.1, expressed in astrocytes surrounds synapses and blood vessels in brain. *Am J Physiol, Cell Physiol* **281**, C922-31 (2001).
36. Clausen, T. Potassium and sodium transport and pH regulation. *Can. J. Physiol. Pharmacol.* **70 Suppl**, S219-22 (1992).
37. Wang, F. *et al.* Astrocytes modulate neural network activity by Ca²⁺-dependent uptake of extracellular K⁺. *Sci. Signal.* **5**, ra26 (2012).
38. Hibino, H. *et al.* Inwardly rectifying potassium channels: their structure, function, and physiological roles. *Physiol. Rev.* **90**, 291–366 (2010).
39. Li, L., Head, V. & Timpe, L. C. Identification of an inward rectifier potassium channel gene expressed in mouse cortical astrocytes. *Glia* **33**, 57–71 (2001).
40. de Ceglia, R. *et al.* Specialized astrocytes mediate glutamatergic gliotransmission in the CNS. *Nature* **622**, 120–129 (2023).

41. Perea, G. *et al.* Activity-dependent switch of GABAergic inhibition into glutamatergic excitation in astrocyte-neuron networks. *eLife* **5**, (2016).
42. Schell, M. J., Molliver, M. E. & Snyder, S. H. D-serine, an endogenous synaptic modulator: localization to astrocytes and glutamate-stimulated release. *Proc Natl Acad Sci USA* **92**, 3948–3952 (1995).
43. Shigetomi, E., Jackson-Weaver, O., Huckstepp, R. T., O’Dell, T. J. & Khakh, B. S. TRPA1 channels are regulators of astrocyte basal calcium levels and long-term potentiation via constitutive D-serine release. *J. Neurosci.* **33**, 10143–10153 (2013).
44. Poskanzer, K. E. & Yuste, R. Astrocytic regulation of cortical UP states. *Proc Natl Acad Sci USA* **108**, 18453–18458 (2011).
45. Poskanzer, K. E. & Yuste, R. Astrocytes regulate cortical state switching in vivo. *Proc Natl Acad Sci USA* **113**, E2675-84 (2016).
46. Vaidyanathan, T. V., Collard, M., Yokoyama, S., Reitman, M. E. & Poskanzer, K. E. Cortical astrocytes independently regulate sleep depth and duration via separate GPCR pathways. *eLife* **10**, (2021).
47. Bojarskaite, L. *et al.* Astrocytic Ca²⁺ signaling is reduced during sleep and is involved in the regulation of slow wave sleep. *Nat. Commun.* **11**, 3240 (2020).
48. Gordon, G. R. J. *et al.* Astrocyte-mediated distributed plasticity at hypothalamic glutamate synapses. *Neuron* **64**, 391–403 (2009).
49. Matsuzaki, M. *et al.* Dendritic spine geometry is critical for AMPA receptor expression in hippocampal CA1 pyramidal neurons. *Nat. Neurosci.* **4**, 1086–1092 (2001).
50. Higley, M. J. & Sabatini, B. L. Competitive regulation of synaptic Ca²⁺ influx by D2 dopamine and A2A adenosine receptors. *Nat. Neurosci.* **13**, 958–966 (2010).

51. Araya, R., Vogels, T. P. & Yuste, R. Activity-dependent dendritic spine neck changes are correlated with synaptic strength. *Proc Natl Acad Sci USA* **111**, E2895-904 (2014).
52. Kwon, T. *et al.* Ultrastructural, molecular and functional mapping of gabaergic synapses on dendritic spines and shafts of neocortical pyramidal neurons. *Cereb. Cortex* **29**, 2771–2781 (2019).
53. Bernardinelli, Y. *et al.* Activity-dependent structural plasticity of perisynaptic astrocytic domains promotes excitatory synapse stability. *Curr. Biol.* **24**, 1679–1688 (2014).
54. Filevich, O. & Etchenique, R. RuBiGABA-2: a hydrophilic caged GABA with long wavelength sensitivity. *Photochem. Photobiol. Sci.* **12**, 1565–1570 (2013).
55. Peterka, D. S. *et al.* Fast two-photon neuronal imaging and control using a spatial light modulator and ruthenium compounds. in *Photonic Therapeutics and Diagnostics VI* (eds. Kollias, N. *et al.*) vol. 7548 75484P (SPIE, 2010).
56. Fino, E. *et al.* RuBi-Glutamate: Two-Photon and Visible-Light Photoactivation of Neurons and Dendritic spines. *Front. Neural Circuits* **3**, 2 (2009).
57. Charles, A. Intercellular calcium waves in glia. *Glia* **24**, 39–49 (1998).
58. Cabrera, R. *et al.* A Visible-Light-Sensitive Caged Serotonin. *ACS Chem. Neurosci.* **8**, 1036–1042 (2017).
59. Araya, R., Andino-Pavlovsky, V., Yuste, R. & Etchenique, R. Two-photon optical interrogation of individual dendritic spines with caged dopamine. *ACS Chem. Neurosci.* **4**, 1163–1167 (2013).
60. Filevich, O., Salierno, M. & Etchenique, R. A caged nicotine with nanosecond range kinetics and visible light sensitivity. *J. Inorg. Biochem.* **104**, 1248–1251 (2010).

61. Bekar, L. K., He, W. & Nedergaard, M. Locus coeruleus alpha-adrenergic-mediated activation of cortical astrocytes in vivo. *Cereb. Cortex* **18**, 2789–2795 (2008).

Chapter 2:

Accurate quantification of astrocyte and neurotransmitter fluorescence dynamics for single-cell and population-level physiology

Abstract

Recent work examining astrocytic physiology centers on fluorescence imaging approaches, due to development of sensitive fluorescent indicators and observation of spatiotemporally complex calcium and glutamate activity. However, the field remains hindered in fully characterizing these dynamics, both within single cells and at the population-level, because of the insufficiency of current region-of-interest-based approaches to describe activity that is often spatially unfixed, size-varying, and propagative. Here, we present an analytical framework that releases astrocyte biologists from ROI-based tools. The Astrocyte Quantitative Analysis (AQuA) software takes an event-based perspective to model and accurately quantify the complex activity in astrocyte imaging datasets. We apply AQuA to a range of *ex vivo* and *in vivo* imaging data, and uncover novel physiological phenomena in each. Since AQuA is data-driven and based on machine learning principles, it can be applied across model organisms, fluorescent indicators, experimental modes, and imaging resolutions and speeds, enabling researchers to elucidate fundamental astrocyte physiology.

Introduction

With increased prevalence of multiphoton imaging and optical probes to study the physiology of astrocytes¹⁻³, many groups now have the tools to study fundamental functions that previously remained unclear. Recent work has focused on new ways to decipher how astrocytes respond to

neurotransmitter and neuromodulator circuit signals⁴⁻⁷ and how the spatiotemporal patterns of their activity shape local neuronal activity⁸⁻¹⁰. Recording astrocytic dynamics with the goal of decoding their disparate roles in neural circuitry has largely centered on cell type-specific expression of genetically encoded probes to carry out intracellular calcium (Ca^{2+}) imaging using variants of GCaMP³. In addition, many groups have studied astrocytic function by performing extracellular glutamate imaging using GluSnFR², and several more recently developed genetically encoded fluorescent probes for neurotransmitters such as GABA¹¹, norepinephrine (NE)¹², ATP¹³, and dopamine¹⁴ are poised to expand our understanding of astrocytic circuit biology.

Compared to neuronal Ca^{2+} imaging, astrocytic Ca^{2+} imaging using GCaMP presents particular challenges for analysis due to their complex spatiotemporal dynamics. Thus, astrocyte-specific analysis software has been developed to capture these dynamics, including techniques that divide the cell into distinct subcellular regions corresponding to their anatomy⁴ or apply a watershed algorithm to identify regions-of-interest (ROIs)¹⁵. Likewise, GluSnFR imaging analysis techniques are based on manually or semi-manually selected ROIs, or by analyzing the entire imaging field together as one ROI^{2,6,8,16}. It is worth noting that these and most, although not all^{17,18}, other current techniques rely on the conceptual framework of ROIs for image analysis. However, astrocytic Ca^{2+} and GluSnFR fluorescence dynamics are particularly ill-suited for ROI-based approaches, because the concept of the ROI has several inherent assumptions that cannot be satisfied for astrocytic activity data. Astrocytic Ca^{2+} signals, for example, can occupy regions that change size or location across time, can propagate within or across cells, and can spatially overlap with other Ca^{2+} signals that are temporally distinct. ROI-based approaches assume that for a given ROI, all signals have a fixed size and shape as

specified by the ROI, and all locations within the ROI undergo the same dynamics, without propagation. Accordingly, ROI-based techniques may over- or under-sample these data, thus obscuring true dynamics and hindering physiological discovery in these cells. An ideal imaging analysis framework for astrocytes would take into account, and quantify, all of these dynamic features and be free of these ROI-based analytical restrictions. In addition, an ideal tool should be applicable to astrocyte imaging data across spatial scales, encompassing subcellular, cellular, and population-wide fluorescence dynamics.

In this work, we set out to design an image analysis toolbox that would capture the complex, wide-ranging fluorescent signals observed in most dynamic astrocyte imaging datasets. We reasoned that a non-ROI-based approach would better describe the observed fluorescent dynamics, and applied probability theory, machine learning, and computational optimization techniques to generate an algorithm to do so. We name this resulting software package Astrocyte Quantitative Analysis (AQuA) and validate its utility by applying it to simulated datasets that reflect the specific features that make analyzing astrocyte data challenging. We next apply AQuA to three experimental two-photon (2P) imaging datasets—*ex vivo* Ca^{2+} imaging of GCaMP6 from acute cortical slices, *in vivo* Ca^{2+} imaging of GCaMP6 in primary visual cortex (V1) of awake, head-fixed mice, and *ex vivo* extracellular glutamate, GABA, and NE imaging. In these test cases, we find that AQuA accurately detects fluorescence dynamics by capturing fluorescence events as they change in space and time, rather than the activity from a single location in space, as in ROI-based approaches. AQuA outputs a comprehensive set of biologically relevant parameters from these datasets, including propagation speed, propagation direction, area, shape, and spatial frequency. Using these detected events and associated output

features, we uncover neurobiological phenomena that have not been previously described in astrocytes.

A wide variety of cellular and circuit functions have been ascribed to astrocytes, and a key question currently under examination in the field is whether certain types of Ca^{2+} activities observed in these cells correspond to particular neurobiological functions. However, current techniques with which to classify these observed dynamics remain inadequate since they do not capture many of the dynamics recorded in fluorescent imaging of astrocytic activity. The framework we describe here allows for a rigorous, in-depth dissection of astrocyte physiology across spatial and temporal imaging scales, and sets the stage for a comprehensive categorization of heterogeneous astrocyte activities both at baseline and after experimental manipulations.

Results

Design principles of the AQuA algorithm

To move away from ROI-based analysis approaches and accurately capture heterogeneous astrocyte fluorescence dynamics, we set out to design an algorithm to decompose raw dynamic astrocyte imaging data into a set of quantifiable events (Fig. 2.1a, Extended Data Fig. 2.1–2.3). Here, we define an event as a cycle of a signal increase and decrease that coherently occurs in a spatially connected region, but this region is defined by the fluorescence dynamics, not *a priori* by the user or the cell morphology. Algorithmically, this definition is converted to the following two rules: 1) the temporal trajectory for an event contains only one peak (single-cycle rule, Fig. 2.1b) and 2) adjacent locations in the same event have similar trajectories (smoothness rule, Fig. 2.1b). The task of the AQuA algorithm is to detect all events, and, for each event, to identify the temporal trajectory, the spatial footprint, and how the signal propagates within the footprint.

Briefly, our strategy of event-detection is to a) explore the single-cycle rule to find peaks, which are used to specify the time window and temporal trajectory, b) explore the smoothness rule to group spatially adjacent peaks, whose locations specify the footprint, c) apply machine learning and optimization techniques to iteratively refine the spatial and temporal properties of the event to best fit the data, and d) apply statistical theory to determine whether a detected event is true or due to noise (Fig. 2.1).

Full statistical and computational details are provided in the Methods, but we want to highlight one technical innovation (Graphical Time Warping [GTW])¹⁹ and one new concept (the single-source rule) that jointly enable a nuanced analysis of astrocyte fluorescence dynamics as shown below in application to experimental datasets. With GTW, we are able to consider fluorescent signal propagation as integrated into each modeled event. To the best of our knowledge, signal propagation has never been rigorously accounted for and has been considered an obstacle to analysis. With GTW, we can estimate and quantify propagation patterns in the data. With the introduction of the single-source rule (Fig. 2.1b), each event only contains a single initiation source and we can separate events that are initiated at different locations but meet in the middle. The single-source rule also allows us to divide large-scale activity that can occur across an entire field-of-view into individual events, each with a single initiation location.

The output of the event-based AQUA algorithm is a list of detected events, each associated with three categories of parameters: 1) the spatial map indicating where the event occurs, 2) the dynamic curve corresponding to fluorescence change over time (dF/F), and 3) the propagation map indicating signal propagation. For each event, we use the spatial map to compute the event area, diameter and shape of the domain it occupies (Fig. 2.1c). Using the dynamic curve, we can calculate maximum dF/F , duration, onset-time, rise-time and decay-time.

Using the propagation map, we extract event initiation location, as well as propagation path, direction, and speed. In addition, AQuA computes features involving more than one event, such as the frequency of events at a position, and the overall number of events in a specified region or cell. A complete list of features is available in Wang & DelRosso et al., 2019 and online at <https://github.com/yu-lab-vt/AQuA>.

Validation of AQuA using simulated data

To validate AQuA, we designed three simulation datasets so that we know the ground truth for the dynamics of each event. These three datasets independently vary the three key phenomena observed in astrocyte imaging datasets that cause ROI-based approaches to misanalyze the data: size-variability, location-variability, and propagation. While these three phenomena usually co-occur in real datasets, we simulated each phenomenon independently to examine their individual impact and test AQuA's performance relative to other fluorescence image analysis tools, including CaImAn²⁰, Suite2P²¹, CaSCaDe¹⁵, and GECI-quant⁴. CaImAn and Suite2P are widely used for neuronal Ca²⁺ imaging analysis while CaSCaDe and GECI-quant were designed specifically for Ca²⁺ activity in astrocytes. We should note that although CaSCaDe uses the term "events" to describe Ca²⁺ transients, all four methods are ROI-based. In our analysis of these simulated datasets, as elaborated in the Methods, we optimally tuned the ROI-detection for all methods for an objective comparison of the best performance of each method (Extended Data Table 2.1). We also systematically changed the signal-to-noise-ratio (SNR) to examine the effect of noise on each analysis method.

To evaluate the performance on all simulated datasets, we used two measures: IoU and a map of the event counts. IoU (intersection over union) measures the consistency between

detected and the ground-truth events, and takes into account both the spatial and temporal accuracy of detected events. IoU ranges from 0 to 1, where 1 indicates perfect detection and 0 indicates a complete failure in detection. The map of the event counts is obtained by counting the number of events at each pixel in the field, and is used to visually assess the accuracy of event-detection results by a comparison to the ground-truth map.

We first studied the impact of size-varying events (Fig. 2.2a), in which multiple events occurred at the same location and the event centers remain fixed, but sizes changed across different events. The degree of size change is quantified using size-change odds (see Methods) where a size-change odds of 1 indicates events with the same size, while an odds of 5 is the largest size change we simulated. For instance, when we set the odds at 5, we simulate events with sizes randomly distributed between 0.2 and 5 times the baseline size, with an SNR of 10dB, chosen to closely match the noise level in real experimental data. When there was no size change (odds=1), all methods, as expected, performed well with IoUs near 0.95 (Fig. 2.2a). When the degree of size change was increased, AQuA still performed well (IoU=0.95), while all other methods quickly drop to 0.4–0.5. We then changed our analysis to study the impact of different SNRs on performance by varying SNR, but fixing the size-change odds. AQuA performed better with increasing SNR and achieved nearly perfect detection accuracy (IoU=1) at 20dB. In comparison, all other methods had an IoU less than 0.6, even at high SNR (Fig. 2.2a). We also examined the results by visualizing event counts at each pixel (Extended Data Fig. 2.4–2.5). With size change odds of 3 or 5, the map of ground truth event-counts did not show clear ROI boundaries, because events from the same ROI had various sizes, and because events from different ROIs can overlap at some spatial locations (Extended Data Fig. 2.4). It is clear from

these maps that AQuA reported faithfully the events under various SNRs but all other methods had erroneous event counts and produced artificial patterns.

We next focused on the impact of shifting the event locations. In these simulated datasets, event size was fixed but event location changed, and degree of change was represented by a location change score (Fig. 2.2b). A value of zero indicates no location change and greater values represent larger degrees of change. Here, results are similar to changing size, as above. AQuA models the location change well and its performance is not affected by degree of location change. Likewise, AQuA reached near perfect results when SNR was high. In contrast, all other analysis methods performed poorly with changing locations. In particular, the other astrocyte-specific methods (CaSCaDe and GECl-quant) missed many signals. Even though the overall conclusion is similar for both the size- and location-changing events, the peer methods had more variation of IoU performance among themselves and the event count map showed distinct patterns (Extended Data Fig. 2.4).

In our third simulated dataset, we asked how the phenomenon of fluorescence signal propagation impacts the performance of AQuA compared to the other methods. Two propagation types—growing and moving—were simulated in this dataset (Fig. 2.2c), although they were also separately evaluated (Extended Data Fig. 2.6). Propagation frame number denotes the difference between the earliest and latest onset times within a single event. When propagation frame number is zero, all signals within one ROI, but not necessarily across ROIs, are synchronized and there is no propagation. Similar results to the two scenarios discussed above were obtained here, with AQuA out-performing all the other methods by a large margin. These results indicate that AQuA can handle various types of propagation well, while the performance of other methods degrades rapidly when propagation is introduced.

In summary, when any of the three ROI-violating factors—size-variability, location-variability, and propagation—is introduced, other methods do not accurately capture the signal dynamics of the simulated data, and AQuA outperforms them by a large margin. We expect that the performance margin on real experimental data is larger than those quantified in the simulation studies here, since real data exhibits multiple ROI-violating factors and the performance of the ROI-based methods is over-estimated in our simulations (see Methods). However, these IoU analyses and the event count visualizations informed us about different types of errors observed in ROI-based methods. To focus on astrocyte-specific methods, CaSCaDe tends to over-segment, as it is based on watershed segmentation. GECI-quant, especially its soma-segmentation step, is particularly challenged by noise, causing many signals to be lost (Extended Data Fig. 2.5). This accounts for the result that GECI-quant is not able to detect anything when the SNR is low (Fig. 2.2b, right). We note that although all events are constrained in the same ROI in the propagation simulations, propagation caused ROI-based approaches to quickly decline in performance. Here, GECI-quant was influenced by noise level, while CaSCaDe’s assumption of synchronized signals did not allow accurate capture of the event dynamics.

AQuA enables identification of single-cell physiological heterogeneities

To test AQuA’s performance on real astrocyte fluorescence imaging data and ask whether AQuA could be used for classifying Ca^{2+} activities observed in single cells, we first ran AQuA’s event-detection on Ca^{2+} activity recorded from astrocytes in acute cortical slices from mouse V1 using 2P microscopy. We used a viral approach to express the genetically encoded Ca^{2+} indicator GCaMP6f³ in layer 2/3 (L2/3) astrocytes. Unlike ROI-based approaches, AQuA detects both

propagative and non-propagative activity, revealing Ca^{2+} events with a variety of shapes and sizes (Fig. 2.3a, left). Further, since AQUA not only detects Ca^{2+} events' spatial footprint but also their time-course, we can apply AQUA to measure the propagation direction each event travels over its lifetime. Imaging single cells, we used the soma as a landmark, and classified events as traveling toward the soma (pink), away from the soma (purple), or static (blue) for the majority of its lifetime (Fig. 2.3a, right). We used AQUA's automatic feature-extraction and combined multiple measurements (size, propagation direction, duration, and minimum proximity to soma) into one spatiotemporal summary plot (Fig. 2.3b). Since astrocytes exhibit a wide diversity of Ca^{2+} activities across subcellular compartments^{6,22,23}, plotting the signals this way rather than standard dF/F transients highlights these heterogeneities, allows us to map the spatial location of the Ca^{2+} signals, and enables a quick, visual impression of a large amount of complex data (Extended Data Fig. 2.7). We note that while the expression of GCaMP6 in these experiments enabled us to analyze events within single cells, some probes do not allow clear delineation of single cells. However, a secondary fluorophore (such as TdTomato) often serves the purpose of defining the morphology of single cells, and the AQUA software has been designed to overlay morphological masks on the dynamic fluorescence channel.

We next asked whether some subcellular regions of astrocytes have more dynamic activity than others across all analyzed cells ($n=11$ cells). Although we detected more static events than dynamic overall (Extended Data Fig. 2.8a), we observed a higher proportion of dynamic events than static events in the soma (59%, Fig. 2.3c, Extended Data Fig. 2.8b). We then characterized events by propagation direction and event initiation location (Fig. 2.3d). Events that begin close to the soma (≤ 50 th percentile) and propagate away (purple) were on average larger than the events propagating toward the soma (pink, two-tailed t-test). Similarly,

those events that began close to the soma (≤ 50 th percentile) and propagated away had on average a longer duration than events propagating toward the soma (two-tailed t-test, Fig. 2.3e, Extended Data Fig. 2.8).

One of AQuA's strengths is its ability to automatically extract a large number of features. These features can be used to form a comprehensive Ca^{2+} measurement matrix, where each row represents an event and each column an extracted feature, and which includes all events for each cell (Extended Data Fig. 2.9). Dimensionality reduction applied to this matrix can, in turn, be used to visualize each cell's Ca^{2+} signature (Extended Data Fig. 2.9, white rows separate each individual cell). To do this, we applied t-distributed Stochastic Neighbor Embedding (t-SNE)²⁴, followed by k-means clustering to assign the cells to groups (Extended Data Fig. 2.9), revealing clusters marked by cells with large differences in median frequency (Fig. 2.3f). Astrocytic Ca^{2+} frequency is commonly measured as the number of transients that occur over time within an ROI. Here, we instead define frequency from an event-based perspective in two ways: 1) for each event, the number of other events that overlap in time, and 2) for each event, the number of other events that overlap in space. We used these two measures (temporal and spatial overlap) and several other extracted measures (Extended Data Fig. 2.9) to construct the matrix used for t-SNE visualization and clustering. We next tested how well our AQuA-specific features perform at clustering the heterogeneity among cells compared to two ROI-based methods (Fig. 2.3g), and found that the AQuA-based method outperformed the others. In fact, even when we only use AQuA-specific features for this analysis—area, temporal overlap, spatial overlap, and propagation speed—and remove all features that can be extracted from ROI-based methods, AQuA still significantly outperforms in clustering cells (Extended Data Fig. 2.9g–i). AQuA-extracted features that correspond only to those that can be obtained by ROI-based methods—

standard frequency, amplitude, duration—do not allow clustering significantly better than the ROI-based approaches themselves (Extended Data Fig. 2.9g–i), suggesting that the AQuA-specific features are those that best capture dynamic fluorescence features that vary among single cells. This indicates that AQuA may be used to extract data from existing *ex vivo* Ca²⁺ imaging datasets to reveal previously uncovered dynamics and sort cells into functionally relevant clusters.

In vivo astrocytic Ca²⁺ bursts display anatomical directionality

Recent interest in astrocytic activity at the mesoscale has been driven by population-level, multicellular astrocytic Ca²⁺ imaging^{1,5,7,8,25-27}. To test the power of AQuA-based event detection, we next applied it to populations of *in vivo* astrocyte Ca²⁺ activity. Previous studies have described temporal details of astrocyte activation^{4,5,7,8,25}, yet have left largely unaddressed the combined spatiotemporal properties of Ca²⁺ activity at the circuit-level, across multiple cells. Here, we explored whether AQuA can uncover spatial patterns within populations of cortical astrocytes in an awake animal, and carried out head-fixed, 2P imaging of GCaMP6f activity in V1, L2/3 astrocytes. Populations of *in vivo* cortical astrocytes exhibit both small, focal, desynchronized Ca²⁺ activity²⁵, and large, coordinated activities^{4,5} that we refer to as bursts in this context. Importantly, AQuA detected both of these classes of Ca²⁺ activity in the same *in vivo* imaging datasets, suggesting that it could be a powerful tool to investigate both kinds of activity—and the interactions between them—even within a single dataset (Fig. 2.4a). Similar to previous studies, we observed many (but not all) of the bursts co-occurring with locomotion periods (Fig. 2.4b, pink), and many events within these burst periods displayed propagation (Fig. 2.4c, top). These propagative events were larger in area and had greater propagation distances compared to the

events that occurred during the inter-burst periods (Fig. 2.4c, bottom). Here, to test whether AQuA could help us understand these large bursts and discover discrete features of this phenomenon, we next focused our investigation on all the events occurring during the burst periods (Extended Data Fig. 2.10).

To analyze the structure of these burst-period Ca^{2+} events, we investigated fluorescence propagation across multiple spatial scales: at the level of individual events, of subregions of the imaging field encompassing multiple events, and of the entire imaging field. At the level of individual events within a single burst, plotting the individual event direction within the entire field of view did not reveal a consistent propagation direction (Fig. 2.4d). However, when we divided our field-of-view into equivalently sized, subregional tiles (Fig. 2.4e), we observed more consistent propagation direction within single subregions (Fig. 2.4f). When we plot the cumulative count of the percentage of bursts with regions that propagate in the same direction, we indeed observe that this curve is right-shifted compared to a simulated random assignment of majority regional propagation direction (Fig. 2.4g), suggesting that there does exist regularity in the propagation pattern within bursts, but that this only becomes apparent at a spatial scale larger than individual events.

Since the consistency of propagation directionality increased with increasing spatial scales, we next explored whole imaging field dynamics during Ca^{2+} burst events. We noted that the percentage of the active field of view varied across burst periods (Fig. 2.4b), with a wide variability from few to hundreds of events (Fig. 2.4h). To control for number and size of events, we used the difference between each event's onset time to calculate a single burst-wide propagation direction (Fig. 2.4h, black arrow). Doing so revealed a consistent posterior-medial directionality of population Ca^{2+} activity in L2/3 V1 astrocytes (Fig. 2.4i). Although Ca^{2+} bursts

have been previously observed using GCaMP6 imaging in awake mice^{4,5}, consistent spatial directionality with respect to the underlying anatomy has never been described. This observed posterior-medial directionality may be revealing anatomical and physiological underpinnings of these bursts, and since they have been shown to be at least partly mediated by norepinephrine^{5,7}, they could be reflective of the response of groups of cortical astrocytes to incoming adrenergic axons originating in locus coeruleus. Regardless of burst mechanism(s), these results suggest that *in vivo*, astrocytic Ca²⁺ propagation dynamics differ depending on the spatial scale examined, which may explain previously described discrepancies in dynamics.

AQuA-based detection of extracellular molecular dynamics

We next asked whether AQuA could be used to detect astrocytic fluorescent activities with distinct spatiotemporal dynamics than we observe when measuring intracellular Ca²⁺. We decided to perform imaging of extracellular-facing probes, including GluSnFR², to measure extracellular glutamate dynamics, since it has been widely used for glutamate imaging^{2,6,8} and astrocytes regulate extracellular glutamate concentration. In addition, GluSnFR dynamics are much faster than GCaMP dynamics, which causes detection to be very susceptible to low SNR. This can be an additional challenge and thus much previous GluSnFR analyses has relied on averaging across multiple trials. While GluSnFR has been expressed both in astrocytes and in neurons previously^{2,8,16,28}, how cell type-specific expression and morphology—particularly relative to synaptic and extra-synaptic glutamate release—determines its fluorescent dynamics has not been fully explored^{16,28}. No previously applied analytical tools have been reported to automatically detect GluSnFR-based glutamate events to accommodate differential event sizes and shapes. Here, we explored whether application of AQuA could be used to detect cell type-

specific differences in glutamate dynamics that may be based on heterogeneous underlying morphologies and cell biological mechanisms.

We expressed GluSnFR in either astrocytes or neurons using cell type-specific viruses² and carried out 2P imaging of spontaneous GluSnFR activity in acute cortical V1 slices from L2/3. Distinct morphological differences between astrocytic and neuronal expression of GluSnFR were evident, as has been observed previously^{8,29,30} (Fig. 2.5a). We applied AQUA to these datasets to detect significant increases in GluSnFR fluorescence, and were able to detect events that were too small and dim to detect by eye; AQUA-detected events were confirmed by *post hoc* ROI-based analysis. Indeed, 62% of astrocytic events had an area less than the size of a single astrocyte ($100 \mu\text{m}^2$), and 8% of astrocytic and 35% of neuronal glutamate events had a small maximum dF/F (less than 0.5). Because GluSnFR events have previously been detected by spatially averaging within a single cell or across broader areas of tissue, *or* by manual detection, the events that AQUA detects are most likely missed by ROI-based methods^{6,8,16} (Extended Data Fig. 2.11). Because AQUA is designed to detect events independently from shape or size, events of heterogeneous size and shape were revealed during this analysis (Fig. 2.5a–b). A large proportion of these spontaneous GluSnFR events changed size over the course of the event, with 42% of total astrocytic and 32% of total neuronal glutamate events exhibiting changes in area. On average, astrocytic GluSnFR events were significantly larger ($274 \pm 39.56 \mu\text{m}^2$) than neuronal events ($172 \pm 57.06 \mu\text{m}^2$), sometimes encompassing an entire astrocyte (Extended Data Fig. 2.11). Neuronal GluSnFR events were significantly more circular (Fig. 2.5b–d), perhaps reflecting morphological differences between cell type somata. We also found that between cell types, GluSnFR events exhibited different size dynamics (Fig. 2.5b–c). While there was no difference in the rate of increase in event size between astrocytes and neurons, we did observe

that the rate of size decrease of astrocytic events between frames was larger than that of neuronal events (Fig. 2.5c), which may reflect differential synaptic and extrasynaptic glutamate dynamics in proximity to subcellular compartments of each cell type.

Once we found that AQuA-based detection was effective for quantification of spontaneous GluSnFR events, we wanted to test its performance on more spatially and temporally precise glutamate events, since GluSnFR can be used to measure synaptic release of glutamate when imaged at fast frame rates^{2,31}. To do this, we performed fast (~100Hz) GluSnFR imaging while photoactivating a caged glutamate compound (RuBi-glutamate^{10,32}) with a second laser beam. In these experiments, we tested uncaging pulses at various durations (25–150ms), and applied AQuA to detect these small-scale, fast events (Fig. 2.5d, right). Although we did observe an increase in detection accuracy (identification of event at the time and location of the laser uncaging pulse) of uncaging-defined GluSnFR events at longer uncaging durations, AQuA detection still showed high accuracy levels at shorter durations, with a minimum of 96% average accuracy across durations (Fig. 2.5d, right; n = 5 cells, 3 replicates/cell). These results indicate that AQuA works well for fluorescent event detection at fast frame rates.

We lastly wanted to demonstrate that AQuA can be used for other extracellular-facing probes that are relevant for astrocyte-neuron physiology. To do this, we imaged and analyzed two recently developed genetically encoded probes that sense extracellular neurotransmitters: GABASnFR¹¹ and GRAB-NE¹², which report GABA and NE dynamics, respectively. We expressed GABASnFR (Fig. 2.5e, left) in cortical astrocytes and GRAB-NE in cortical neurons (Fig. 2.5f, left), and performed *ex vivo* 2P imaging before and after bath application of either NE or GABA. In both cases, we used AQuA to detect events as the neurotransmitter contacted the fluorescent sensors. For GABASnFR expression in individual astrocytes, we observed that each

event increased in both fluorescence amplitude and area with cell-specific dynamics (Fig. 2.5e, right). While the widespread neuronal expression of GRAB-NE did not allow for cell-specific analysis, it did allow us to observe waves of NE as it was bathed over the slice. Here, AQuA enabled detection of the dynamic spatial location, amplitude, and area of these waves as they progressed across the slice (Fig. 2.5f, right), indicating that AQuA may be useful to quantify propagating wavefronts in other contexts. Together, results in this section suggest that AQuA-based detection can be used to quantify the dynamics of extracellular molecules at a range of speeds and spatial spreads, across multiple cell types and expression patterns.

Discussion

With the development and application of a flexible event-based analysis tool for astrocyte imaging datasets, we hope to enable many research groups to accurately quantify observed fluorescence dynamics, including those that are un-fixed, propagative, and size varying. Here, we demonstrate that AQuA performs better than many other image analysis methods—including those designed for astrocytic and neuronal applications—on simulated datasets, and describe fluorescent event detection in several types of datasets, using the genetically encoded GCaMP, GluSnFR, GABASnFR, and GRAB-NE indicators. Because AQuA is data-driven, it can be applied to datasets that have not been directly tested here, including those captured under different imaging magnifications and spatial resolutions, as well as confocal or wide-field imaging systems. In addition, since the AQuA algorithm functions independently from frame rate, datasets captured with faster or slower frame rates^{17,25} are also just as amenable to an event-based analysis with AQuA as those shown here. Further, AQuA is applicable to fluorescent indicators other than the ones tested here, particularly those that exhibit complex dynamics.

We envision the AQuA software and its underlying algorithm as enabling problem-solving for a wide range of astrocyte physiological questions, both because AQuA accurately captures dynamics exhibited by commonly used fluorescent indicators and because there are more features extracted by AQuA that can be analyzed than those extracted by existing methods. Since AQuA-specific features were able to capture heterogeneities we observed among single cells when imaging Ca^{2+} , we posit that these features may be more physiologically relevant than the standard measurements (amplitude, frequency, duration) used to describe astrocytic physiological differences, although these standard measures are also features extracted by AQuA. In the current work, we use these multiple features to describe the spontaneous astrocyte activity in cortex, but with varying spatial scale, fluorescent probe, and experimental preparation. In future work, we and others can apply AQuA-based analyses to other brain regions and layers to describe potential functional heterogeneities among astrocytes³³. Beyond baseline differences, we expect that AQuA will be a powerful tool to quantify physiological effects of pharmacological, genetic, and optogenetic manipulations, among others. These manipulations and subsequent analyses would allow researchers to examine both astrocyte-intrinsic and -extrinsic physiology, depending on whether astrocytes, neurons, or another brain cell type is being changed.

Significant disagreement in the field remains about basic physiological functions of astrocytes. Perhaps the most outstanding issue is whether astrocytes undergo vesicular release of transmitters such as glutamate. While we don't address this controversial topic in the current work, we expect that the heterogeneous activities that we uncover using an AQuA-based analysis of GluSnFR may be key in determining different sources of glutamate in neural circuits under different conditions, and could help untangle some of the conflicting data in this arena. Our tool

enabled us to identify extracellular glutamate changes not only by cell type, but also by event size and shape dynamics, demonstrating an in-depth analysis of GluSnFR data. The event-based analytical tools presented here may be particularly useful as next-generation GluSnFR variants become available and make multiplexed imaging experiments increasingly accessible³¹.

When surveying astrocyte Ca^{2+} imaging data, experimental regimes can largely be grouped into two categories: single-cell, usually *ex vivo* imaging and population-wide, *in vivo* imaging focusing on large-scale activity of many cells. Experimental data and neurobiological conclusions from these two groups can differ quite widely, or even conflict. This may be due, in part, to the large, population-wide bursts observed with the onset of locomotion *in vivo*. Many techniques used to analyze these bursting events—all ROI-based—can under-sample events that occur between bursts by swamping out smaller or shorter signals. Here, we present a technique that can be used to sample small- and large-scale activity in the same dataset or across datasets, in order to bridge spatiotemporal scales these datasets. As such, this event-based analysis tool has the potential to aid researchers in resolving outstanding physiological problems, while also tackling new ones.

As demonstrated by its utility with Ca^{2+} , glutamate, GABA, and NE datasets, AQuA also has the potential to be applied to many other fluorescence imaging datasets that exhibit non-static or propagative activity. Although we designed AQuA specifically to study dynamic astrocyte fluorescence, it is open-source and user-tunable, and we anticipate that experimentalists will find it advantageous in other contexts in which neuronal or non-neuronal cells exhibit non-static or propagative fluorescence activity. For example, recently described Ca^{2+} activity in oligodendrocytes displays some similar properties to that in astrocytes^{34,35} and AQuA-based analysis may be useful. Likewise, subcellular compartments in neurons, such as dendrites or

dendritic spines, have also been shown to exhibit propagative, wave-like Ca^{2+} signals³⁶ and large-scale, whole-brain neuronal imaging can capture burst-like, population-wide events³⁷.

While we predict that the potential applications are wide, it is also important to note the limitations of AQuA, and be clear about when it will not be the most effective approach. Since AQuA detects local fluorescence changes as events, it is not well suited to strictly morphological dynamics, such as those observed in microglia, and it does not improve on the many excellent tools built for analyzing somatic neuronal Ca^{2+} activity^{20,21}, where ROI assumptions are well satisfied. In addition, AQuA was optimized for and tested on 2D datasets, as these comprise the majority of current imaging experiments in the field. As techniques for volumetric imaging rapidly advance, an extension to accommodate 3D imaging experiments will be necessary. We expect that AQuA is expandable to 3D datasets, based on the fact that the algorithmic design is not restricted to 2D assumptions. Although developing a full version of a 3D extension is beyond the scope of this paper, we have built a 3D prototype to test the feasibility of extending events from 2D to 3D (Extended Data Fig. 2.12). Using a simulated 3D dataset based on published¹⁷ astrocytes, the prototype performed well on 3D data, including detection of various event sizes and signal propagation rates (Extended Data Fig. 2.12). These results suggest that a full 3D AQuA extension—including the optimization of computational efficiency and visualization—will work on real 3D datasets in the future. In addition, the results demonstrate that AQuA is a flexible and robust platform that can accommodate new types of data without large changes to the underlying algorithm.

Methods

Viral injections and surgical procedures

For slice experiments, neonatal mice (Swiss Webster, P0–P4) were anesthetized by crushed ice anesthesia for 3 minutes and injected with 90nL total virus of *AAV5-GFaABC1D.Lck-GCaMP6f*, *AAV5-GFaABC1D.cyto-GCaMP6f*, *AAV1-GFAP-iGluSnFR*, *AAV1-hsyn-iGluSnFR*, *AAV2-GFAP-iGABASnFR.F102G*, and *AAV9-hsyn-NE2.1* at a rate of 2–3nL/sec. Six injections 0.5µm apart in a 2x3 grid pattern with 15nL/injection into assumed V1 were performed 0.2µm below pial surface using a UMP-3 microsyringe pump (World Precision Instruments). Mice were used for slice imaging experiments at P10–P23.

For *in vivo* experiments, adult mice (C57Bl/6, P50–P100) were given dexamethasone (5mg/kg) subcutaneously prior to surgery and then anesthetized under isoflurane. A titanium headplate was attached to the skull using C&B Metabond (Parkell) and a 3mm diameter craniotomy was cut over the right hemisphere ensuring access to visual cortex. Two 300nL injections (600nL total virus) of *AAV5-GFaABC1D.cyto-GCaMP6f* were made into visual cortex (0.5–1.0mm anterior and 1.75–2.5mm lateral of bregma) at a depth of 0.2–0.3mm and 0.5mm from the pial surface, respectively. Virus was injected at a rate of 2nL/s, with a 10min wait following each injection to allow for diffusion. Following viral injection, a glass cranial window was implanted to allow for chronic imaging and secured using C&B metabond³⁸. Mice were given at least ten days to recover, followed by habituation for three days to head fixation on a circular treadmill, prior to imaging.

Two-photon imaging

All 2P imaging experiments were carried out on a microscope (Bruker Ultima IV) equipped with a Ti:Sa laser (MaiTai, SpectraPhysics). The laser beam was intensity-modulated using a Pockels cell (Conoptics) and scanned with linear or resonant galvonometers. Images were acquired with a 16x, 0.8 N.A. (Nikon, *in vivo* GCaMP and *ex vivo* GRAB-NE) or 40x, 0.8. N.A. objective (Nikon, *ex vivo* GCaMP, GluSnFR, and GABASnFR) via a photomultiplier tube (Hamamatsu) using PrairieView (Bruker) software. For imaging, 950nm (GCaMP), 910nm (GluSnFR and GABASnFR), or 920nm (GRAB-NE) excitation and a 515/30 emission filter was used.

Ex vivo imaging

Coronal, acute neocortical slices (400 μ m thick) from P10–P23 mice were cut with a vibratome (VT 1200, Leica) in ice-cold cutting solution (in mM): 27 NaHCO₃, 1.5 NaH₂PO₄, 222 sucrose, 2.6 KCl, 2 MgSO₄, 2 CaCl₂. Slices were incubated in standard continuously aerated (95% O₂/5% CO₂) artificial cerebrospinal fluid (ACSF) containing (in mM): 123 NaCl, 26 NaHCO₃, 1 NaH₂PO₄, 10 dextrose, 3 KCl, 2 CaCl₂, 2 MgSO₄, heated to 37°C and removed from water bath immediately before introducing slices. Slices were held in ACSF at room temperature until imaging. Experiments were performed in continuously aerated, standard ACSF. 2P scanning for all probes was carried out at 512x512 pixel resolution. Acquisition frame rates were 1.1Hz (GCaMP), 4–100Hz (GluSnFR), 6Hz (GABASnFR), and 1.4Hz (GRAB-NE). For GluSnFR imaging and RuBi-glutamate uncaging experiments, GluSnFR imaging was performed at 950nm excitation to ensure that no RuBi-glutamate was released during scanning. Acquisition rates were between 95–100Hz, using resonant galvonometers. 300 μ M RuBi-glutamate was added to the circulating ACSF and using a second MaiTai laser tuned to 800nm, five uncaging points were

successively uncaged at each cell at durations indicated in the figure and at power <3mW that were shown in control experiments to cause no direct cell activation.

In vivo GCaMP imaging

At least two weeks following surgery mice were head-fixed to a circular treadmill and astrocyte calcium activity was visualized at ~2Hz effective frame rate from layers 2/3 of visual cortex with a 512x512 pixel resolution at 0.8 microns/pixel. Locomotion speed was monitored using an optoswitch (Newark Element 14) connected to an Arduino.

AQuA algorithm and event detection

Overview of the AQuA algorithm

Astrocytic events are heterogeneous and varying with respect to many aspects of their properties. In AQuA, we extensively applied machine learning techniques to flexibly model these events, so that our approach is data-driven and physiologically relevant parameters are extracted from the data instead of imposing *a priori* assumptions. Probability theory and numerical optimization techniques were applied to optimally extract fluorescent signals from background fluctuations. Here, we delineate the eight major steps in AQuA (Extended Data Fig. 2.1), discuss motivations behind the algorithm design, and describe key technical considerations in further detail.

Step 1: data normalization and preprocessing. This step removes experimental artifacts such as motion effects, and processes the data so that noise can be well approximated by a standard Gaussian distribution. Particular attention is paid to the variance stabilization, estimate of baseline fluorescence, and variance. Step 2: detect active voxels. Step 3: identify seeds for peak detection. Step 4: detect peaks and their spatiotemporal extension. These three steps work

together to achieve peak detection. To detect peaks we start from a seed, which is modeled as a spatiotemporal local maximum. However, since random fluctuations due to background noise can also result in local maxima, we need to detect active voxels such that only the local maxima on the active voxels are considered as seeds. Here, active voxels are those likely to have signals.

Step 5: cluster peaks to identify candidates for super-events. Temporarily ignoring the single-source requirement, the set of spatially-adjacent and temporally-close peaks is defined as a super-event. However, clustering results of spatially adjacent peaks are not super-events themselves, because a peak group may consist of noise voxels and temporally distant events.

Step 6: estimate the signal propagation patterns. Step 7: Detect super-events. To get super-events from peak clusters, we compute the temporal closeness between spatially adjacent peaks by estimating signal propagation patterns. The propagation pattern for each event is also important for its own sake, by providing a new way to quantify activity patterns. Step 8: split super-event into individual events with different sources. A super-event is split into individual events by further exploiting propagation patterns. Based on propagation patterns within a super-event, the locations of event initiation are identified as local minima of the onset time map. Each initiation location serves as the event seed. Individual events are obtained by assigning each pixel to an event based on spatial connectivity and temporal similarity.

A full description of each step and pseudocode are available in the Methods section of Wang & DelRosso et al., 2019.

Generation of simulation data sets

Spatial footprint templates: We built a set of templates for event footprints from real *ex vivo* data which serve as the basis for the ROI maps in the subsequent step. Footprints are processed by

morphology closing, hole filling, and morphology opening to clean boundaries, with 1683 templates generated total.

ROI maps: 2D ROI maps generated from spatial footprint are used to generate events in subsequent steps. Different simulation types have a different preference for the size of the ROIs. Maximum number of ROIs is set at 100; ROIs are randomly chosen and placed onto a 2D map <5 pixels from existing ROIs.

Simulation dataset 1 (size-varying events): To simulate event size changes, we generate events for each ROI and then alter them to have different sizes so that each ROI in the 2D map will be related to multiple events whose centers are inside that ROI, but whose sizes are different. The degree of size change is characterized by the odds ratio (maximum = 5) between the maximum and the minimum allowable sizes of the events associated with that ROI. For example, with an odds ratio of 2, the size of the event will range from 50–200% of the ROI area. The chances for the event size to be larger or smaller than the area of the ROI are the same. To achieve this, we generate a random number between 1 and 2, then randomly assign whether to enlarge size by multiplying or shrink by dividing by this factor. Event duration is four frames.

To determine the frames at which the event occurs, we first put the event 10–30 frames (randomly) after the ROI occurs. Spatial distance of this event from others must be ≥ 3 pixels and temporal distance ≥ 4 frames. Part of the event may be inside the spatial footprint of other ROIs, as long as its spatiotemporal distance to other events is larger than the threshold set above. Events are generated for each ROI; on average, we simulate 250 frames with 800 events on 90 ROIs.

Simulation dataset 2 (location-changing events): To simulate event location changes, we generate events with the same size for each ROI and shift them to nearby locations. Thus, each ROI (450–550 pixel size) is related to multiple events near to that ROI. Denote *dist* the distance between the event center and the ROI center. Denote *diam* the diameter of the ROI. The degree of location change is quantified by the ratio between *dist* and *diam*. For example, if we set 0.5 as the maximum degree of location change, the distance of the center of a new event to the ROI will be 0–0.5 times the diameter of the ROI. If the ratio is 0, we simulate a pure ROI dataset. The new event may be located any direction from the ROI, randomly picked from $0-2\pi$. Shapes of new events are randomly picked from the templates, so may be different from the ROI while size is constant. Event duration is four frames, and the remaining steps are the same as above. On average, we simulate 250 frames with 800 events on 90 ROIs.

Simulation dataset 3 (propagating events): We simulated two types of propagation: growing and moving, leading to three types of synthetic datasets: growing only, moving only, and mixed. These three types are generated similarly. The ROI map is generated as above, and ROI sizes are 4,000–10,000 pixels, with events generated inside each ROI. In comparison, events in the size-change and location-change simulations can be (fully or partially) outside their corresponding ROIs. We simulate only one seed (starting propagation point) in each ROI. For each event, we generate a rise-time map (for each pixel in the ROI) and construct event-propagation based on the map. We obtain this map by simulating a growing process starting from the seed pixel, with the seed pixel active at the first time-point. At the next time point, its neighboring pixels are active with a variable success probability. Growth continues until $\geq 90\%$ of pixels in the ROI are included in the event. Based on the rise-time map, we identify frames at which pixels become

active in the event. To determine when the event ends, we treat growing and moving propagation differently. In growing propagation, all pixels are inactive simultaneously 2 frames after the last pixel becomes active. For moving propagation, the duration is 5 frames. Typically, we generate approximately 140 events in 14 ROIs for each synthetic dataset.

Simulate various SNRs: Gaussian noise is added to the synthetic data to achieve various SNRs.

We define the signal intensity as the average of all active pixels in all frames. SNR is defined as

$$20 \times \log_{10} \frac{\text{average signal intensity}}{\text{noise standard deviation}}$$

When we change the degree of location change, size change, and propagation duration, we add noise with 10 dB SNR. To study the impact of SNR on size changes, size-change degree is 3. For location changes, distance-change ratio is 0.5 while varying SNRs. For propagation, propagation duration is 5 frames. Seven SNRs are tested: 0, 2.5, 5, 7.5, 10, 15, 20 (all in dB).

Post-processing simulated data: We set the average signal intensity at 0.2, with a range from 0–1. Synthetic data is spatially filtered to mimic blurred boundaries in real data. The smoothing is performed with a Gaussian filter with a standard deviation of 1. Signals with intensity <0.05 after smoothing are removed. Remaining signals are temporally filtered with a kernel with a decay τ of 0.6 frames. The rising kernel is linear. For propagation simulation, data is down-sampled by five. Next, we perform a cleaning step. For each pixel in each event, we find the highest intensity (x_{peak}) across frames. For that pixel, we set signals that are <0.2 times of x_{peak} to 0. Finally, a uniform background intensity of 0.2 is added (except for GECl-quant, where no background is added; see below).

Application of AQuA and peer methods on the simulation data sets

Based on our knowledge about simulated datasets, we apply specific considerations for each analytical method in order to set optimal parameters for each. In this way, we aim to assess the methodological limit of each method, rather than suboptimal performance due to inadequate parameter-setting. We expect that the performance of the peer methods on simulation data is an overestimate of their performance on real experimental data, because here we take advantage of the ground-truth knowledge, which is not available for experimental astrocyte data.

Event detection using peer methods: AQuA and CaSCaDe report detected events, while other methods report detected ROIs. For a consistent comparison, we detect events from those methods that use ROIs. Once ROIs are detected, we calculate the average dF/F curve for each ROI, as follows: The curve is temporally smoothed with a time-window of 20. The minimum value in the smoothed curve is considered baseline. Assume the minimum value occurs at time t_{base} . The baseline is then subtracted to obtain the dF curve. The noise standard deviation σ is estimated using 40 frames around t_{base} . We then obtain a z-score curve as dF/σ . A large z-score indicates an event; we use a z-score threshold of z_0 . The value z_0 is set according to ground-truth knowledge, so that the smallest-size event in the simulation data is detected by this threshold. Denote x_0 and s_0 the peak intensity and the size for the smallest event in the ground truth. We also denote the ground truth noise level as σ_0 . Then, the threshold is calculated as,

$$z_0 = \min \left(\frac{0.9x_0\sqrt{s_0}}{\sigma_0}, 10 \right).$$

We clip the score to 10 to avoid setting large values for high SNR. For CaSCaDe, we supply this value as the peak intensity threshold parameter.

Using the z-score curves and threshold, we detect events from ROIs for CaImAn, Suite2P, and GECI-quant. For each z-score curve, we find all frames with values $>z_0$. Each frame is a seed for an event. Assume the z-score for that frame is z_1 and we search before and after that frame. If the intensity of the frame is $\geq 0.2z_1$, the frame is associated with the event. If we meet frames with intensities $< 0.2z_1$, we stop searching that direction. Once finished, we obtain all frames associated with the event. We continue with another seed frame to find another event. Note that if a frame is considered part of an event, we do not consider it as a seed for another event, even if it is $>z_0$. The spatial footprint is fixed for all frames in an event, based on the ROI detected. Combining spatial footprint and frames, we obtain events for each ROI and identify all voxels belonging to an event.

Parameter setting for AQuA: The parameters of AQuA are based on the ex-vivo-GCaMP-cyto preset with the following modifications: For different noise levels (SNR), we apply different smoothness levels. The smoothing is performed only spatially and values are empirically chosen. The smoothness parameter is the standard deviation of the Gaussian smoothing kernel used.

Extended Data Table 2.1. Parameter setting for AQuA

The smoothness parameter used in AQuA for each noise level (SNR) in the simulated data.

SNR (dB)	0	2.5	5	7.5	10	15	20
Smoothness	1	0.9	0.8	0.7	0.6	0.5	0.1

We do not simulate motion of the field-of-view, so we do not discard any boundary pixels, and we set $regMaskGap = 0$. We do not simulate Poisson Gaussian noise; we use additional Gaussian noise only, so $PG = 0$. Event sizes in the simulation are >200 pixels, so we set the minimum event size to be a value much smaller: $minSize = 16$. An event may not have

more than one peak, so we set $cOver = 0$. We do not simulate temporally adjacent events, so we set $thrTWScl = 4$. We do not use proofreading, so we choose a more stringent z-score of events: $zThr = 5$.

Specific considerations for CaSCaDe: We use the following parameters for CaSCaDe:

According to the duration and temporal distances of the simulated events, we can safely set peak distance $p.min_peak_dist_ed = 3$ and minimum peak length $p.min_peak_length = 2$. We set the spatial smoothing filter size in the 3D smoothing function ($bpass3d_v1$) according to the size of the event, so we set $p.hb$ equal to 2x median of the radius of the spatial footprint of all events.

We use this setting because the default settings could not detect larger events on the simulation data sets. For temporal smoothing, we set $p.zhb=21$. We do not need to correct background, so we set $p.int_correct= 0$. The minimum peak intensity is $p.peak_int_ed = z0$, as discussed above. Minimum event intensity is $p.min_int_ed = \min(2, p.peak_int_ed * 0.2)$. We modified the low-frequency part of the watershed segmentation step to allow larger events to be detected, by changing the function $bpassW$ inside the function $domain_segment$. We replaced the noise estimator in CaSCaDe (function $estibkg$) with the more robust one used by AQUA.

CaSCaDe uses a supervised approach to classify detected events. Instead of manually labeling a large number of events and training many SVM models, we directly use ground truth to perform training. For example, for each event detected by CaSCaDe, we check the ground-truth data to test whether it is (part of) a true event. If so, it is retained; otherwise, it is discarded.

Specific considerations for GECI-quant: GECI-quant requires user input at each step. Here, we describe how to automate these steps by taking advantage of ground-truth information. This allows us to test many conditions and repeat many times.

First, we do not add background signals to the synthetic data, so background subtraction is ignored. The domain- and the soma-detection steps require manual thresholding. We estimate the best threshold using the ground-truth data for each simulation. To do so, we scan 255 thresholds and use the one that leads to the best correlation between binarized data and ground truth. We next cleaned the binarized signals with sizes <4 pixels. The data here is also smoothed as it is in GECI-quant (3x3 spatial averaging). Events with spatial footprints $< 1,000$ pixels are treated as domains and others are treated as somas. The soma segmentation step also uses a threshold. We first process the data as in GECI-quant: for every three frames, a standard-deviation map is calculated so that each voxel in ground-truth data is associated with a standard deviation value. The average of all standard deviations from the ground-truth data is used as the threshold.

We next made the entire analysis pipeline automatic. Fiji is called from the command line in each step and parameters are passed as well. The final ROIs from Fiji are brought back into MATLAB. ROIs are > 15 pixels in area. All other parameters are unchanged, including those for the particle detector. Note that this modification cannot be used as an automated version of GECI-quant for real applications since it relies on ground-truth information.

Specific considerations for CalmAn: We experimented with different parameters for CalmAn and found the following set of parameters performed best on simulation data. As event size can be large, we enlarge the patch size, so `patch_size = [128,128]` and `overlap = [32,32]`.

Components to be found is set to $K = 50$. The standard deviation of the Gaussian kernel (half size of a neuron) is enlarged to $\tau = 16$. Maximum size is 5,000 and the minimum size is 25. Decay time is 0.5. Other parameters are based on default settings. No spatial or temporal down-sampling is used. Adjusting these parameters does not impact results on our simulated data. We used the 5/5/2018 version downloaded from <https://github.com/flatironinstitute/CaImAn-MATLAB>.

Specific consideration for Suite2P: The most critical parameter for Suite2P is neuron size. We set `db.diameter` equal to the minimum between 50 and the median of the radius of the spatial footprint of all events. Setting the diameter too large leads to an out-of-memory issue. We bypass the registration step. We used the 6/4/18 version downloaded from <https://github.com/cortex-lab/Suite2P>.

Performance evaluation on the simulated data

To evaluate the accuracy of detected events, we quantify the intersection over the union (IoU). We consider all event voxels, not only pixels as in ROI-based methods. For each detected event i , we find all the ground-truth events that have common voxels with event i . For each such ground-truth event, e.g., event j , we calculate an IoU score (also known as Jaccard index) between this pair of events as the following,

$$IoU_{i,j} = \frac{\text{Number}(\text{Voxels in event } i \cap \text{Voxels in event } j)}{\text{Number}(\text{Voxels in event } i \cup \text{Voxels in event } j)}$$

When a detected event can be perfectly matched with a ground-truth event, its IoU score is 1. A score of 0 indicates this pair of events has nothing in common. For each detected event i , we find the maximum IoU score among all pairs between this event and a ground-truth event. We denote

this maximum score as IoU_i . Similarly, we can compute a score IoU_j for the ground truth event j . The final IoU score is obtained by averaging over all events, including detected and ground-truth events. Supposing we have I detected events and J ground truth events, where I and J are not necessarily equal, we compute the final score as the following,

$$IoU = \frac{\sum_{i=1}^I IoU_i + \sum_{j=1}^J IoU_j}{I + J}$$

All simulation is performed on a workstation with 16 cores, 128 GB RAM and 6TB hard drive. We use MATLAB 2018a on Windows 10 Enterprise Edition. GECI-quant is run on Fiji with ImageJ version 1.52h. Each simulation is repeated 10 times. The mean and 95% confidence interval (CI) of IoU score is calculated and plotted. The CI is calculated as $[\mu_{sim} - 2\sigma_{sim}, \mu_{sim} + 2\sigma_{sim}]$, where μ_{sim} is the estimated mean and σ_{sim} is the estimated standard deviation (σ_{sim}) based on 10 repetitive runs.

Open-source software for analyzing and visualizing dynamic fluorescent signals in astrocytes.

Applying software engineering principles, we developed an open-source toolbox for astrocyte fluorescent imaging data with detailed user guidelines. The software not only implements the AQUA algorithm for detecting events, but also provides an integrated environment for users to see the results, interact with the analysis, and combine other types of data such as cell/region masks and landmarks. There are two versions of the software with the same functionality, based on MATLAB or Fiji. The software is freely available at <https://github.com/yu-lab-vt/aqua> where detailed documents and example applications can be found. A list of extracted features is shown in Supp. Table 5. Here, we highlight several important functions of the software.

First, the software implements AQUA and provides several options to export the event-detection results, including TIFF files with color-coded events, event features in Excel, and

MATLAB or Java data structures to be used by other programs. Second, the software can display analysis results by adding color to the raw video, where color encodes the value of a user-defined extracted feature such as propagation speed. Users can specify which feature to be displayed, either an existing feature in AQuA or a user-designed feature based on features provided by AQuA. We provide several pre-defined colormaps, but allow users to manually define colormaps as well. AQuA also provides a side-by-side view, to simultaneously display two features or a raw video plus one feature. Third, the software provides a convenient way to interactively view detected events and their associated features. By clicking on an event, the dF/F curve for the event is shown in a separate panel below the video, and the time-frames during which the event occurs are highlighted in red. The values of several other features for that event are also shown in another panel. The software allows multiple events to be selected simultaneously, so that their curves and features can be plotted together and compared. Fourth, the software provides both automatic and manual ways to proofread the results. For automatic proofreading, events are filtered by setting desired ranges for features-of-interest. Alternatively, users can choose the ‘delete/restore’ button and manually click an event to remove it. Fifth, the software provides flexible ways to incorporate cell morphology or landmark information. Users can manually supply cell morphology or regional information such as the cell boundary, which can assign events to individual cells. Users can also provide landmark information such as the location of a pipette for pharmacological application. Users can also load cell, region, or landmark information from other data sources, such as another fluorescence channel that captures cell morphology. The software can extract landmark-related features for each event, including the direction of propagation relative to a landmark.

Figures

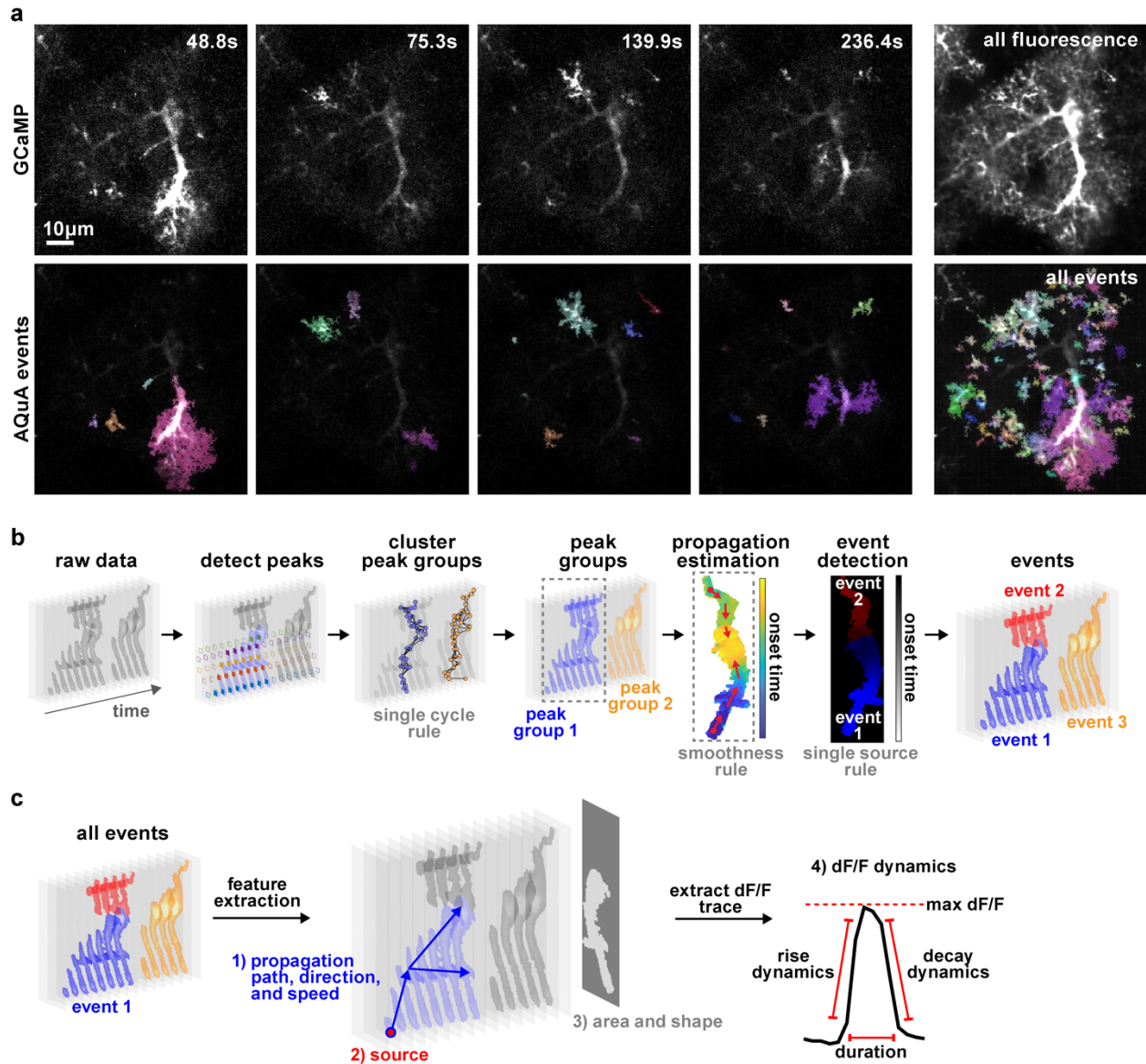


Figure 2.1. AQuA-based event detection.

(a) Individual representative frames from 5-min *ex vivo* astrocytic GCaMP imaging experiment (top), with AQuA-detected events shown below. Each color represents individual event and is chosen at random. Right column shows the average GCaMP fluorescence (top) and all AQuA-detected events (bottom) from the entire movie. Note that contrast is different between rows to highlight events. (b) Flowchart of AQuA algorithm. Raw data is visualized as a stack of images across time with grey level indicating signal intensity. In the *detect peaks* panel, five peaks are detected and highlighted by solid diamonds, each color denoting one peak. Based on the single-cycle rule and spatial adjacency of the apexes (solid dots) of each peak, peaks are clustered into spatially disconnected groups. Based on smoothness, propagation patterns are

Figure 2.1 continued on next page

Figure 2.1 continued

estimated for each peak group. By applying the single-source rule, two events are detected for peak group 1. Three total events are detected. (c) Feature extraction. Based on the event-detection results, AQUA outputs four sets of features relevant to astrocytic activity: 1) propagation-related (path, direction, and speed); 2) source of events, indicating where an event is initiated; 3) features related to the event footprint, including area and shape. Event 2 is plotted here; 4) features derived from the dF/F dynamics.

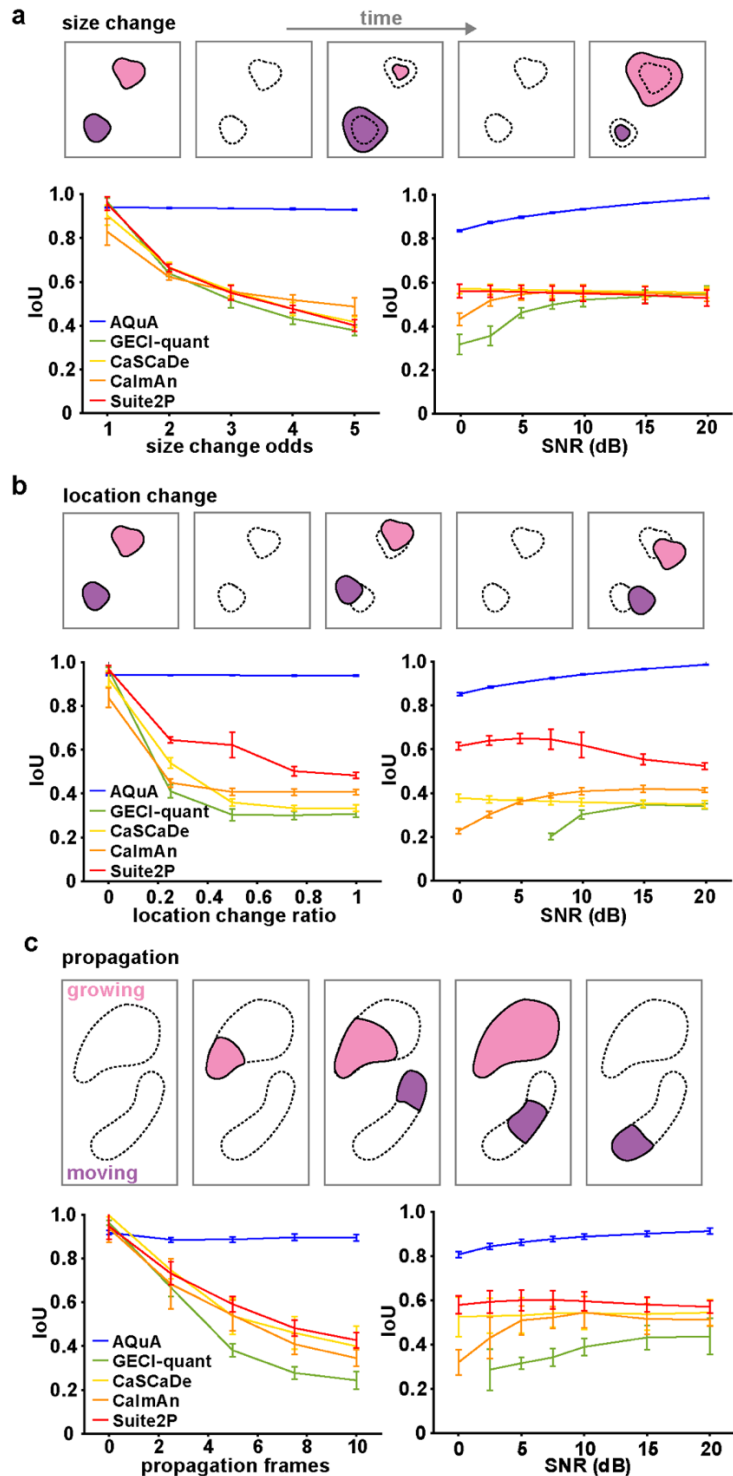


Figure 2.2. Performance comparison among image-analysis methods.

(a–c) Schematic (top) and results (bottom) of performance of five image analysis methods (AQuA, GECI-quant, CaSCaDe, CalmAn, and Suite2P) on simulated datasets, independently changing event size (a), location (b), and propagation duration (c). In results, change of independent parameter is shown in left panel, and varying SNR in right. For each result, the *Figure 2.2 continued on next page*

Figure 2.2 continued

smallest value of the independent parameter corresponds to a simulation under pure ROI assumptions. The larger the values, the greater the violation of the ROI assumptions. IoU (intersection over union) measures the overlap between detected and ground-truth events. An IoU=1 is the best achievable performance, meaning that all detected events are ground-truth and all ground-truth events are detected. Error bars indicate the 95% confidence interval calculated from 10 independent replications of simulation, where each simulation contains hundreds of events.

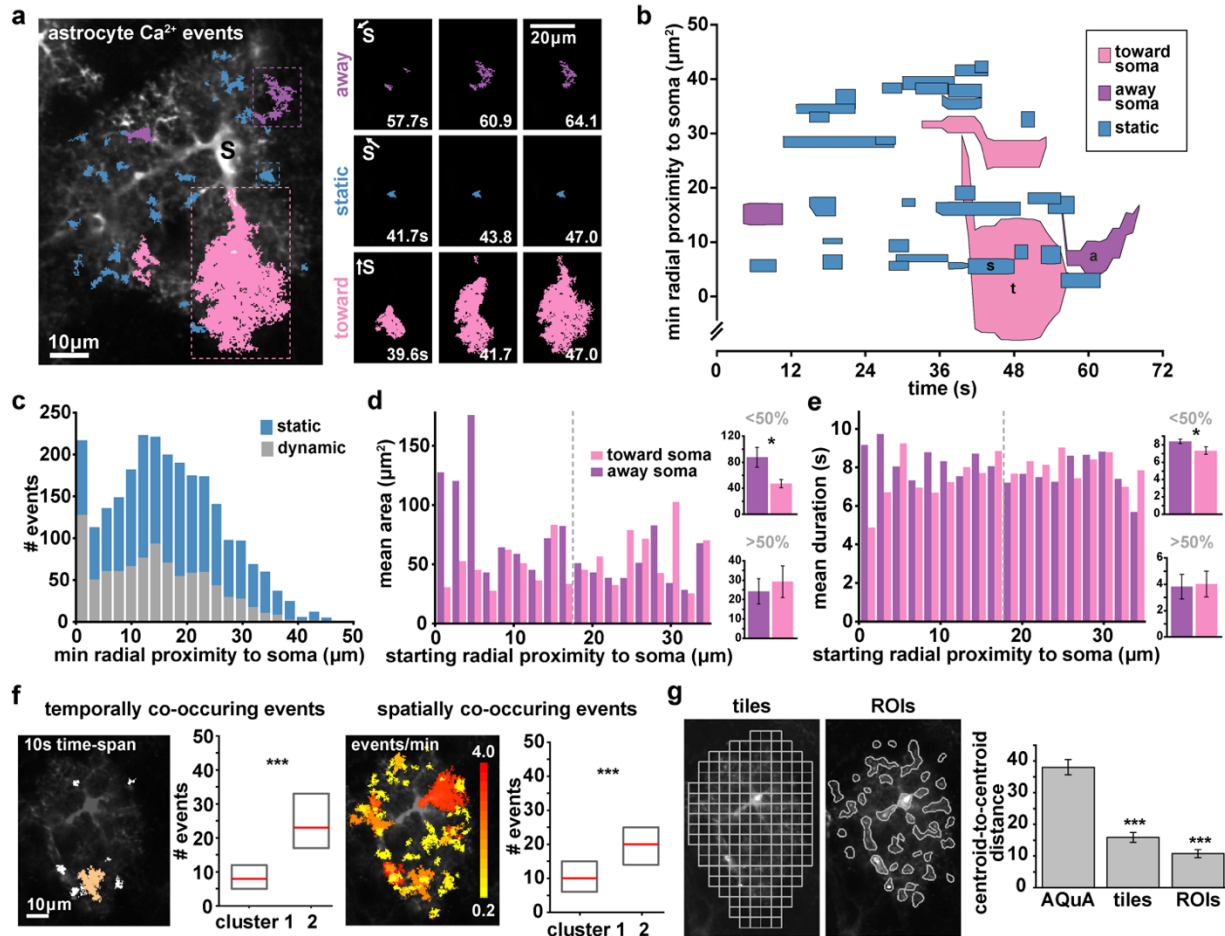


Figure 2.3. AQuA features capture heterogeneities among single astrocytes.

(a) Representative GCaMP6f *ex vivo* image (left) with AQuA events overlaid from 1 min of a 5 min movie. Soma marked with black s. Right: Representative image sequence for each propagation direction class (blue = static, pink = toward soma, purple = away from soma). Soma direction marked with s and white arrow. (b) Spatiotemporal plot of Ca^{2+} activity from 1 min of movie. Each event is represented by a polygon that is proportional to its area as it changes over its lifetime. (c) Distribution of dynamic and static events as a function of minimum distance from soma (chi-square test, $***p < 0.001$, $n = 5$ slices, 11 cells). All bin widths calculated by Freedman-Diaconis's rule. (d) Left: Propagative event size versus starting distance from soma, segregated by propagation direction. Dashed gray line denotes half the distance between the soma and the cell border. Right: Average event area for those that start $< 50\%$ (top) and $> 50\%$ (bottom) of the distance from the soma, (one-tailed paired t-test, $*p < 0.05$). (e) Left: Event duration versus starting distance from soma. Right: Average event duration for those that start $< 50\%$ (top) and $> 50\%$ (bottom) of the distance from the soma (one-tailed paired t-test, $*p < 0.05$). (f) Two event-based measurements of frequency: events with activity overlapping in time (left) and in space (right;). Left: one example event (orange) co-occurs with six other events (white) within 10s. Right: event colors indicate event number/min (0.2–4) at each location. Median (red) and interquartile range (gray) from cells in each cluster in Extended Data Fig. 2.9 (one-tailed Wilcoxon rank sum, $***p < 0.001$). (g) Quantification of centroid distances between cells from two clusters determined by t-SNE plots of Ca^{2+} activity using features calculated from ROIs and $5 \times 5 \mu\text{m}$ tiles (top), (bottom, one-tailed paired t-test, $***p < 0.001$).

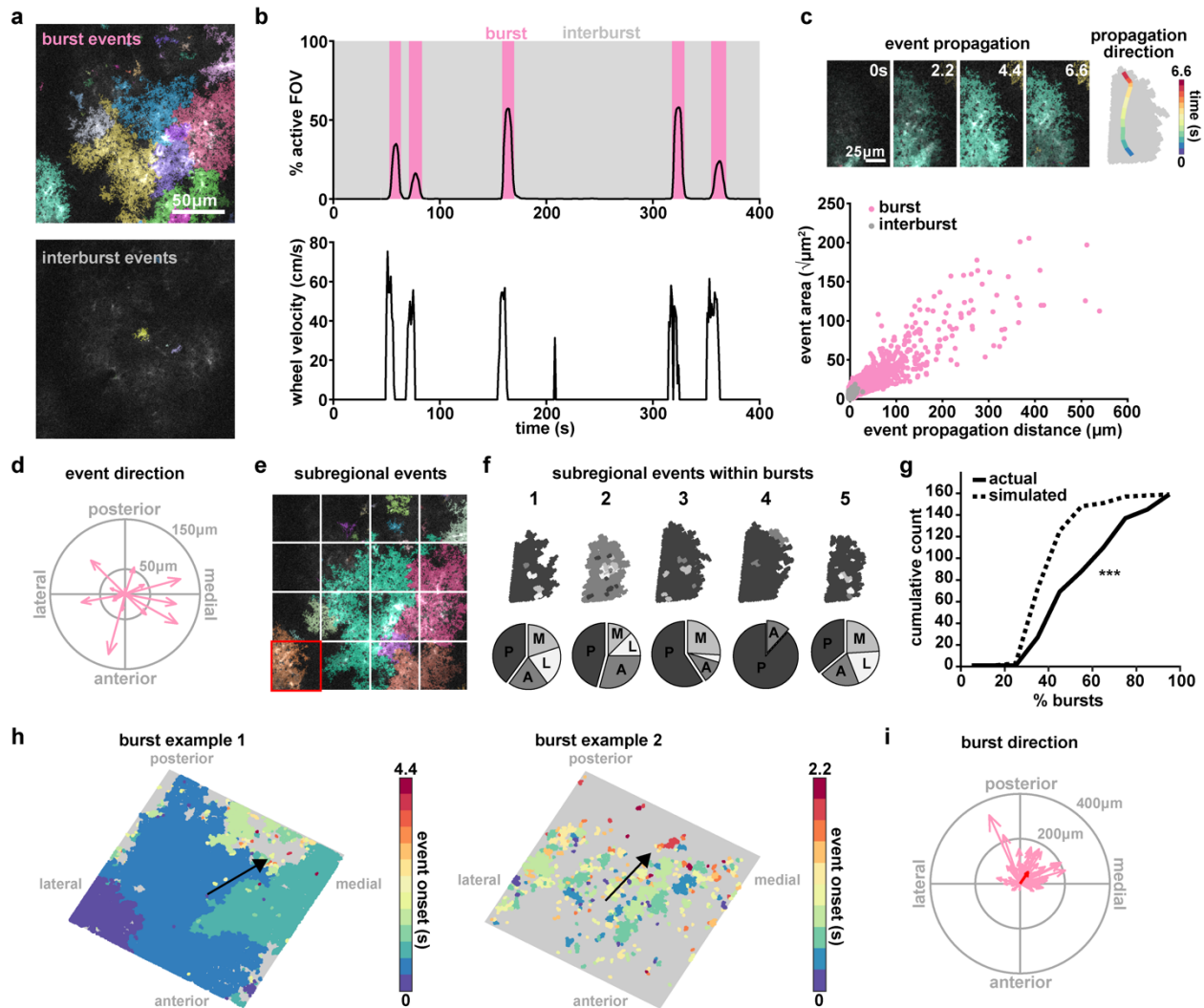


Figure 2.4. AQuA resolves astrocytic Ca^{2+} propagation directionality across scales. (a) Representative *in vivo* GCaMP6f images during a burst period (top) and inter-burst period (bottom) with overlaid AQuA-detected events. (b) Population Ca^{2+} events represented as percentage of the imaging field active as a function of time. Burst periods (pink) are identified when Ca^{2+} activity exceeds more than 1% of the active field of view and exceeds more than 10% of the maximum number of event onsets. (c) *In vivo* Ca^{2+} events propagate with specific directionality. Top: representative propagative event that occurred during the burst period in panel a. The propagation direction (change of centroid relative to its original location) for each frame is overlaid on the event (right). Bottom: Total propagation distance versus event size for all events within bursts ($n=6$ mice, 66 bursts, 14,967 events). (d) Event propagation direction from all events over the entire field in the burst shown in e. Length of arrow indicates propagation distance. (e) To test consistency of subregional directionality during bursts, sixteen $96 \times 96 \mu\text{m}$ tiles are overlaid on images. (f) Top: All events within highlighted tile in d (red square) for five burst periods, color-coded by propagation direction (top). Bottom: Event propagation direction distributions (P=posterior; A=anterior; M=medial; L=lateral). (g) Cumulative count versus percentage of bursts for actual (solid line) and simulated (dotted line) events. *** indicates statistical significance. (h) Event onset maps for two burst examples, showing event onset time (s) across the field. (i) Burst directionality in a circular plot.

Figure 2.4 continued on next page

Figure 2.4 continued

(g) Cumulative distribution of percentage of bursts with events (within individual tiles/regions) propagating in the same direction in actual (solid) and simulated (dashed) data (one-tailed Wilcoxon rank sum, *** $p < 0.001$) (h) Two representative maps of population burst propagation direction with each event color-coded by their onset time relative to the beginning of the burst period, demonstrating variability of burst size. (i) Burst propagation direction calculated from onset maps in h ($n=66$ bursts). Event locations from the first 20% of the frames after burst onset are averaged together to determine burst origin. Event locations from 20% of the last frames after burst onset are averaged together and the difference between this and the origin determines burst propagation distance. Red arrow denotes average of all bursts.

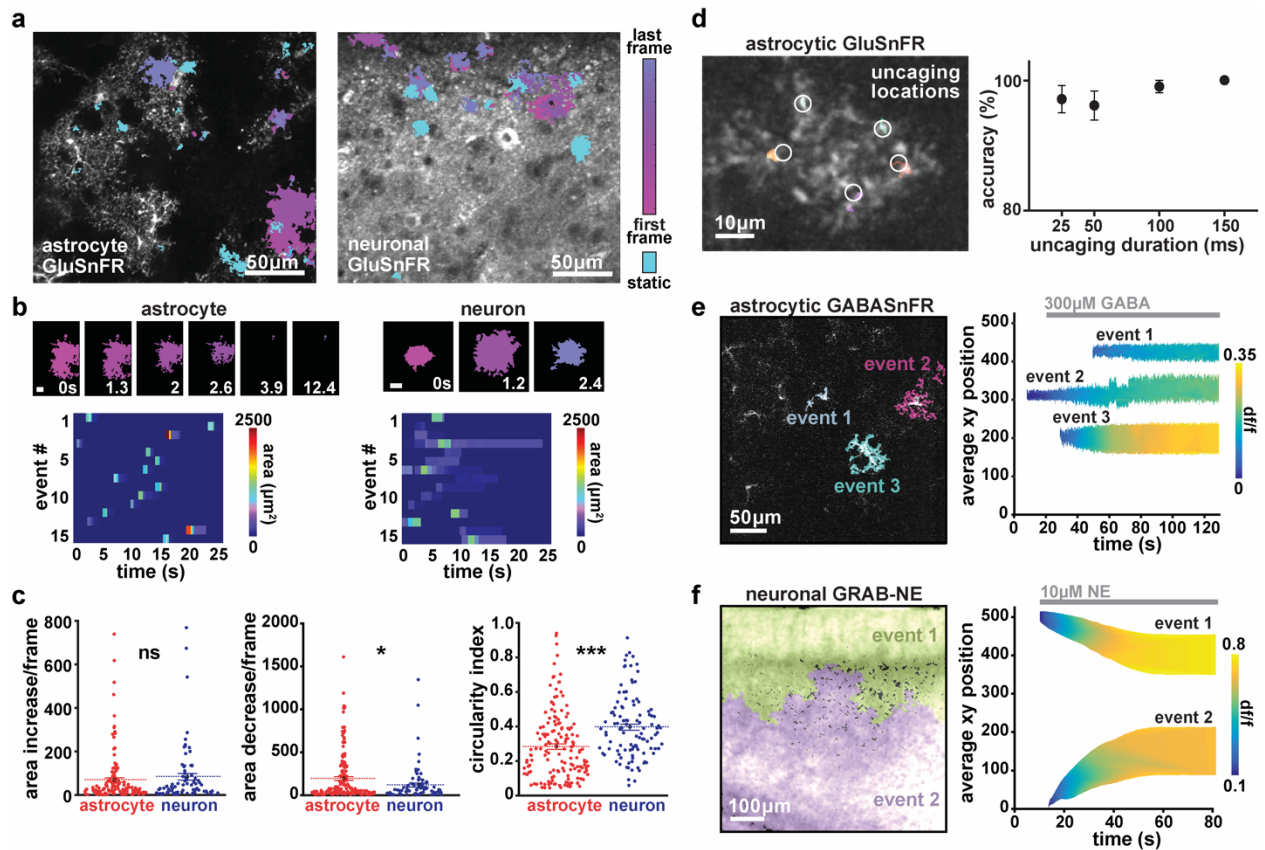
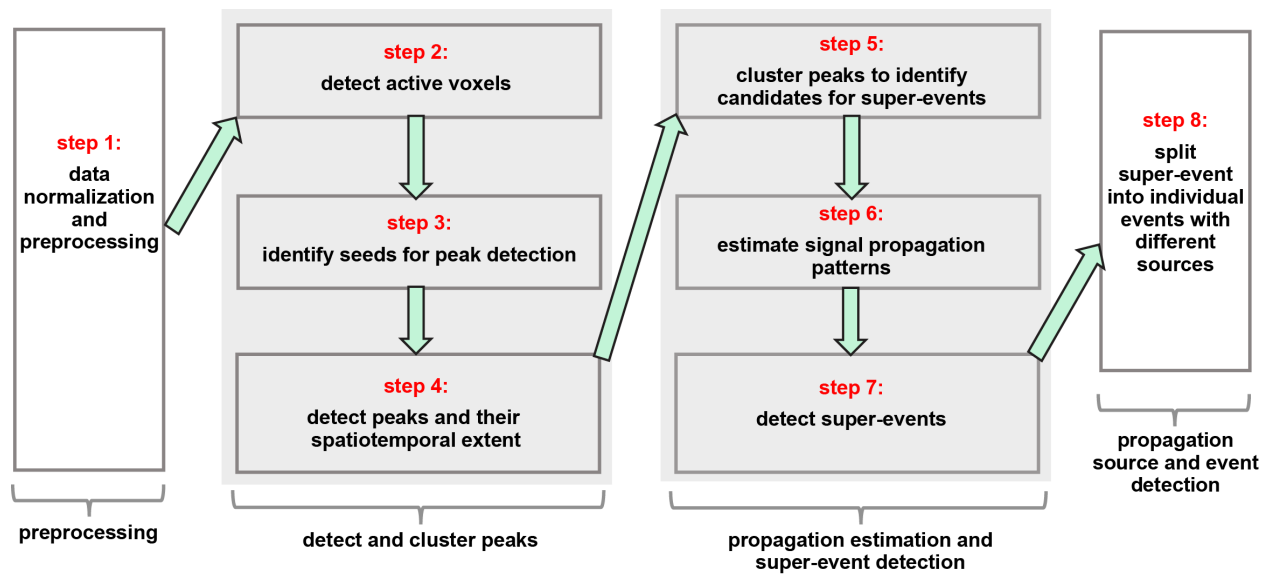


Figure 2.5. AQuA-based detection of extracellular dynamics via astrocytic and neuronal expression of genetically encoded neurotransmitter sensors.

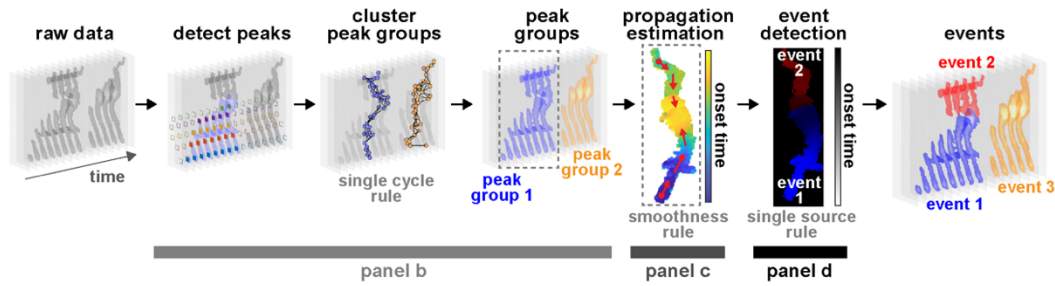
(a) Representative images of *ex vivo* slices with expression of astrocytic (left) or neuronal (right) GluSnFR. Color indicates detected events. Those with dynamic shape are shown in magenta, and static events in cyan. (b) Examples of timecourse of astrocytic (left, top) and neuronal (right, top) glutamate events. Scale bar = 10 μ m. Raster plot of area of astrocytic (left, bottom) and neuronal (right, bottom) glutamate events. (c) Size dynamics (area increase [left] and decrease [middle] per frame) and shape (circularity index, right) of glutamate events when GluSnFR is expressed on astrocytes (red) or neurons (blue). (d) Left: Single astrocyte expressing GluSnFR, with AQuA-detected events (colors) with ~100Hz frame rate imaging and 25–150ms uncaging of RuBi-glutamate. Uncaging locations marked with white circles. Right: Percent correct events detected by AQuA, depending on duration of the laser uncaging pulse. (e) Example of three AQuA-detected events at single timepoint (97s) after addition of 300 μ M GABA to slice with astrocytes expressing GABASnFR (left). Right: Detected events before and after addition of 300 μ M GABA (gray bar) to circulating bath. Events are plotted to display spatial position in imaging field (y-axis), event area (height), and gradually increasing amplitude (color) over time. (f) Left: two detected events in cortical slice expressing GRAB-NE in neurons after addition of 10 μ M NE. Right: Events plotted to display spatial position (y-axis), event area (height), and amplitude (color) dynamics over the course of the experiment. In (e) and (f), average xy position at each timepoint is calculated using the following equation: $\frac{((xLoc-1)*frameSize) + yLoc}{frameSize}$.



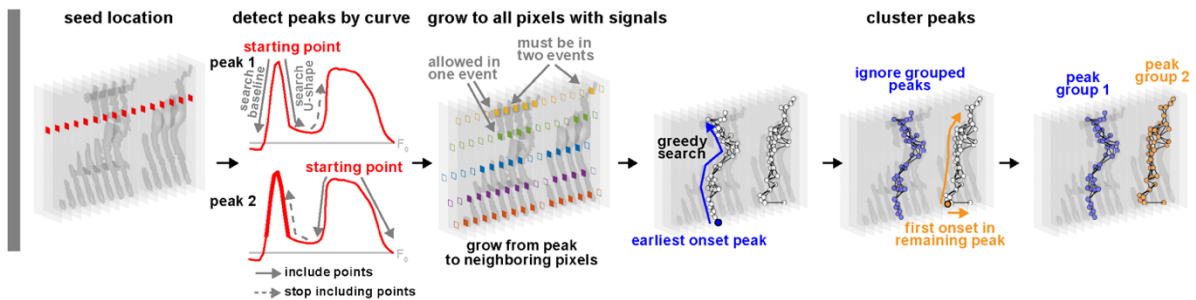
Extended Data Figure 2.1: Eight steps in the AQa algorithm.

The eight steps can be grouped into four modules indicated by brackets below panels. The last three modules are further illustrated in Extended Data Fig. 2.2.

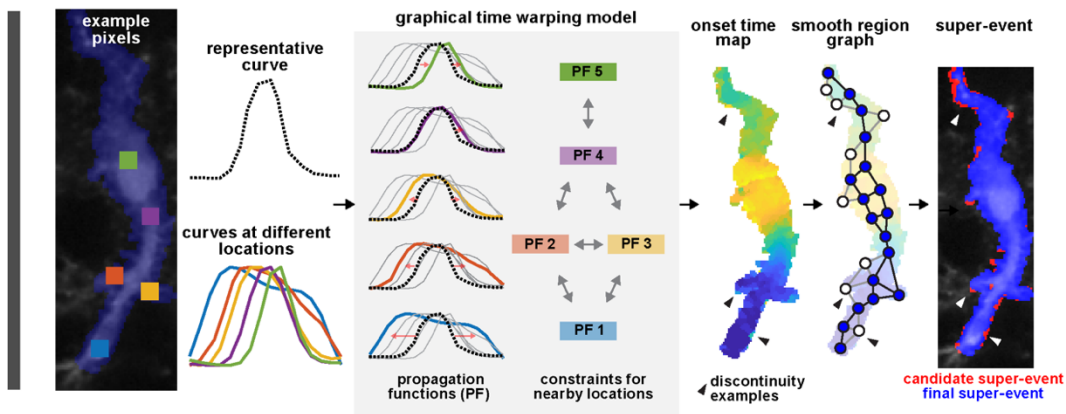
a AQUa flowchart



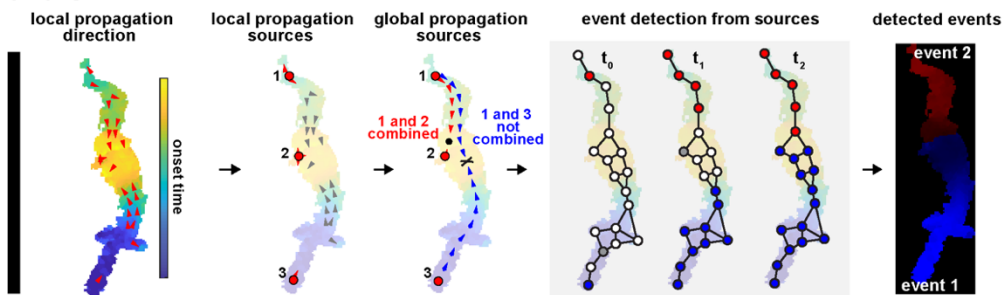
b detect and cluster peaks



c propagation estimation and super-event detection



d propagation source and event detection

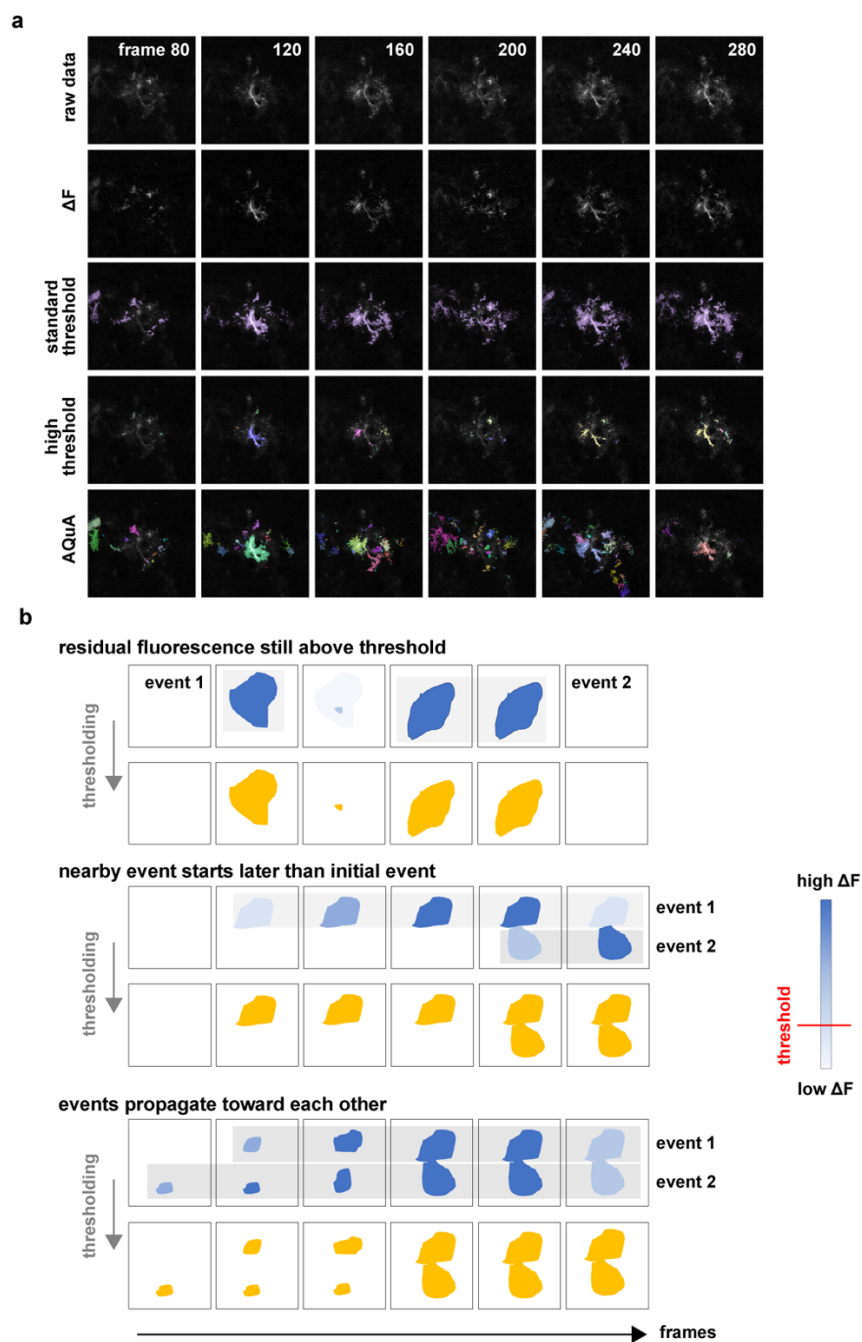


Extended Data Figure 2.2: Schematic illustration of three major modules in AQUa algorithm.

Curves and regions taken from a real data set. (a) AQUa flowchart, with three gray bars below indicating where the three major modules are located with respect to the AQUa
 Extended Data Figure 2.2 continued on next page

Extended Data Figure 2.2 continued

flowchart. **(b) detect and cluster peaks:** curves in the *detect peaks by curve* panel are associated with the location labeled by the red diamond in the *seed location* panel. One curve may have multiple peaks, which are detected one-by-one. Once a peak is detected at a seed location, the peak is spatially extended to include its neighboring pixels as in the *grow to all pixels with signals* panel. Clustering of peaks starts from the peak with the earliest onset time and includes its spatially adjacent peaks based on the two inclusion rules shown in the *grow to all pixels with signals* panel. Two peaks at one location are never clustered into one group. Once the greedy search strategy can't find more peaks to include, it stops and one peak group is formed. Then, to find another peak group, the greedy search restarts from the first onset in the remaining peaks. The process is repeated until no peaks remain. **(c) Propagation estimation and super-event detection:** This module is applied to each peak group. The five colored curves are the dynamics of the five exemplar pixels with corresponding colors. The dashed curve is the representative or reference curve. In the *graphical time warping model* panel, red arrows indicate how the reference curve can be warped to represent the curve at each location. The graphical time warping model incorporates the information that nearby locations should have more similar curves than distant locations. A double-headed arrow between two functions informs the model that these curves should be warped similarly to the reference curve. As a comparison, if there is no double-headed arrow between curves, dissimilar warping functions are allowed. Once the warping function is calculated by the graphical time warping model, onset time is computed for each pixel, resulting in an onset time map. Note discontinuity of onset time examples at black triangles. These pixels are removed to obtain the final super-event, which may contain multiple events and are subject to the next operation. **(d) Propagation source and event detection:** Local propagation sources are obtained by finding local minima on the onset time map. According to the rules described in Methods, some local sources will be combined/merged, resulting in global propagation sources. Briefly, if the path between two local sources does not have to go through a location with a late onset time, these two local sources are combined. Then, each global propagation source leads to an event. Each event is obtained by growing each global source to include its neighboring pixels. In the *event detection from sources* panel, solid dots are pixels already assigned to an event, white dots are unexplored pixels, and grey dots are explored but await a later decision to be assigned to an event.



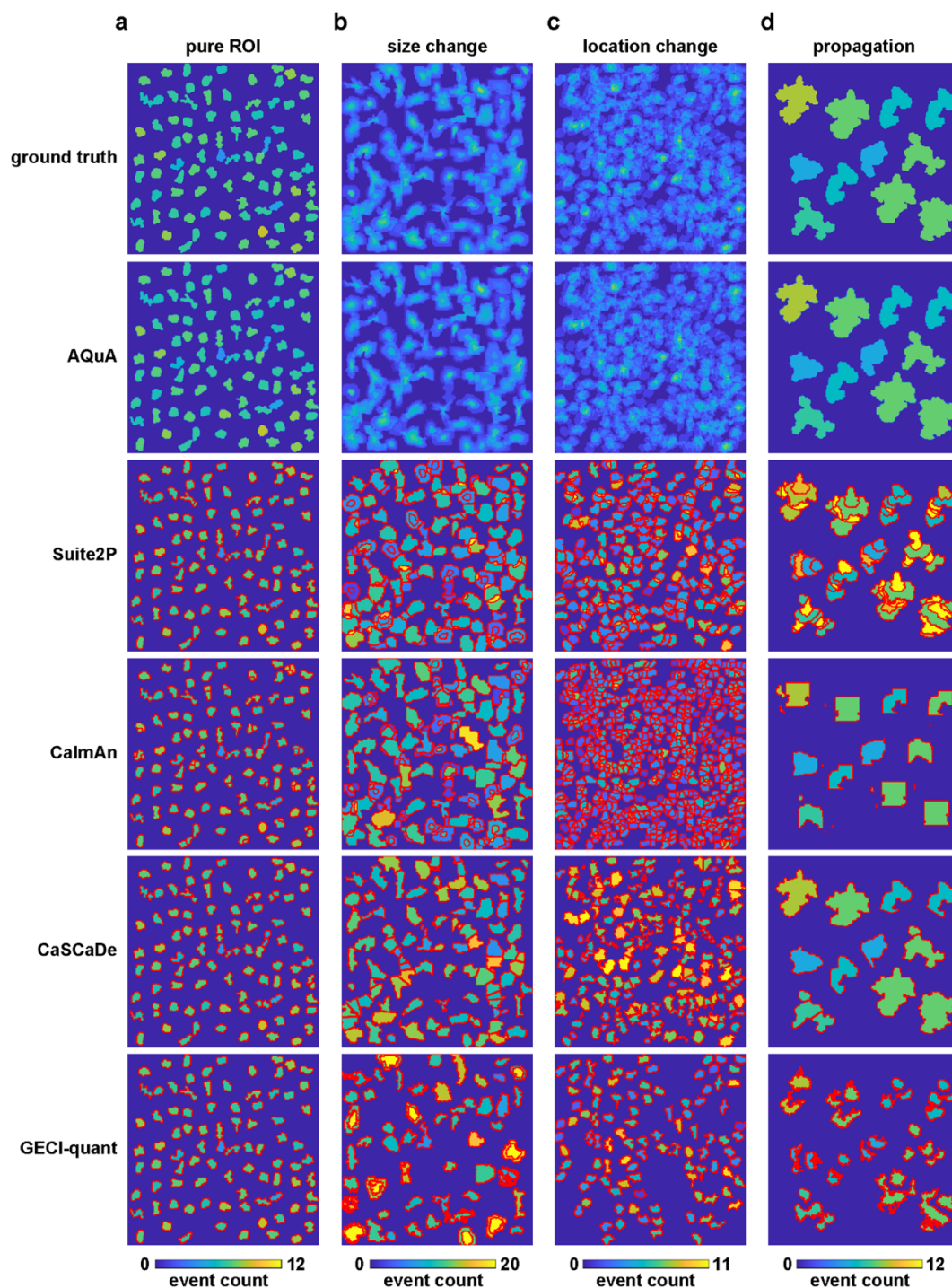
Extended Data Figure 2.3: Limitations of thresholding-based analysis.

(a) *Top row*: Six example frames of *ex vivo* data smoothed with a Gaussian kernel of $\sigma=0.5$ after square root transformation. *Second row*: Baseline for each pixel is estimated with a 20-frame time window, noise level is estimated as σ_{noise} , and baseline is subtracted from raw data to obtain ΔF . *Third row*: Standard threshold is set at $3\sigma_{\text{noise}}$. Many individual events are erroneously detected as one very long and large spatiotemporal component, for reasons graphically explained in (b). *Fourth row*: A high threshold ($10\sigma_{\text{noise}}$) leads to loss of many true events, and many detected events are incomplete. Each color indicates an event. *Fifth row*: AQuA-detection avoids the pitfalls in threshold-setting and identifies each individual event.

Extended Data Figure 2.3 continued on next page

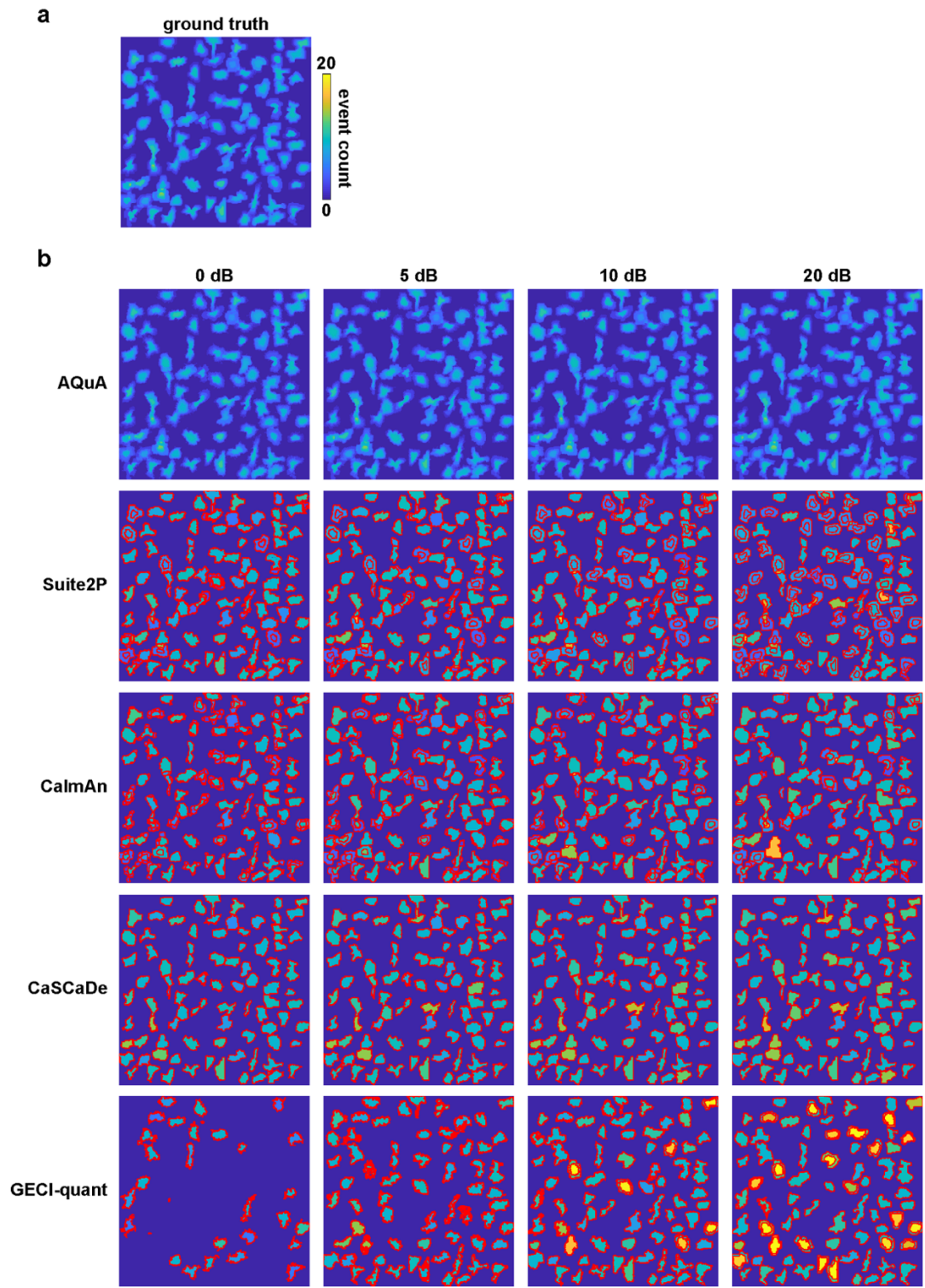
Extended Data Figure 2.3 continued

(b) Two events are incorrectly connected after thresholding (incorrect events in yellow in each sub-panel). Intensity color bar on right, with red indicating the threshold, refers to all panels. *Top:* Between multiple events in the same location, even though the intensity drops a lot, not all pixels will fall below the threshold. Each event is shown with a gray bounding box. The super-voxel step in AQuA solves this problem by finding a time window for each seed, and spatially extending the windows. *Middle:* Neighboring events are initiated at distinct times, but are spatiotemporally connected at a later time. If two regions have very different onset times, AQuA will treat them as different events in the super-event detection step. *Bottom:* Two events can be separated when they appear, but meet after propagating. In the event detection step, AQuA distinguishes these events based on the single-source rule.



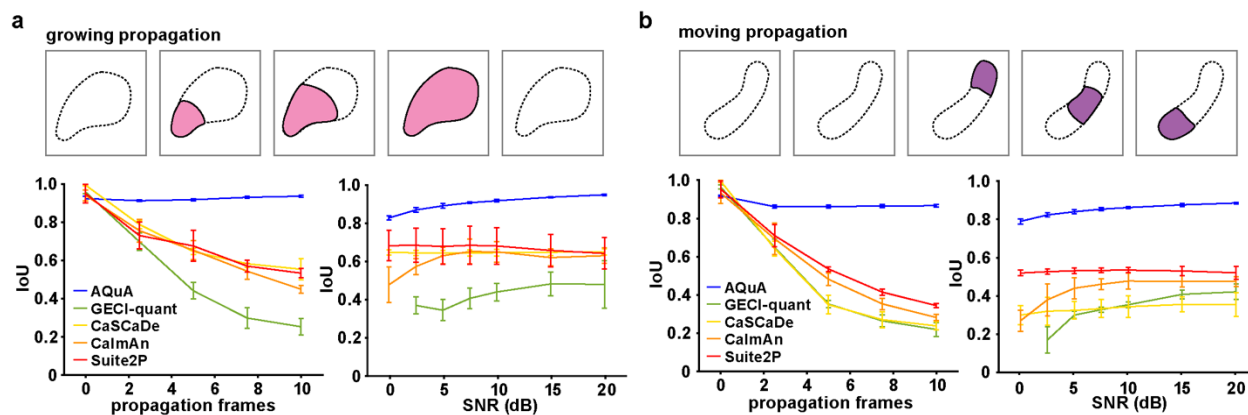
Extended Data Figure 2.4: AQuA detects ground truth events across three types of simulated data.

Color represents event count for each pixel (note colors bars have different scales in each dataset). Red borders show ROIs detected by ROI-based methods. (AQuA does not detect ROIs.) (a) Pure ROI. (b) Size change odds of 5, indicating size changes 20–500% of ROI. (c) Location change ratio of 1. Average distance to the center of the ROI is 100% the ROI diameter. (d) Mixed propagation with 10 frames.



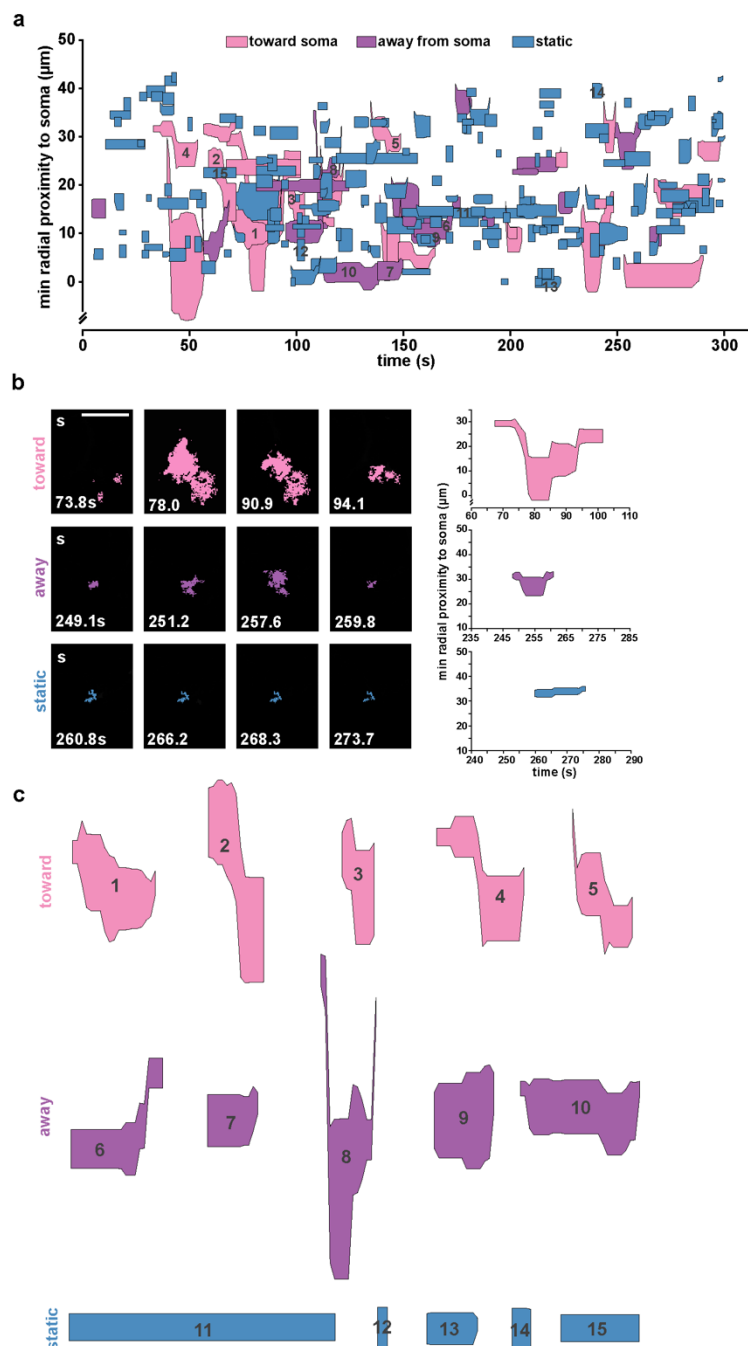
Extended Data Figure 2.5: Event counts under different SNRs.

Study the impact of SNR change when size change ratio is 3. The color shows the count of events on that pixel. All plots share the same scale. The red lines are the boundaries of detected ROIs. **(a)** Ground truth event count and the color bar for all plots. **(b)** The event count for all methods under four different SNRs.



Extended Data Figure 2.6: Peer method performance on growing and moving propagation types.

Schematic (top) and results (bottom) of performance of five image-analysis methods (AQUA, GECI-quant, CaSCaDe, CalmAn, and Suite2P) on simulated datasets with (a) growing propagation and (b) moving propagation. Change of the propagation frame number is shown in the bottom left panel, and varying SNR in the bottom right. When the number of propagation frames (not the event duration) is 0, the simulation is under pure ROI assumptions. IoU (intersection over union) measures the overlap between detected and ground-truth events. An IoU of 1 is the best performance achievable by any method, meaning that all detected events are ground-truth and all ground-truth events are detected. The bars on each curve indicate the 95% confidence interval calculated from 10 independent replications of simulation, where each simulation contains hundreds of events.



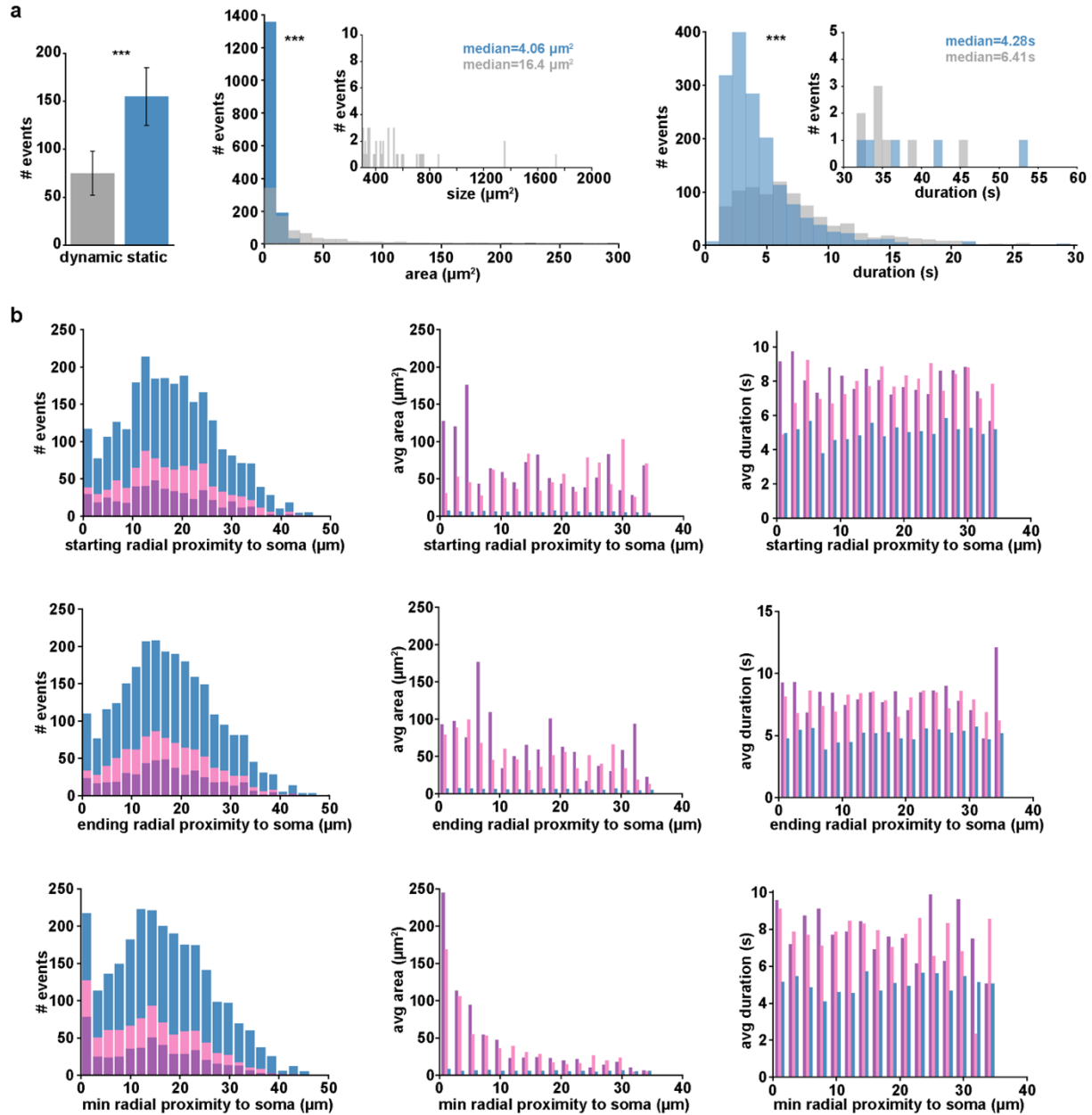
Extended Data Figure 2.7: AQUA features enable detailed Ca^{2+} activity plots.

(a) Spatiotemporal plot of Ca^{2+} activity from a five minute movie (the first minute of which is shown in Fig. 2.3b). Each event is represented by a polygon that is proportional to the area of the event as it changes over its lifetime, and color-coded by propagation direction. (b) Example time series illustrating how propagation direction is determined (left). A propagation direction score is calculated for each event by multiplying the Euclidian distance between the event pixels' proximity to the soma at each frame by each pixel's intensity. The overall score is the summation of this weighted pixel intensity distance over the lifetime of the event. Therefore, if more pixels with higher intensity move toward the soma it will be classified as such (top). While some events

Extended Data Figure 2.7 continued on next page

Extended Data Figure 2.7 continued

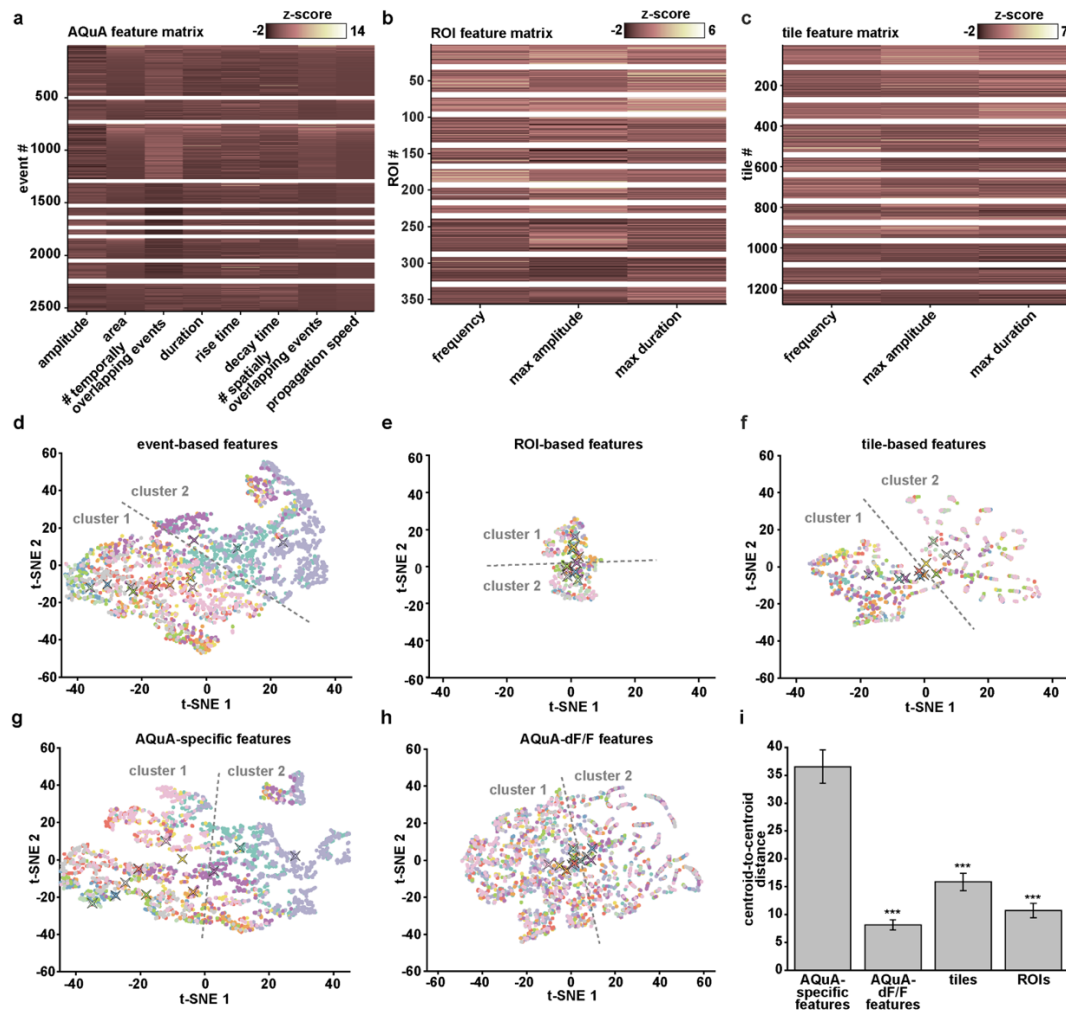
appear in the plot as moving toward the soma, they are actually calculated as moving away from the soma (middle) since we are only displaying the minimum event proximity to the soma in the spatiotemporal plot, but calculate each pixel's proximity to the soma when generating propagation score. Further, pixel intensity is first thresholded at 0.3dF/F. Therefore, events that move toward or away from the soma yet have pixel intensities below threshold (bottom) appear to have a propagation direction when plotted, yet have a zero propagation direction score when calculated. (c) Additional events plotted for each propagation direction category to demonstrate range of detected/plotted events. Scale is not equivalent to events shown in *b*, but is equivalent within entire group shown here.



Extended Data Figure 2.8: Distribution of Ca²⁺ event features.

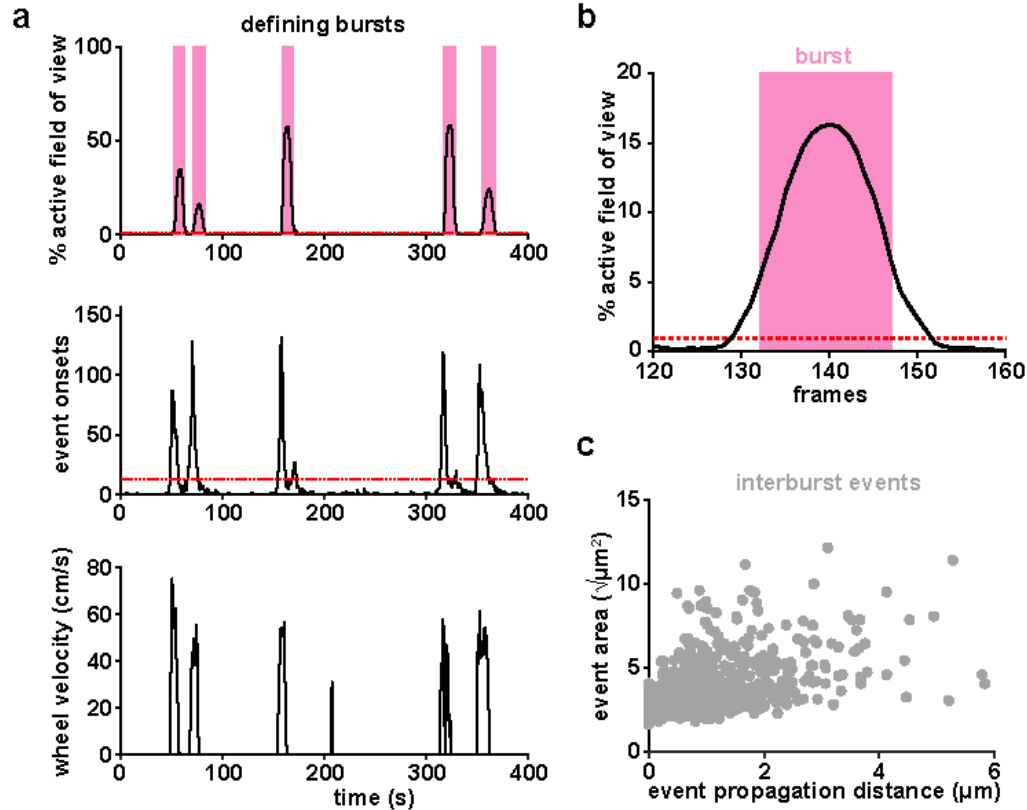
(a) Left: total number of Ca²⁺ events that are dynamic (gray, propagation direction score > 0) and static (blue, propagation direction score = 0) within the 2D imaging plane, ***p < 0.001, n=11 cells, chi-square test for independence. Middle: distribution of Ca²⁺ event area for dynamic and static events, ***p < 0.001, one-tailed Wilcoxon rank sum test. Right: distribution of Ca²⁺ event duration for dynamic and static events, ***p < 0.001, one-tailed Wilcoxon rank sum test (right).

(b) Distribution, average area, and average duration of events propagating toward soma (pink), away from soma (purple), and static events (blue) compared to starting distance from soma (top row), ending distance from soma (middle row), and minimum distance from soma (bottom row). Bin widths calculated by Freedman-Diaconis's rule.



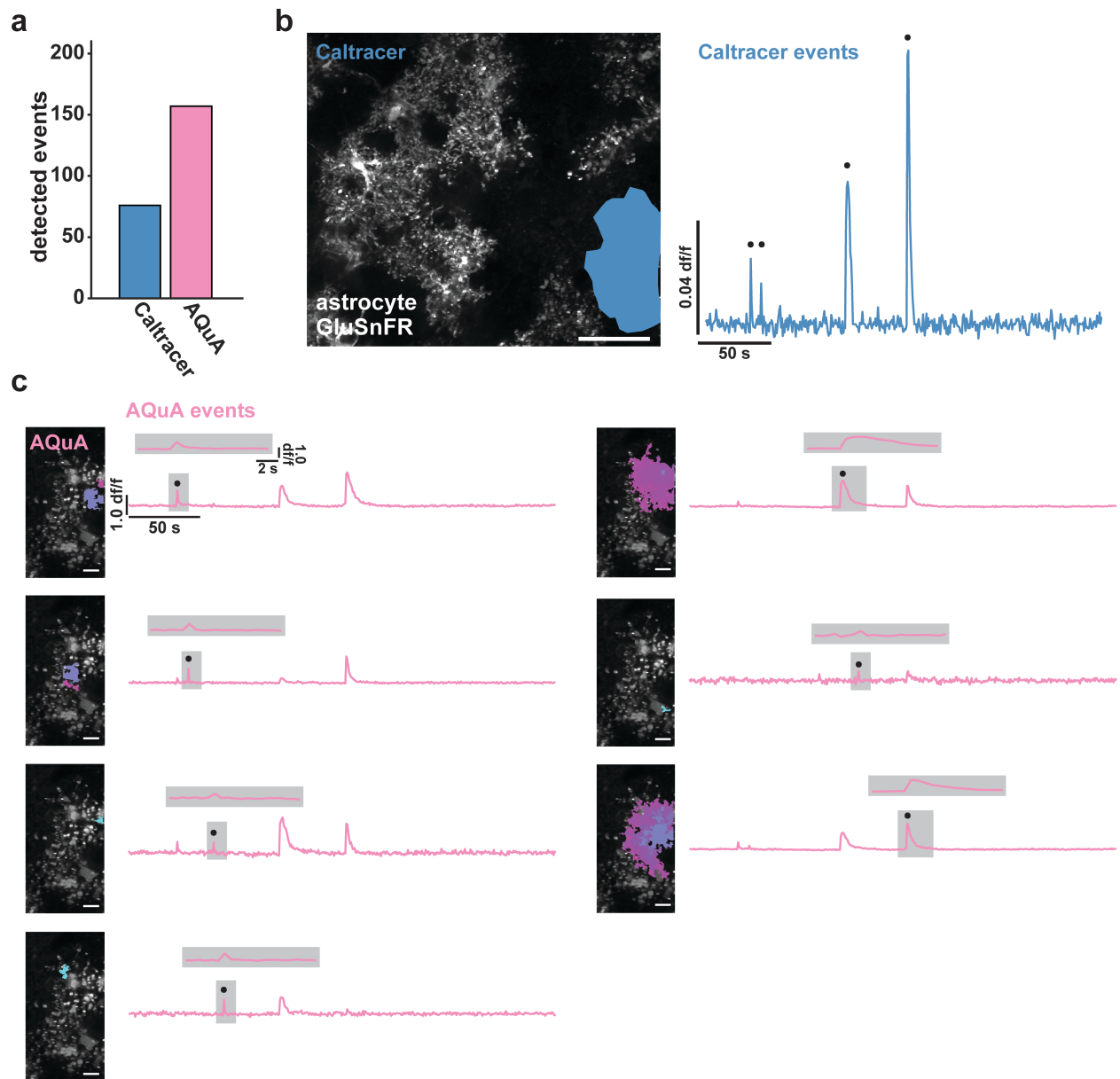
Extended Data Figure 2.9: Cluster analysis on features generated from three spatial footprint methods.

(a) Heatmap of z-scores for eight AQuA features (x-axis) describing each event. White boxes demarcate events and features from individual cells. (b–c) Top: heatmaps of z-scores for three features describing the Ca^{2+} activity at each ROI (b) or tile (c) location. ROIs detected using average projection image with a $5\mu\text{m}$ square filter applied (for ROIs) or $5\times 5\mu\text{m}$ tiles, based on fluorescence intensity and size. Ca^{2+} events with signals $> 0.03\text{dF/F}$ and two times the noise of each individual trace were selected. Pixels within each ROI or tile were averaged and dF/F was calculated by dividing each value by the mean values from the previous 25 seconds. (d–f) t-SNE visualizations of each cell's Ca^{2+} activity using features calculated using AQuA (d), ROIs (e), and tiles (f). High dimensional data (a–c) are reduced and displayed in two dimensions. Points that are clustered closer together can be interpreted as having more similar Ca^{2+} activity features. k-means clustering boundary denoted as dashed line. (g–h) t-SNE plots using only subsets of AQuA-calculated features from (a) and (d). (g) t-SNE plot of only the features specific to AQuA and not shared with ROI or tile analysis. (h) Plot using only AQuA-extracted features that correspond to those in ROI- or tile-based analyses. (i) Comparison of difference between two clusters generated from the t-SNE analysis followed by k-means clustering. Note increased separation using AQuA-specific features compared to others. (One-tailed paired t-test, *** $p < 0.001$)



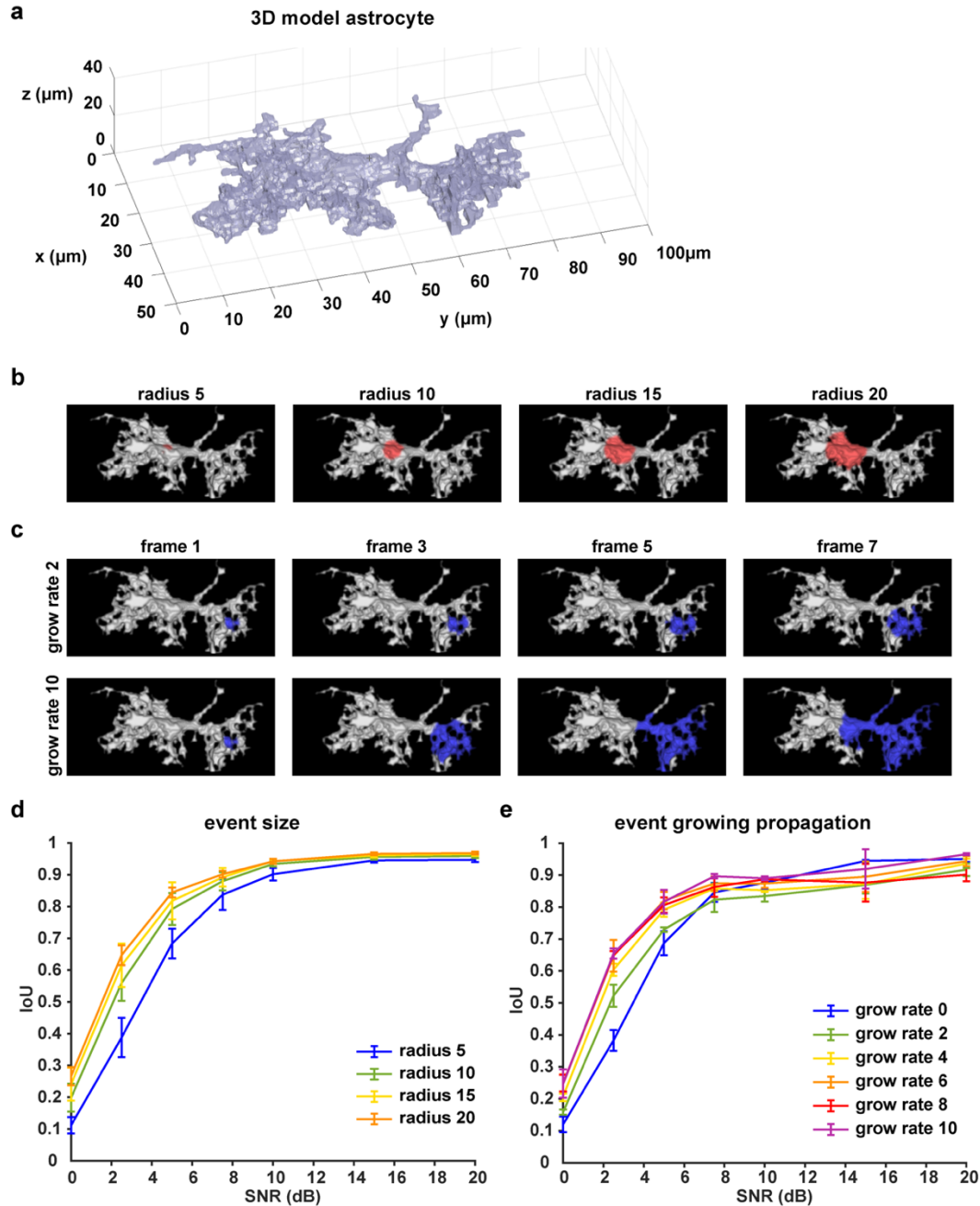
Extended Data Figure 2.10: Defining Ca²⁺ bursts.

(a) Population Ca²⁺ events represented as two temporal traces: percentage of imaging field active (top) and number of AQuA event onsets (middle). Burst periods (pink) are defined from the top trace as periods when Ca²⁺ activity exceeds 1% of the active field of view (red dashed line, top), and exceeds 10% of the maximum number of event onsets (red dashed line, middle). Burst periods correlate with wheel velocity of the treadmill (bottom). (b) Burst onset is defined as the first frame in which 10% of the peak is exceeded and burst offset is defined as the last frame exceeding 10% of the peak. (c) The relationship between all interburst events' total propagation distance and size, similar to the burst events plotted in Fig. 2.4c.



Extended Data Figure 2.11: Comparison of AQuA and Caltracer for event detection of astrocytic GluSnFR signals.

(a) Applied to the same data sets, AQuA detects 157 events, while Caltracer^{2,9}, using a rising faces algorithm, detects 76 events with manually defined single-cell ROIs. (b) ROI example (left) and temporal trace with detected events marked by black circle using Caltracer software. Scale bar = 50 μ m. (c) AQuA-detected events from the same cell as in (b), and corresponding temporal traces (black dot, specific events shown above each trace). Scale bar = 10 μ m.



Extended Data Figure 2.12: AQUA performance on simulated 3D datasets.

(a) The 3D model used for performance testing the 3D AQUA extension was extracted from real imaging data¹⁷. (b) Example of simulated data in which event size varies; each column represents a different event radius. (c) Examples of simulated events with slow (top row, growth rate 2) and fast (bottom row, growth rate 10) growing propagation rates. (d–e) Results of AQUA performance on simulated datasets with respect to varying SNR under independently varying event (d) size and (e) growing propagation rates. IoU (intersection over union) measures the overlap between detected and ground-truth events. An IoU of 1 is the best performance achievable, indicating that all detected events are ground-truth and all ground-truth events are detected. The bars on each curve indicate the 95% confidence interval calculated from 5 independent replications of simulation, where each simulation contains 10–20 events.

References

1. Srinivasan, R. *et al.* New Transgenic Mouse Lines for Selectively Targeting Astrocytes and Studying Calcium Signals in Astrocyte Processes In Situ and In Vivo. *Neuron* **92**, 1181–1195 (2016).
2. Marvin, J. S. *et al.* An optimized fluorescent probe for visualizing glutamate neurotransmission. *Nat. Methods* **10**, 162–170 (2013).
3. Chen, T.-W. *et al.* Ultrasensitive fluorescent proteins for imaging neuronal activity. *Nature* **499**, 295–300 (2013).
4. Srinivasan, R. *et al.* Ca²⁺ signaling in astrocytes from Ip3r2(-/-) mice in brain slices and during startle responses in vivo. *Nat. Neurosci.* **18**, 708–717 (2015).
5. Paukert, M. *et al.* Norepinephrine controls astroglial responsiveness to local circuit activity. *Neuron* **82**, 1263–1270 (2014).
6. Hausteiner, M. D. *et al.* Conditions and constraints for astrocyte calcium signaling in the hippocampal mossy fiber pathway. *Neuron* **82**, 413–429 (2014).
7. Ding, F. *et al.* α 1-Adrenergic receptors mediate coordinated Ca²⁺ signaling of cortical astrocytes in awake, behaving mice. *Cell Calcium* **54**, 387–394 (2013).
8. Poskanzer, K. E. & Yuste, R. Astrocytes regulate cortical state switching in vivo. *Proc. Natl. Acad. Sci. U.S.A.* 201520759 (2016). doi:10.1073/pnas.1520759113
9. Ma, Z., Stork, T., Bergles, D. E. & Freeman, M. R. Neuromodulators signal through astrocytes to alter neural circuit activity and behaviour. *Nature* **539**, 428–432 (2016).
10. Poskanzer, K. E. & Yuste, R. Astrocytic regulation of cortical UP states. *Proc. Natl. Acad. Sci. U.S.A.* **108**, 18453–18458 (2011).
11. Looger, L. L. A genetically encoded fluorescent sensor for in vivo imaging of GABA.

- bioRxiv* 322578 (2018). doi:10.1101/322578
12. Feng, J. *et al.* A Genetically Encoded Fluorescent Sensor for Rapid and Specific In Vivo Detection of Norepinephrine. *Neuron* (2019). doi:10.1016/j.neuron.2019.02.037
 13. Lobas, M. A. *et al.* A genetically encoded single-wavelength sensor for imaging cytosolic and cell surface ATP. *Nature Communications* **10**, 711 (2019).
 14. Patriarchi, T. *et al.* Ultrafast neuronal imaging of dopamine dynamics with designed genetically encoded sensors. *Science* **360**, eaat4422 (2018).
 15. Agarwal, A. *et al.* Transient Opening of the Mitochondrial Permeability Transition Pore Induces Microdomain Calcium Transients in Astrocyte Processes. *Neuron* **93**, 587–605.e7 (2017).
 16. Armbruster, M., Hanson, E. & Dulla, C. G. Glutamate Clearance Is Locally Modulated by Presynaptic Neuronal Activity in the Cerebral Cortex. *J. Neurosci.* **36**, 10404–10415 (2016).
 17. Bindocci, E. *et al.* Three-dimensional Ca(2+) imaging advances understanding of astrocyte biology. *Science* **356**, eaai8185 (2017).
 18. Wu, Y.-W. *et al.* Spatiotemporal calcium dynamics in single astrocytes and its modulation by neuronal activity. *Cell Calcium* **55**, 119–129 (2014).
 19. Wang, Y. *et al.* Graphical Time Warping for Joint Alignment of Multiple Curves. *Neural Information Processing Systems* 3648–3656 (2016).
 20. Giovannucci, A. *et al.* CaImAn: An open source tool for scalable Calcium Imaging data Analysis. *bioRxiv* 339564 (2018). doi:10.1101/339564
 21. Pachitariu, M. *et al.* Suite2p: beyond 10,000 neurons with standard two-photon microscopy. (2016). doi:10.1101/061507

22. Poskanzer, K. E. & Molofsky, A. V. Dynamism of an Astrocyte In Vivo: Perspectives on Identity and Function. *Annu. Rev. Physiol.* **80**, 143–157 (2018).
23. Shigetomi, E. *et al.* Imaging calcium microdomains within entire astrocyte territories and endfeet with GCaMPs expressed using adeno-associated viruses. *J. Gen. Physiol.* **141**, 633–647 (2013).
24. van der Maaten, L. & Hinton, G. Visualizing Data using t-SNE. *Journal of Machine Learning Research* **9**, 2579–2605 (2008).
25. Stobart, J. L. *et al.* Cortical Circuit Activity Evokes Rapid Astrocyte Calcium Signals on a Similar Timescale to Neurons. *Neuron* **98**, 726–735.e4 (2018).
26. Kanemaru, K. *et al.* In vivo visualization of subtle, transient, and local activity of astrocytes using an ultrasensitive Ca(2+) indicator. *Cell Rep* **8**, 311–318 (2014).
27. Nimmerjahn, A., Mukamel, E. A. & Schnitzer, M. J. Motor behavior activates Bergmann glial networks. *Neuron* **62**, 400–412 (2009).
28. Parsons, M. P. *et al.* Real-time imaging of glutamate clearance reveals normal striatal uptake in Huntington disease mouse models. *Nature Communications* **7**, 11251 (2016).
29. Jiang, R., Diaz-Castro, B., Looger, L. L. & Khakh, B. S. Dysfunctional Calcium and Glutamate Signaling in Striatal Astrocytes from Huntington's Disease Model Mice. *J. Neurosci.* **36**, 3453–3470 (2016).
30. Hefendehl, J. K. *et al.* Mapping synaptic glutamate transporter dysfunction in vivo to regions surrounding A β plaques by iGluSnFR two-photon imaging. *Nature Communications* **7**, 13441 (2016).
31. Marvin, J. S. *et al.* Stability, affinity, and chromatic variants of the glutamate sensor iGluSnFR. *Nat. Methods* **15**, 936–939 (2018).

32. Fino, E. *et al.* RuBi-Glutamate: Two-Photon and Visible-Light Photoactivation of Neurons and Dendritic spines. *Front Neural Circuits* **3**, 2 (2009).
33. Chai, H. *et al.* Neural Circuit-Specialized Astrocytes: Transcriptomic, Proteomic, Morphological, and Functional Evidence. *Neuron* **95**, 531–549.e9 (2017).
34. Baraban, M., Koudelka, S. & Lyons, D. A. Ca²⁺ activity signatures of myelin sheath formation and growth in vivo. *Nat. Neurosci.* **19**, 190 (2017).
35. Krasnow, A. M., Ford, M. C., Valdivia, L. E., Wilson, S. W. & Attwell, D. Regulation of developing myelin sheath elongation by oligodendrocyte calcium transients in vivo. *Nat. Neurosci.* **93**, 9887 (2017).
36. Higley, M. J. & Sabatini, B. L. Calcium signaling in dendritic spines. *Cold Spring Harb Perspect Biol* **4**, a005686–a005686 (2012).
37. Keller, P. J. & Ahrens, M. B. Visualizing whole-brain activity and development at the single-cell level using light-sheet microscopy. *Neuron* **85**, 462–483 (2015).
38. Goldey, G. J. *et al.* Removable cranial windows for long-term imaging in awake mice. *Nat Protoc* **9**, 2515–2538 (2014).

Chapter 3:

Network-level encoding of local neurotransmitters in cortical astrocytes

Abstract

Astrocytes—the most abundant non-neuronal cell type in the mammalian brain—are crucial circuit components that respond to and modulate neuronal activity via calcium (Ca^{2+}) signaling. Astrocyte Ca^{2+} activity is highly heterogeneous and occurs across multiple spatiotemporal scales: from fast, subcellular activity to slow, synchronized activity that travels across connected astrocyte networks. Furthermore, astrocyte network activity has been shown to influence a wide range of processes. While astrocyte network activity has important implications for neuronal circuit function, the inputs that drive astrocyte network dynamics remain unclear. Here we used *ex vivo* and *in vivo* two-photon Ca^{2+} imaging of astrocytes while mimicking neuronal neurotransmitter inputs at multiple spatiotemporal scales. We find that brief, subcellular inputs of GABA and glutamate lead to widespread, long-lasting astrocyte Ca^{2+} responses beyond an individual stimulated cell. Further, we find that a key subset of Ca^{2+} activity—propagative events—differentiates astrocyte network responses to these two major neurotransmitters, and gates responses to future inputs. Together, our results demonstrate that local, transient neurotransmitter inputs are encoded by broad cortical astrocyte networks over the course of minutes, contributing to accumulating evidence across multiple model organisms that significant astrocyte-neuron communication occurs across slow, network-level spatiotemporal scales. We anticipate that this study will be a starting point for future studies investigating the link between specific astrocyte Ca^{2+} activity and specific astrocyte functional outputs, which could build a consistent framework for astrocytic modulation of neuronal activity.

Introduction

A set of defined rules governing neuronal input-output relationships is a cornerstone of neuroscience. Given a specific excitatory or inhibitory neurotransmitter (NT) input, post-synaptic membrane potential changes that lead to action potentials can be accurately predicted. But, neurons are not the only cells in the nervous system that sense NTs. Astrocytes—the most abundant non-neuronal cell type in the mammalian brain—are crucial circuit components that respond to and modulate neuronal activity via calcium (Ca^{2+}) signaling¹⁻⁸. However, the set of rules governing input-output relationships in astrocytes is poorly defined, in part because it's unclear over which spatiotemporal scales these relationships should be evaluated. While there appear to be fast and local astrocytic responses to local stimuli^{3,4}, there is also evidence to suggest that astrocyte responses to local stimuli have a spatiotemporally distributed component, as local astrocyte stimulation can lead to distributed changes in neuronal activity and plasticity^{9,10}. Thus, a comprehensive framework describing input-output relationships in astrocytes requires simultaneous investigation of activity across multiple spatiotemporal scales.

Here, we set out to build an input framework governing transient and sustained cortical astrocyte Ca^{2+} activity at three spatial scales: subcellular, single cell, and network. To take a physiologically relevant and comparative approach, we focused on astrocyte responses to the two major NTs: glutamate and GABA. While previous studies demonstrate general astrocyte Ca^{2+} increases in response to these NTs^{2,6,11,12}, our goal was to link specific excitatory and inhibitory chemical inputs to specific astrocyte Ca^{2+} activity, and map the scales over which astrocytes could exert effects on neuronal circuitry.

Results

NTs drive distinct astrocyte Ca²⁺ activity

To first test whether astrocytes show generally distinct activity in response to different NTs, we used two-photon (2P) Ca²⁺ imaging (via the genetically encoded intracellular indicator, Cyto-GCaMP6f) of astrocytes while sequentially bath-applying GABA and glutamate receptor agonists onto *ex vivo* acute cortical slices from mice (Fig. 3.1a). We activated the GABAergic and glutamatergic GPCRs expressed by astrocytes^{13,14} (Extended Data Fig. 3.1a), using baclofen to activate GABA_B receptors^{2,11,15} and a broad spectrum metabotropic glutamate receptor (mGluR) agonist, (1S-3R)-ACPD (t-ACPD)^{9,16-18}, to activate mGluR₃, the mGluR subtype expressed by astrocytes at this age¹⁹, while silencing neuronal firing with tetrodotoxin (TTX). We analyzed the resulting Ca²⁺ activity using the event-detection software AQUA²⁰ (Fig. 3.1b). In the same populations of astrocytes, with similar levels of baseline activity (Extended Data Fig. 3.1b), GABA_BR or mGluR₃ activation both increased Ca²⁺ event frequency, but each led to distinct Ca²⁺ responses in time-course and magnitude. Using both event-based and region-of-interest (ROI)-based analysis methods, we found with t-ACPD, Ca²⁺ activity increases were robust and transient, whereas baclofen caused a delayed and prolonged activation, lasting through the end of recording (Fig. 3.1c, Extended Data Fig. 3.1c–e, Extended Data Table 3.1, 3.3). Analyzing individual Ca²⁺ events by area and duration, we found a population of events larger and longer compared to baseline with t-ACPD, but not with baclofen (Fig. 3.1d, Extended Data Fig. 3.1f,g, Extended Data Table 3.4). To ensure that these distinct responses weren't dependent on a specific agonist concentration or agonist order, we quantified activity changes across a broad concentration range, alternating agonist order between concentrations. Across Ca²⁺ event features, we saw a consistently higher response with mGluR₃ compared to GABA_BR

activation (Fig. 3.1e–h, Extended Data Table 3.2), demonstrating that the same cortical astrocyte populations exhibit distinct activity, with distinct time courses, in response to different NTs.

GABA_BR and mGluR₃ are both G_i-coupled GPCRs canonically linked to decreases in intracellular cAMP. To explore whether these two G_i-GPCRs also engage cAMP in NT-specific ways, we expressed the genetically encoded cAMP sensor Pink Flamindo²¹ in astrocytes, and bath-applied agonists selective for these receptors (Extended Data Fig. 3.1h–k). We switched from using a broad spectrum mGluR agonist, t-ACPD (Fig. 3.1), to an mGluR₃-selective agonist, LY 379268 (Extended Data Fig. 3.1h–k), to specifically examine the effect of this G_i-GPCR activation on cAMP activity. In contrast to canonical G_i-GPCR signaling, we saw slow and sustained cAMP increases^{22,23} with both agonists, with more cells responding to mGluR₃ compared to GABA_BR activation (Extended Data Fig. 3.1j). When comparing astrocytic Ca²⁺ and cAMP signaling in response to agonists, we found significantly more dynamic Ca²⁺ activity compared to cAMP (Extended Data Fig. 3.1k). Although Ca²⁺ isn't a canonical downstream signaling partner of G_i-GPCRs, our results confirm previous findings that astrocytes do signal via mGluR₃ and GABA_BR to mobilize intracellular Ca²⁺ (ref. ^{2,11,22,24}) potentially via PLC signaling^{25,26} or by βγ subunits directly binding to IP₃R^{27,28}. The relative lack of dynamism in cAMP compared to Ca²⁺ led us to focus only on Ca²⁺ as the second messenger more likely to exhibit NT-specific responses to spatiotemporally restricted—and more physiological—NT release.

Single astrocytes respond to subcellular release of NTs

To release NTs with spatiotemporal precision, we used 2P photo-release (“uncaging”) of caged neurotransmitters (Fig. 3.2a), as is commonly used to interrogate post-synaptic physiology

via restricted activation area and duration^{7,9,29–33}. To compare the effects of GABA or glutamate on the same astrocytes, we chose a class of caged compounds (with ruthenium bipyridine [RuBi] backbones), bound to either GABA^{34,35} or glutamate^{35,36}, that can be 2P-uncaged (800nm) during simultaneous GCaMP Ca²⁺ imaging with a second 2P laser (excitation 980nm) (Fig. 3.2b). With this strategy, the uncaging/imaging experimental paradigm is common to both GABA and glutamate conditions. Because of likely variability in the Ca²⁺ response to NT across individual cells^{7,37}, we imaged the same astrocytes while sequentially uncaging GABA and glutamate at the same subcellular location, separated by an inter-imaging interval of > 20 min, including a washout period of > 10 min. To account for any changes resulting from prior NT release, we alternated the order of GABA- or glutamate-uncaging between slices. To first quantify the properties of NT release in this dual-2P uncaging/imaging strategy, we imaged an extracellular-facing glutamate sensor (GluSnFR³⁸) while uncaging RuBi-glutamate (Fig. 3.2c). We confirmed that NT release was spatiotemporally confined at the intended location over an area of ~25 μm² and duration of 0.5–1 s (Fig. 3.2d). To ensure that the uncaging laser itself does not stimulate astrocytes, we also stimulated GCaMP-expressing astrocytes with the uncaging laser alone in the absence of RuBis, and did not observe a change in average Ca²⁺ fluorescence or event frequency (Extended Data Fig. 3.2a,b, Extended Data Table 3.5).

After validating the spatiotemporal precision of this approach, we next released NT during GCaMP imaging. We first analyzed the Ca²⁺ activity within the astrocyte that was directly stimulated (Fig. 3.2e). We observed examples of Ca²⁺ increases within seconds, in close proximity to the uncaging site (Fig. 3.2f, g). By plotting $\Delta F/F$ and sorting by latency-to-fluorescence increases, we saw most astrocytes increase Ca²⁺ activity following NT release (Fig. 3.2h, above white line [70% and 88% of cells for GABA and glutamate, respectively], 3.2i), but

the area and duration of Ca^{2+} events were unchanged (Extended Data Fig. 3.2e). The activity increases often lasted for 2.5 minutes after NT release, the post-uncaging duration of the recording (Fig. 3.2h, Extended Data Fig. 3.2b), validating previous findings that NT-induced astrocyte Ca^{2+} activity can be long-lasting^{2,6}. Comparing the same astrocyte's response to both NTs, we found no significant relationship between the magnitude of its response to GABA vs. glutamate (Fig. 3.2j), a controlled comparison given similar levels of activity within each cell prior to uncaging (Extended Data Fig. 3.2c,d). To confirm that the Ca^{2+} elevations were due to activation of astrocytic GPCRs, we next performed NT uncaging in slices where $\text{GABA}_{\text{B}}\text{R}$ or mGluR were inhibited pharmacologically, and found that Ca^{2+} increases were indeed blocked in these conditions (Extended Data Fig. 3.2a,b).

Astrocyte Ca^{2+} activity can be highly compartmentalized^{3,4,7,37}, so we next tested whether observed changes in Ca^{2+} activity within the stimulated astrocyte were confined to subcellular regions directly exposed to initial NT release ($<10\mu\text{m}$ from uncaging, Fig. 3.2c,d). We found an increased frequency of Ca^{2+} events both near ($<10\mu\text{m}$) and far ($\geq 10\mu\text{m}$) from the uncaging site (Fig. 3.2k–o and Extended Data Fig. 3.2f), with increases in both spatial domains peaking ≥ 1 min after uncaging for both NTs. These data demonstrate that spatiotemporally restricted NT release can drive Ca^{2+} activity in subcellular compartments extending beyond the stimulated region.

Astrocyte networks respond to subcellular NTs

To ask whether activity changes extended beyond single cells, we next investigated population-wide Ca^{2+} activity in neighboring astrocytes within the gap junctionally coupled local network (Fig. 3.3a). Within the $300 \times 300 \mu\text{m}$ imaging field-of-view (FOV), the astrocyte over

which NT was uncaged was approximately centered. Neighboring astrocytes ($n=10.3\pm 3.85$, mean \pm SD) with GCaMP6f activity were imaged and distinguished from the uncaged cell by delineating cell maps. The active neighboring astrocytes within a given FOV define a “local network” (Fig. 3.3a,b). We observed general Ca^{2+} increases within the local network of astrocytes after uncaging (Fig. 3.3b, Extended Data Fig. 3.3d–f). While we saw heterogeneity in the timing and magnitude of local network responses to subcellular NT release in the uncaged cell, the majority of imaged networks responded with population-wide fluorescence increases (Fig. 3.3c, left).

To investigate whether gap junctional coupling mediates these non-cell autonomous Ca^{2+} activity changes after a single point of network stimulation, we either genetically or pharmacologically inhibited gap junctions and measured population-wide network Ca^{2+} responses (Fig. 3.3c–f). Genetically, we focused on the predominant connexin protein (Cx43) expressed in cortical astrocytes^{13,14,39} (Extended Data Fig. 3.3a), and decreased Cx43 expression by injecting the astrocyte-specific Cre virus *AAV5-GFAP(0.7)-RFP-T2A-iCre*⁴⁰ (and *AAV5-GfaABC1D-GCaMP6f-SV40* to express GCaMP) into Cx43^{fl/+} and Cx43^{fl/fl} mice. Cx43 protein decreases in Cre⁺ cells were confirmed via immunohistochemistry (Extended Data Fig. 3.3b,c). After targeting Cre⁺ astrocytes for RuBi-GABA and -glutamate uncaging, population-wide network activity changes were attenuated compared to those observed in wild-type (WT) slices (Fig. 3.3c, right). While population-wide fluorescence did rise above threshold in some post-stim frames in Cx43^{floxed} and CBX networks with similar onset latencies to WT networks (Fig. 3.3d, e), the proportion of time population-wide activity remained in an elevated state was significantly reduced in networks with gap junctional inhibition (Fig. 3.3c, f). Additionally, Cx43^{floxed} networks showed no significant increase in average event frequency, similar to the

laser-uncaging controls and receptor-activation controls in slices where GABA_BR or mGluR were inhibited pharmacologically during uncaging (Extended Data Fig. 3.3g,h, Extended Data Table 3.7). These results suggest that astrocytic Cx43-based signaling is necessary for the sustained increase in network-level Ca²⁺ activity following NT release elsewhere in the local network. Further, these observations hint that reduced Ca²⁺ signaling in uncoupled astrocyte networks may underlie altered neuronal network activity and deficits in sensory-related behaviors observed in Connexin-deficient mice^{41,42}.

We next asked how far NT-induced local network activity extended from the uncaged cell. First, using a Sholl-like analysis (Fig. 3.3g), we observed event frequency increases as far away as 125–175µm from uncaging of both GABA and glutamate (Fig. 3.3h, Extended Data Table 3.6), which extends to the edge of the FOV (Extended Data Fig. 3.3i). To compare the spatial distribution of these network-level responses between GABA and glutamate, we then analyzed event activity within 20x20µm ROIs in a grid over the FOV (Fig. 3.3i–k). As in the Sholl-like analysis (Fig. 3.3h), ROIs with uncaging-driven activity were distributed both near and far from the uncaging site (GABA: 119.9±46.1µm; glutamate: 109.3±49.4µm [mean±SD]) (Fig. 3.3j). Further, while baseline activity encompasses contiguous, overlapping portions of the astrocyte network (Fig. 3.3k, left), ROIs exhibiting an event increase after NT uncaging were sparse (Extended Data Fig. 3.3j) and, critically, exhibit no significant overlap between responses to GABA and glutamate (Fig. 3.3k, right and l), suggesting that GABA and glutamate do not primarily activate the same regions of the astrocyte network. Together these data show that focal release of NT at a single cortical astrocyte leads to spatially distributed changes in Ca²⁺ activity across an astrocyte network.

Propagation distinguishes network responses

Because astrocyte events are highly heterogeneous²⁰, we next performed an unbiased analysis screen for changes in 16 AQuA-extracted event characteristics from neighboring cells (Extended Data Fig. 3.4a,b, Extended Data Table 3.12–3.13). The most robust and consistent NT-specific changes in neighboring cells were in events exhibiting propagation, with specific directionality toward the pia (Fig. 3.4a,b, Extended Data Fig. 3.4b, Extended Data Table 3.8, 3.13), which echoed a change we observed above in populations of astrocytes following more widespread NT exposure (Fig. 3.1h). These propagative events were discrete events contained within individual cells (Fig. 3.4a) and we did not observe coordinated activity propagating across populations of astrocytes with a visible wavefront (Extended Data Fig. 3.5a). Since propagative events constituted a small subset of spontaneous *ex vivo* astrocyte Ca²⁺ activity (Extended Data Fig. 3.5b), we wanted to ensure that they reflected activity that could be observed *in vivo*. To test this, we recorded spontaneous astrocyte Ca²⁺ activity from the same cortical region (V1) in head-fixed mice^{5,20} (Fig. 3.4c). We focused on spontaneous astrocyte Ca²⁺ activity that occurred when the mouse was stationary, to eliminate stimulus-triggered Ca²⁺ bursts driven by locomotion^{20,43–45}. We found a similar fraction of propagative events *ex vivo* and *in vivo* (Fig. 3.4d), suggesting that this small subset of Ca²⁺ activity may indeed comprise a physiologically relevant population.

Ex vivo, propagative event frequency specifically increases after glutamate uncaging, in all 30-s time-bins 0–120s post-uncaging across neighboring cells (Fig. 3.4e, f, Extended Data Fig. 3.5c, Extended Data Table 3.9–3.10), while no changes were observed across neighboring cells after GABA uncaging in these same slices. Indeed, local network responses to glutamate and GABA uncaging can also be distinguished via the fraction of cells exhibiting changes in propagative event frequency (Fig. 3.4g), in which a higher fraction of astrocytes in each local

network respond with increases in propagative activity to glutamate (~40%) compared to GABA (~25%) (Fig. 3.4h, Extended Data Fig. 3.5d, Extended Data Table 3.9). Further, the NT input received can be accurately decoded via the relative change in propagative event rate/FOV (Fig. 3.4i). In contrast, a similar fraction of local network astrocytes responds to GABA and glutamate with increased static event frequency (Extended Data Fig. 3.6, Extended Data Table 3.9–3.10). Astrocytes in the local network exhibited significantly higher baseline propagative activity and similar levels of static activity prior to uncaging GABA compared to glutamate (Extended Data Fig. 3.5g). While this could influence results, these baseline differences likely do not account for the differential network responses to the two NTs because baseline propagative rate is not correlated with the relative post-uncaging propagative event rate (Extended Data Fig. 3.5h). These results indicate that glutamate and GABA are differentially encoded at the network level by engaging local network astrocytes to differing degrees via Ca^{2+} events that propagate within individual cells (Fig. 3.4n). Because there are few propagative events at baseline, even a small increase in propagative events following uncaging is a large relative increase in activity, and may thus constitute a salient signal with a high signal-to-noise ratio. This increase in glutamate-driven propagative responses is not observed when uncaging NTs in astrocyte networks with decreased Cx43 expression (Fig. 3.4j,k, Extended Data Table 3.9–3.10), which show significantly lower baseline activity compared to WT networks (Extended Data Fig. 3.5f). These data suggest that gap junction coupling is a cellular mechanism underlying this NT-specific signal.

Similar to our prior finding that all network-level responses to glutamate and GABA were spatially non-overlapping (Fig. 3.3k,l), out of astrocytes that responded to either NT, we see few astrocytes responsive via propagative activity increases to *both* NTs (Fig. 3.4l). In fact, the number of astrocytes responsive to both NTs is not significantly different from chance,

indicating that how an astrocyte in the network responds to one NT provides no information about how that same astrocyte will respond to the other NT. Further, when uncaging less glutamate in a different set of local networks (Extended Data Fig. 3.7a, b), the response profile of an individual astrocyte to three sequential rounds of NT release at the same location was variable (Extended Data Fig. 3.7c). This was a controlled comparison since average increases in event frequency occurred over a similar time course (Extended Data Fig. 3.7d, Extended Data Table 3.14) and baseline activity was comparable in astrocytes of the local network across rounds (Extended Data Fig. 3.7e). Since propagative response to a particular NT does not predict the response to the other NT nor to sequential stimulation by the same NT, we next looked for metrics that instead might predict astrocyte-network responses. Astrocyte Ca^{2+} activity can depend on prior and current Ca^{2+} levels^{44,46,47}, which led us to ask whether network-level propagative responses could be predicted based on ongoing network activity. To do so, we asked whether the composition of baseline (1 min) activity in the network could predict the network-level response to uncaging (Extended Data Fig. 3.5e). Here, we saw that those cells with a higher fraction of propagative events at baseline (relative to all baseline events) were correlated with a lower fraction of astrocytes in each network responding to either GABA or glutamate (Fig. 3.4m, left, Extended Data Fig. 3.5i, j, Extended Data Table 3.11). In contrast, overall baseline event rate was not predictive of responses to either NT (Fig. 3.4m, right). Thus, in addition to differentiating the local astrocyte network response to GABA or glutamate, these data suggest that propagative events can selectively bias the astrocyte network's subsequent responses to NTs.

Discussion

Single astrocyte stimulation can cause long-lasting changes in neuronal activity and plasticity extending tens to hundreds of microns from the stimulation site^{9,10,41}. However, the mechanism(s) that drive distributed effects have been unclear. Here, a brief, spatially restricted NT input leads to long-lasting, network-wide changes in astrocyte Ca^{2+} , an effect facilitated by gap junctions. These findings could bridge the spatiotemporal gap between transient, local astrocyte stimulation and sustained, distributed effects on neurons. Still, the full spatial extent of astrocyte network activation remains an open question because astrocyte Ca^{2+} changes extend beyond our FOV.

What might be an effect of restricted NT inputs causing prolonged and distributed responses? For coordinated behavior and learning, neuronal signals are integrated over seconds and minutes⁴⁸. Models of neural integration that solely rely on neuronal activity require fine-tuned positive feedback loops to allow for integration over periods longer than tens of milliseconds⁴⁹. While recurrent neuronal connections enable temporal integration, astrocyte networks provide another possible mechanism to integrate inputs over long time periods⁵⁰⁻⁵², linking the milliseconds timescale of neurons and the seconds-to-minutes timescales of behavior.

Both GABA and glutamate uncaging led to sustained, far-reaching changes in astrocyte network Ca^{2+} activity, but propagative activity differentiated responses to each NT (Fig. 3.4n). These propagative events may facilitate integration of information across cellular compartments which could allow for coordinated modulation of groups of nearby synapses⁵³ or spatiotemporal integration of inputs across individual cells⁴⁷. Stimulation by glutamate consistently led to greater increases in propagative activity (Fig. 3.1h and Fig. 3.4b, f and h), suggesting that cortical astrocytes are more responsive to glutamatergic than GABAergic signaling, as has been

described for other brain regions¹¹. Heightened astrocyte sensitivity to glutamate may mirror structural organization in the cortex, where astrocyte processes are closer to glutamatergic than GABAergic synapses⁵⁴, potentially reflecting astrocytes' key role in extracellular glutamate uptake. Since the surface mobility of astrocytic glutamate transporters is dependent on intracellular Ca^{2+} (ref. ⁵⁵), a more robust Ca^{2+} response to glutamate may allow astrocytes to efficiently take up extracellular glutamate by increasing surface mobility of glutamate transporters.

Astrocyte network responses to glutamate and GABA were also context-dependent: responses to both NTs were inhibited specifically by high fractions of propagative events at baseline (Fig. 3.4m). Thus, as glutamatergic input preferentially recruits propagative events in the surrounding astrocyte network (Fig. 3.4b,f,h), it could also suppress subsequent responses to NT inputs. This suggests that astrocyte networks implement combinatorial logic, integrating NT inputs across the local network by disseminating information via specific subtypes of Ca^{2+} activity.

While most astrocytes and local networks increase Ca^{2+} in response to NT uncaging, a subset don't respond to direct or remote uncaging. This heterogeneity may be shaped by the activity state of the astrocyte and connected network during stimulation or by the subcellular location of uncaging. Alternately, only a subset of astrocytes may be equipped to respond to NTs, given the molecular heterogeneity of astrocytes^{56,57}. Future experiments imaging astrocyte responses to NTs, followed by spatial transcriptomics, could elucidate how cellular machinery may underlie heterogeneous responses.

Here, astrocytic gap junctions mediate network activity changes, and may also regulate Ca^{2+} activity in individual cells. Molecules, including Ca^{2+} and IP_3 , can diffuse through gap

junctions^{58,59}. IP₃ is required for Ca²⁺ release from internal stores⁶⁰ and Ca²⁺ itself regulates Ca²⁺ release from internal stores via calcium-induced calcium release. Here, reduced gap junctional coupling between astrocytes may have altered cytosolic Ca²⁺ and IP₃ concentrations, which could impact Ca²⁺ release from internal stores and shape Ca²⁺ dynamics within individual cells.

Methods

Animals

Experiments were carried out using young adult mice, in accordance with protocols approved by the University of California, San Francisco Institutional Animal Care and Use Committee (IACUC). Animals were housed in a 12:12 light-dark cycle with food and water provided *ad libitum*. Male and female mice were used whenever available. Transgenic mice used in this study were Cx43^{fl/fl} mice⁶¹ from the Bhattacharya Lab (UCSF, USA) and EAAT2-tdT mice⁶² from the Yang Lab (Tufts University, USA). For *in vivo* imaging, all experiments were performed at the same time each day.

Surgical procedures

For viral expression for *ex vivo* experiments, neonatal Swiss Webster or C57Bl/6 (P0–3) mice were anesthetized on ice for 3 min before injecting viral vectors (*AAV5.GfaABC1D.GCaMP6f.SV40* [Addgene, 52925-AAV5], *AAV9.hGfap.pinkFlamindo*, *pENN.AAV9.Gfap.iGluSnFr.WPRE.SV40* [Addgene, 98930-AAV9], or *AAV5.GFAP(0.7).RFP.T2A.iCre* [Vector Biolabs, 1133]). Pups were placed on a digital stereotax and coordinates were zeroed at lambda. Four injection sites in a 2 × 2 grid pattern over V1 were chosen. Injection sites were 0.8–0.9 mm and 1.6–1.8 mm lateral, and 0 and 0.8–0.9 mm rostral. At each injection site, 30–120 nl of virus were

injected at a rate of 3 nl/s at two depths (0.1 mm and 0.2 mm ventral/below pia) using a microsyringe pump (UMP-3, World Precision Instruments).

For viral expression for the *in vivo* experiments, adult C57BL/6 mice were administered dexamethasone (5mg/kg, s.c.) >1 hour before surgery, and anesthetized using 1.5% isoflurane (Patterson Veterinary Supply, 78908115). After hair removal and three alternating swabs of 70% ethanol (Thermo Fisher Scientific, 04-355-720) and Betadine (Thermo Fisher Scientific, NC9850318), a custom-made titanium headplate was attached to the skull using cyanoacrylate glue and C&B Metabond (Parkell, S380). A 3mm craniotomy was made over the right visual cortex. Virus was injected at two sites in right visual cortex at coordinates centered on +2.4mm and +2.7mm medial/lateral, +0.35mm and +0.65mm anterior/posterior and -0.3mm dorsal/ventral from lambda. 300nL of *AAV5.GfaABC1D.GCaMP6f.SV40* (Addgene, 52925-AAV5) was injected at each site through a glass pipette and microsyringe pump (UMP-3, World Precision Instruments). After allowing at least ten minutes for viral diffusion, the pipette was slowly withdrawn and a glass cranial window implanted using a standard protocol.

Ex vivo two-photon (2P) imaging and uncaging

Coronal, acute V1 slices (400- μ m thick) from P28–32 (bath-application) and P27–42 (uncaging) mice were cut with a vibratome (VT 1200, Leica) in ice-cold slicing solution containing (in mM) 27 NaHCO₃, 1.5 NaH₂PO₄, 222 sucrose, 2.6 KCl, 2 MgSO₄, 2 CaCl₂. Slices were transferred to pre-heated, continuously aerated (95% O₂/5% CO₂) standard artificial cerebrospinal fluid (ACSF) containing (in mM) 123 NaCl, 26 NaHCO₃, 1 NaH₂PO₄, 10 dextrose, 3 KCl, 2 MgSO₄, 2 CaCl₂. Younger mice were sliced in the same solutions for GCaMP bath application of LY379268 and Baclofen (P20–25), Pink Flamingo (P20–22), and GluSnFR (P14–17). Slices

were kept at room temperature until imaging. Bath-application experiments were performed at room temperature and 2P uncaging experiments were performed at 29°C using an in-line heater (TC-324B and SH-27B, Warner Instruments). To block neuronal action potentials during all slice imaging experiments, TTX (1 μ M) was added to the ACSF > 10 min before imaging and remained in the circulating bath for the duration of the experiments.

Images were acquired on an upright microscope (Bruker Ultima IV) equipped with two Ti:Sa lasers (MaiTai, SpectraPhysics). Laser beam intensities were modulated using two independent Pockels cells (Conoptics) and images were acquired by scanning with linear galvanometers. Images were acquired with a 16 \times , 0.8 N.A. (Nikon) or a 40 \times , 0.8 N.A. (Nikon) water-immersion objective via photomultiplier tubes (Hamamatsu) using PrairieView (Bruker) software. For GCaMP imaging, 980 nm excitation and a 515/30 emission filter were used. For RFP imaging, 980 nm excitation and a 605/15 emission filter were used. For Pink Flamingo and Alexa Fluor 594 imaging, 1040 nm excitation and a 605/15 emission filter were used. Images were acquired at 1.42 Hz frame rate, 512 \times 512 pixels and 0.64–1.61 μ m/px resolution. For GluSnFR imaging only, images were acquired at 6.21 Hz frame rate, 200 \times 200 pixels and 0.64 μ m/px resolution, with 980 nm excitation and a 515/30 emission filter.

For bath-application experiments, a 5-min baseline was recorded to monitor spontaneous activity, after which receptor agonists were added along with a fluorescent dye (Alexa Fluor 594 Hydrazide) to assess the time at which drugs reached the imaging field/recording chamber (except for Pink Flamingo due to spectral overlap). An ACSF washout period (> 10 min), followed by a TTX incubation period (>10min), occurred between trials when imaging the same slice sequentially for bath-application of different receptor agonists or uncaging of different

RuBi-subtypes. To account for any changes resulting from prior agonist exposure or uncaging, we alternated the order of agonists between concentrations or RuBi-subtypes between slices.

For simultaneous 2P imaging and uncaging, a second Ti-Sa laser beam was tuned to 800 nm and controlled using an independent set of linear galvanometers from those used for scanning. Laser beam intensity was modulated using an independent Pockels cell (Conoptics) to achieve a power measurement of ~2–8 mW at the slice. The beam paths for imaging and uncaging were combined after the linear galvanometers using an 855-longpass dichroic mirror (T855lpxr, Chroma). The uncaging laser was calibrated each experimental day by burning spots into a fluorescent slide. RuBi- compounds (300 μ M) and TTX (1 μ M) were added to the ACSF >10 minutes before imaging each slice. Fields of view (FOV) were chosen based on the location of GCaMP expression, which was often biased to/brighter in deeper cortical layers (distance of FOV from pia: $615 \pm 196\mu\text{m}$ [mean \pm SD, n = 121 FOV]). Prior to imaging at each FOV, a 60-s period was recorded to identify potential uncaging sites. Areas of GCaMP expression that exhibited moderate levels of spontaneous Ca^{2+} activity were chosen as uncaging sites. For FOVs with sequential GABA/glutamate uncaging, a continuous 5-min recording was used to monitor activity in each FOV. For FOVs with three sequential rounds of glutamate uncaging, a continuous 12.5-min recording was used to monitor activity in each FOV. Each recording began with a 2.5-min baseline period and at the 2.5-min mark, neurotransmitter was uncaged with 10 x 100 ms pulses, 100 ms apart. Sequential recordings of GABA/glutamate uncaging within the same FOV were separated by > 20min. Rounds of sequential glutamate uncaging were separated by ≥ 25 min. Voltage from the uncaging laser Pockels cell was recorded to mark the time of uncaging pulses. Because RuBi-GABA and RuBi-glutamate are light-sensitive, care was taken to ensure experiments were carried out in minimal light. The computer screen and red-shifted

headlamp were covered with two layers of red filter paper (Roscolux #27 filter, Rosco) and all indicator lights on equipment were covered.

In vivo 2P imaging

In vivo 2P imaging was performed on the same microscope as *ex vivo* imaging, via a Nikon 16x, 0.8 N.A. water-dipping objective with a 2x-optical zoom (frame rate: 1.7Hz, FOV: 412 μ m², resolution: 512x512 pixels). Animals were given > 1 week after surgery for recovery and viral expression. They were then habituated on a custom-made circular running wheel over at least two days, and for a cumulative time of at least 2.5 hours, before recording. After habituation, mice were head-fixed on the wheel and movements were recorded by monitoring deflections of colored tabs on the edge of the wheel using an optoswitch (Newark, HOA1877-003). To compute wheel speed, a detected break in the optoswitch circuit was determined when the absolute value of the derivative of the raw voltage trace was at least 2 standard deviations above the mean. For recordings with little movement (std < 0.1), this threshold generated false positives, so a set threshold of 0.1 was used. The number of breaks in the optoswitch circuit per second was then calculated, and using the circumference and number of evenly spaced colored tabs at the edge of the wheel, the wheel speed was determined and used for all subsequent analyses using speed. Movement periods were defined by wheel speed ≥ 10 cm/s and movement bouts that were separated by ≤ 2 s were considered one event. To ensure that movement related dynamics were not included in stationary analysis, data was excluded from < 10 s around identified movement periods. GCaMP was imaged with 950nm excitation light and a 515/30 emission filter. Recordings lasted 30 minutes.

Ex vivo pharmacology

The following concentrations of each pharmacological reagent were used for experiments as indicated in the text: Tetrodotoxin Citrate (TTX, 1 μ M, Hello Bio); Carbenoxelone disodium (CBX, 50 μ M, Tocris Bioscience); R(+)-Baclofen hydrochloride (5–100 μ M, Sigma-Aldrich); (1S,3R)-ACPD (t-ACPD, 5–100 μ M, Tocris); LY 379268 disodium salt (100 μ M, Tocris); Alexa Fluor 594 Hydrazide (0.1–2 μ M, ThermoFisher Scientific); RuBi GABA trimethylphosphine (RuBi-GABA-Pme₃, 300 μ M, Tocris); RuBi-Glutamate (300 μ M, Tocris); CGP 55845 hydrochloride (10 μ M, Tocris); and LY 341495 (10 μ M, Tocris).

Immunohistochemistry and image quantification

After recording, slices from 2P imaging experiments were immersed in 4% PFA for 30 min and switched to 30% sucrose for one day at 4°C before being embedded in OCT and stored at -80°C. Slices were re-sectioned coronally at 40 μ m on a cryostat and then stored in cryoprotectant at -20°C until staining. For immunohistochemistry, sections were washed three times in 1X PBS for 5 min and permeabilized for 30 min with 0.01% Triton-X in 1X PBS. Sections were next blocked with 10% NGS (Abcam) for 1 h and incubated overnight with primary antibodies at 4°C in 2% NGS. The next day, they were washed three times in 1X PBS before incubating with secondary antibodies for 2 h at room temperature. Sections were washed three times in 1X PBS for 5 min before being mounted on slides with Fluoromount-G (SouthernBiotech).

To validate reduction of Connexin 43 (Cx43) protein in astrocytes transduced with AAVs to express GCaMP-GFP and Cre-RFP, primary antibodies for α -connexin-43 (1:1500, rabbit, Sigma-Aldrich), α -GFP (1:3000, chicken, Abcam), and α -mCherry (1:2000, rat, Thermo Fisher Scientific) in 2% NGS were used. Secondary antibodies include α -rabbit Alexa Fluor 405, α -

chicken Alexa Fluor 488, and α -rat Alexa Fluor 555 (all Thermo Fisher Scientific), which were all used at 1:1000 dilution. 60x multi-channel z-stack images were acquired on a CSU-W1 Spinning Disk Confocal (Nikon) from V1 in which AAVs were injected. To quantify loss of Cx43 in RFP⁺ and RFP⁻ astrocytes, Fiji (ImageJ) was used. Through batch processing, cell maps were created through a semi-automated pipeline to segment astrocytes, with *post hoc* ROI adjustments for vasculature artifacts. Multi-channel z-stacks were split into 405, 488, and 555 channels, and unstacked into sequential 8-bit z-plane images. For each z-plane, RFP⁺ and RFP⁻ astrocytes were detected using a Gaussian blur (sigma = 3), thresholding using the Phansalkar method (radius = 1000), and applying ImageJ's "Analyze Particles" (size > 175 μm^2 , circularity = 0–0.60) to outline ROIs using the wand tool. Corresponding Cx43 images were binarized and the Fiji plugin SynQuant⁶³ was used to detect Cx43 puncta number within each RFP⁺ and RFP⁻ astrocyte in a z-plane's cell map. Puncta counts were normalized to astrocyte area, and the normalized count from each z-stack was averaged for each slice.

2P image and data analysis

Individual-astrocyte cell maps for time series images were created in Fiji using the following process: For each FOV, an 8-bit z-projection of the time series was created. The z-projection was binarized using the 'Auto Local Threshold' feature, using the Niblack method and a radius of 30 or 75, for 16 \times and 40 \times images, respectively. Cell maps were drawn on binarized images using a combination of the Lasso and Blow Tool and freehand drawing tool in Fiji, and verified on the z-projected image. Cell maps were also verified against a static indicator of astrocyte morphology when available (EAAT2-tdT⁺ mice for bath-application of LY379268 and Baclofen; GFAP(0.7)-RFP-T2A-iCre in Cx43^{flxed} mice). To load cell masks into AQUA, regions were saved to the

ROI manager and filled in with a color. The regions were projected onto a black image the same size as the original (512×512 pixels). The overlay of regions was flattened, converted to an 8-bit image, and saved as a tiff. For the 12.5-min recordings with sequential rounds uncaging glutamate, drift of the slice in X and Y was corrected post-hoc using moco⁶⁴.

AQuA: GCaMP and GluSnFR 2P image sequences were analyzed using AQuA²⁰ and custom MATLAB code (MATLAB R2018b). Signal detection thresholds were adjusted for each video to account for differences in noise levels after manually checking for accurate AQuA detection. Cell maps were loaded into AQuA to define cells consistently over multiple time-series featuring the same FOV. For all bath-application experiments, the direction of pia was marked as anterior. For 2P uncaging experiments, the uncaging site was marked as a 3×3 -pixel landmark.

Bath-application event-based analysis: For Baclofen and t-ACPD Ca^{2+} imaging experiments, *Event count per frame* was quantified by counting all AQuA-detected events, new or ongoing, in each frame (Fig. 3.1c). *Percent of field active* values were calculated by recording the number of active pixels in each frame, as determined by the frame-by-frame footprints of AQuA-detected events. These values were normalized by total number of active pixels in the recording and multiplied by 100. For the *Percent of field active* dose-response curve (Fig. 3.1e), the percent of field active values from all frames within the chosen timepoints were averaged by slice. *Event propagation* was calculated by summing the growing propagation from all cardinal directions, using the AQuA feature *propGrowOverall*. For dose-response curves for discrete event features (area, duration and propagation [Fig. 3.1f–h]), all detected Ca^{2+} events within the chosen timepoints were averaged by slice.

The frame the agonist entered the recording chamber was estimated using fluorescence from Alexa Fluor 594 (0.1–2 μM) added to the ACSF reservoir along with agonist. The frame agonist entered the recording chamber was estimated using the maximal curvature method on frames 1–600 of the raw Alexa Fluor 594 fluorescence trace. The *maximum curvature method*⁶⁵ defines the onset fluorescence changes as the point of maximum curvature during the rising phase of the signal. To identify this point, traces were fit using a modified Boltzmann’s sigmoidal equation:

$$f(x) = \frac{a}{1 + e^{(b-x)/d}} + c$$

where a is the difference between the minimum and the maximum fluorescence, b is the inflection point, c is the baseline fluorescence and d is the slope, using a nonlinear least squares algorithm (Levenberg-Marquardt) in MATLAB (Mathworks). Next, the frames of maximum curvature were calculated by setting the fourth derivative of the fitted curve equal to zero and solving for its three solutions. The earliest frame identified out of these three solutions was recorded as the onset frame.

Bath-application ROI-based analysis: Pink Flamingo and GCaMP imaging experiments were analyzed using ROI-based approaches in Fiji. To identify responding cells in Pink Flamingo experiments (Extended Data Fig. 3.1j), sigmoidal curves were fit to $\Delta F/F$ traces using the modified Boltzmann’s sigmoidal equation detailed above. Cells were defined as “responding” if the difference between the minimum and maximum values of the fit curve (a in the Boltzmann’s sigmoidal equation) $>$ baseline noise (3 SD of baseline fluorescence). Responding cells were defined as “increasing” if $f(x_{start}) < f(x_{end})$ and decreasing if $f(x_{start}) > f(x_{end})$.

To identify fluctuations in Pink Flamindo and GCaMP fluorescence (Extended Data Fig. 3.1k), peaks were detected from $\Delta F/F$ traces from individual cells. Peaks were counted if they were 3 SD above the mean baseline fluorescence, had a minimum peak width of 5 frames and a minimum distance of 10 frames between detected peaks. The baseline period was defined as all frames before the frame of agonist entry. For GCaMP, all astrocytes exhibiting ≥ 1 AQuA-detected event during the 10-min recording were run through peak finding. For Pink Flamindo, all detected astrocytes were run through peak finding.

For GCaMP experiments, the frame agonist entered the recording chamber was estimated using the fluorescence from Alexa Fluor 594 (0.1–2 μM) added to the ACSF reservoir along with agonist. Time of agonist entry in the recording chamber was estimated by identifying the first frame Alexa Fluor 594 fluorescence reached ≥ 3 SD above baseline mean (frames 1–300); only frames > 375 were considered for evaluation of exceeding the threshold. For Pink Flamindo experiments, dye was not added with agonist to avoid spectral overlap. Time of agonist entry in the recording chamber was estimated by adding 90 frames (the average number of frames for ACSF to travel from the reservoir to the recording chamber) to the frame agonist was added to the reservoir of ACSF.

2P uncaging event-based analysis: Individual astrocytes were excluded from analyses (Fig. 3.2–3.4, Extended Data Fig. 3.2–3.7) if the baseline event rate changed significantly. Changes in baseline event rate for each cell were determined by performing Poisson regression of events in 1-s bins during the period from 90–10s pre-uncaging. Cells with a regression coefficient with $p < 0.1$ at baseline and with > 5 AQuA-detected events throughout the recording were excluded from all analyses, except for Extended Data Fig. 3.7d RuBi-glutamate uncaging control. $\Delta F/F$ values

in raster plots (Fig. 3.2h and 3.3c) were calculated using the AQuA output *dffMatFilter(:, :, 2)*, the $\Delta F/F$ traces from events after removing the contributions from other events in the same location. For the Sholl-like analysis (Fig. 3.3h), events were sorted into 50 μm bands radiating out from the uncaging site based on the minimum distance between an event and the uncaging site at event onset (using the AQuA output *ftsFilter.region.landmarkDist.distPerFrame*). In order to categorize events as propagative or static (Fig. 3.4d–m and Extended Data Fig. 3.5b–j, 3.6 and 3.7c), the total propagation distance of each event was computed by summing the growing propagation from all cardinal directions, using the AQuA feature *propGrowOverall*. Events were categorized as propagative if the total propagation distance $> 1\mu\text{m}$.

Statistics for Fig. 3.1–3.3 and associated Extended Data Figures

All statistical tests used and exact n values can be found for each figure in the corresponding figure legend. Adjustments for multiple comparisons using Bonferroni-Holm correction were implemented using *fwer_holmbonf*⁶⁶. Significance levels defined as the following: ns: $p \geq 0.05$, *: $p < 0.05$, **: $p < 0.01$, ***: $p < 0.001$.

Permutation testing: Statistical significance for time-series (t-series) data was computed using permutation testing with custom-written code in MATLAB. 10,000 permutations were run and one- or two- sided p -values for each time point were calculated. p -values were corrected for multiple comparisons using the Benjamini-Yekutieli procedure (implemented using ref. ⁶⁷) with a False Discovery Rate (FDR) ≤ 0.05 .

Data were shuffled/permuted in the following way: To test change in event number/cell (Fig. 3.1c, Extended Data Fig. 3.2b and 3.3g,h), events were shuffled independently for each

active cell (≥ 1 AQuA-detected event) in each t-series. For each active cell, events were randomly placed in time bins spanning the duration of the recording (time bins = 60s [Fig. 3.1c] and 30s [Extended Data Fig. 3.2b and 3.3g,h]) and the change in number of events/time bin was calculated as for the experimental data. Permuted changes in event number/cell were averaged across active cells in each t-series and across all t-series to obtain the permuted mean for one round of permutation testing.

To test change in event number/ band (Fig. 3.3h), permutation tests were run separately for each band and events were shuffled independently for each t-series. For each t-series, events from the tested band were randomly placed in 30 s time bins spanning the duration of the recording, and the change in event number/30 s was calculated as for the experimental data. Permuted changes in event number/30 s were averaged across all t-series to obtain the permuted mean for one round of permutation testing. To test magnitude of change in experimental data versus permuted data, two-sided p -values were calculated as:

$$\frac{(\# \text{ of times } |\text{permuted change}| \geq |\text{experimental change}|) + 1}{\# \text{ of permutations} + 1}$$

For testing increases in $\Delta F/F$ (Extended Data Fig. 3.1d), frames were shuffled independently for each t-series. For each t-series, the average $\Delta F/F/\text{frame}$ from active regions (≥ 1 AQuA-detected event in either condition [baclofen or t-ACPD]) was calculated, the frame order was shuffled, and the mean $\Delta F/F/30\text{s}$ was calculated. Permuted mean $\Delta F/F$ was averaged across all t-series to obtain the permuted mean for one round of permutation testing. To test magnitude of increases in experimental data versus permuted data, one-sided p -values were calculated as:

$$\frac{(\# \text{ of times the permuted mean } \geq \text{the experimental mean}) + 1}{\# \text{ of permutations} + 1}$$

Statistics for Fig. 3.3i–l, Fig. 3.4, and associated Extended Data Figures

2P uncaging grid-based ROI analysis: Grid-based regions of interest (ROIs) were determined by dividing the 300 x 300 μm imaging field into a uniform 20 x 20 μm grid (Fig. 3.3i–l). Each identified Ca^{2+} event was assigned to the ROI in which the centroid of its spatial footprint was located. ROIs with any baseline events were identified as ROIs with ≥ 1 events in the baseline window 60–0s before uncaging. “Active” ROIs for each NT were identified as ROIs with a $\geq 50\%$ increase in event rate in the window 0–120s after uncaging for that NT, as compared with the rate during the baseline window. Active ROIs were a subset of ROIs with baseline events, as the relative increase in event rate is not defined when there are no baseline events, which results in division by 0. The distance from the uncaging site to each active ROI was determined using the Euclidean distance between the uncaging site, at (0, 0), and the center of each grid ROI (Fig. 3.3j).

The fraction of overlap (*i.e.*, Jaccard index) O_i between active ROIs for GABA and glutamate were determined for the i th field of view by:

$$O_i = \frac{|A_{\text{GABA},i} \cap A_{\text{glutamate},i}|}{|A_{\text{GABA},i} \cup A_{\text{glutamate},i}|}$$

where $A_{\text{GABA},i}$ and $A_{\text{glutamate},i}$ are the sets of active ROIs for GABA and glutamate, respectively.

The overall fraction of overlap O between active ROIs for GABA and glutamate was computed as the mean of the individual O_i (Fig. 3.3l).

To determine if the observed fraction of overlap was expected due to chance, a distribution of $N = 10,000$ surrogate fractions of overlap was computed. The k th surrogate value, $\tilde{O}^{(k)}$ was computed as above, but replacing, for each NT, the set of active ROIs $A_{\text{NT},i}$ with a new

set, $\tilde{A}_{NT,i}^{(k)}$, which was chosen as a random subset of size $|A_{NT,i}|$ of the set of ROIs with any baseline events for that NT. The p -value for this comparison was estimated⁶⁸ as

$$p = \frac{(\# \text{ of } \tilde{O}^{(k)} \geq O) + 1}{N + 1} \quad (1)$$

Propagation probability (Fig. 3.4b): Each Ca^{2+} event was identified as “growing in the depth axis” if the frontier of that event’s spatial footprint extended over time either toward the pia or away from the pia, as determined by the posterior and anterior component of the *propGrowOverall* metric computed *via* segmentation by AQuA²⁰.

The probability of events growing in the depth axis was computed separately for recordings of GABA and glutamate uncaging within each examined time window. Probabilities were estimated for the baseline window of 60–0s before uncaging, as well as in nonoverlapping 30s bins ranging from 0–150s post-uncaging, by computing the fraction of events that were identified as growing in the depth axis among all events from all recordings within the relevant time window. The change in the probability of events growing in the depth axis was then estimated for each bin as the difference between the fraction of events growing in the depth axis for that bin versus for the baseline period.

To empirically determine the distribution of each of these estimators, we performed this same procedure for estimating the probability of events growing in the depth axis for each NT and time bin on surrogate data generated by hierarchically bootstrapping Ca^{2+} event data, where the hierarchy was sampled cells within sampled recordings (i.e., all events for an individual cell-recording always remained together); this procedure was repeated 10,000 times for each bin. Standard errors were computed as the standard deviation of these empirical distributions.

To determine the probability of observing effects this large under a null hypothesis of no effect of time on the probability of events growing in the depth axis, we computed the distribution of the estimator under an imposed condition in which the overall temporal structure of astrocyte Ca²⁺ events was disrupted. To do this, we performed the same procedure as above for estimating the probability of events growing in the depth axis for each bin, but on surrogate data generated by circularly shifting the timing of each individual cell's Ca²⁺ events from 90s before to 150s after uncaging by its own independent, uniform random shift between 0s and 240s; this procedure was repeated $N = 10,000$ times for each bin. As it was unknown whether event propagation would increase or decrease post-uncaging, two-sided p -values were estimated⁶⁸ as

$$p = \frac{(\# \text{ of } |\tilde{X}^{(k)}| \geq |X|) + 1}{N + 1} \quad (2)$$

where X denotes the actual observed value of the estimator, and each $\tilde{X}^{(k)}$ is the value of the estimator computed from the k th shifted dataset. These p -values were adjusted across tested time bins and NTs using the Benjamini-Hochberg procedure to obtain q -values, as implemented in statsmodels 0.12.2 (ref⁶⁹).

Event feature changes (Extended Data Fig. 3.4a,b): Each Ca²⁺ event is assigned several metrics by AQUA-segmentation²⁰, including size (*area*, *perimeter*, *circMetric* [circularity, based on area and perimeter]), amplitude (*dffMax*), and dynamics (*rise19* [rise time], *fall91* [fall time], *decayTau* [decay time constant], *width11* [duration]). For each non-propagation metric, the mean metric value among events was computed separately for recordings of GABA and glutamate uncaging for the baseline window 60–0s before uncaging, as well as in nonoverlapping 30s bins

from 0–150s post-uncaging. For each bin, the ratio of that bin’s mean metric value to the baseline mean metric value was computed.

AQuA metrics also capture information about events’ directional propagation. Each Ca^{2+} event was identified as “growing” or “shrinking” in each cardinal direction if the frontier of that event’s spatial footprint extended or receded, respectively, over time in that direction, as determined by the components of the *propGrowOverall* and *propShrinkOverall* metrics. For each propagation metric, the change in the probability of events growing or shrinking in each axis was computed separately for recordings of GABA and glutamate uncaging within each examined time window, as above in *Propagation probability*, but using the “growing” or “shrinking” identifiers for each cardinal direction.

To empirically determine the distribution of each of these estimators (*i.e.*, binned post/baseline ratio for non-propagation metrics, binned change in growing/shrinking probability for propagation metrics), we performed the same procedures for computing each metric’s relevant estimators for each NT and time bin outlined above on 10,000 surrogate datasets generated by hierarchically bootstrapping Ca^{2+} event data, as described in *Propagation probability*. Standard errors were computed as the standard deviation of these empirical distributions.

To determine the probability of observing effects this large under a null hypothesis of no effect of time on the probability of events growing in the depth axis, we computed the distribution of each estimator under 10,000 realizations of an imposed condition in which the overall temporal structure of astrocyte Ca^{2+} events was disrupted by randomly circularly shifting each cell’s Ca^{2+} events, as described in *Propagation probability*. As it was unknown whether event propagation would increase or decrease post-uncaging, two-sided *p*-values were estimated

using equation (2) above⁶⁸. These p -values were adjusted across tested time bins and NTs using the Benjamini-Hochberg procedure to obtain q -values, as implemented in statsmodels 0.12.2 (ref. ⁶⁹).

Comparison of in vivo and ex vivo event propagation (Fig. 3.4d): Events were categorized as propagative or static, as outlined above in the *2P uncaging event-based analysis* section. The fraction of propagative events observed *in vivo* and *ex vivo* was calculated using baseline events. Ca^{2+} events in *in vivo* recordings were labeled as “baseline events” if they occurred during periods when the mouse was stationary, as outlined above in the *in vivo 2P imaging* section. Ca^{2+} events in *ex vivo* recording were labeled as “baseline events” if they occurred in neighboring astrocytes (*i.e.* cells not directly stimulated by NT) during the 60–0s before NT uncaging.

To determine the distribution of the two median propagative event fractions empirically, we computed the medians of 10,000 bootstrapped samples of the per-recording fractions for each setting. Standard errors for each statistic were determined from the standard deviations of these empirical distributions.

Computing rate changes for propagative and static events (Fig. 3.4f, j and Extended Data Fig. 3.6b–c): The overall rates of propagative and static events for neighboring astrocytes were computed separately for recordings of GABA and glutamate uncaging.

For each event class (*i.e.*, propagative and static events), for each recording, the event rate was computed in each time window as the total number of events from all neighboring cells in that recording in the given time window divided by the duration of that time window. These recording-level rates were computed for the baseline window of 60–0s before uncaging and in

nonoverlapping 30s bins ranging from 0–150s post-uncaging. For each recording, the relative rate of propagative and static events was computed for each time bin as the ratio of the event rate for the given event class in that time bin divided by the corresponding event rate in the baseline window. For each time bin, the overall relative rate was estimated as the median of the per-recording relative rates in that time bin.

To determine the distribution of each of these relative rate estimators empirically, we performed this same procedure for estimating relative event rates on surrogate data generated by hierarchically bootstrapping Ca^{2+} event data 10,000 times for each bin (as above in *Propagation probability*). Standard errors were computed as the standard deviation of these empirical distributions.

To determine the probability of observing effects this large under a null hypothesis of no effect of time post-uncaging on the rate of astrocyte Ca^{2+} events, we computed the distribution of the relative rate estimators under an imposed condition in which the overall temporal structure of astrocyte Ca^{2+} events was disrupted *via* a random circular shift of the events in each cell, as above in Fig. 3.4b; this procedure was repeated $N = 10,000$ times for each bin. Motivated by results in bath application experiments above demonstrating robust aggregate astrocyte Ca^{2+} activity increases in response to agonism of glutamate receptors (Fig. 3.1h), one-sided p -values were estimated from these permuted datasets, as in equation (1) above. These p -values were adjusted across tested time bins and NTs using the Benjamini-Hochberg procedure to obtain q -values, as implemented in statsmodels 0.12.2 (ref. ⁶⁹).

Determining responding cells based on static and propagative events (Fig. 3.4h,k and Extended Data Fig. 3.6e–f): The overall rates of propagative and static events were computed for each neighboring astrocyte, with paired measurements made for recordings of GABA and glutamate uncaging. For each neighboring astrocyte, for each event class (*i.e.* propagative and static events), the event rate was computed in each time window as the total number of events from that cell in the given time window divided by window’s duration (baseline window: 60–0s before uncaging, response window: 0–120s after NT-uncaging; Extended Data Fig. 3.5c). Relative event rates were calculated as for Fig. 3.4f, j and Extended Data Fig. 3.6b–c above. Cell-recording combinations with zero events of a given type in the baseline window were excluded for computation of relative rates of propagative (GABA: 36 cell-recordings [26.7% of total]; glutamate: 37 [32.2%]) and static (GABA: 0; glutamate: 0) events, as the relative rate would require a division by zero and be undefined in those cases. Astrocytes were identified as “responders” with a particular event type (*i.e.*, static or propagative) to GABA or glutamate if their relative rate of that type of event was ≥ 1.5 for the corresponding NT uncaging recording (Extended Data Fig. 3.5d). The fraction of astrocytes that were responders was computed for each individual recording, as well as the overall fraction of responders across all recordings for each NT.

To determine the distribution of these overall responder fractions, we performed this same procedure for estimating relative event rates on surrogate data generated by hierarchically bootstrapping Ca^{2+} event data 10,000 times (as above in *Propagation probability*). Standard errors were computed as the standard deviation of these empirical distributions.

To determine whether there were significant differences between the overall responder fractions for GABA and glutamate, we computed the distribution of the difference between these

two fractions under an imposed condition in which there was no systematic difference between GABA and glutamate. To do this, we performed the same procedure as above for estimating the difference between the overall responder fractions for “GABA” and “glutamate”, but on surrogate data generated by, for each cell, swapping the labels for “GABA” and “glutamate” responses from that in the experimental data with probability 1/2; this procedure was repeated 10,000 times. As it was unknown *a priori* whether GABA or glutamate would have a higher fraction of responder cells, a two-sided *p*-value was estimated as in equation (2) above.

Decoding NT identity from propagative event responses (Fig. 3.4i): To quantify the extent to which the observed difference in propagative event responses to uncaged glutamate and GABA enabled reliable identification of NT identity on a trial-by-trial basis, we built a simple classifier that took as input a single value, the relative change in propagative event rate across a FOV in the window 0–120s post-uncaging relative to the window 60–0s pre-uncaging, and classified that FOV as responding to glutamate if the value was \geq a set threshold, and GABA if the value was $<$ the threshold. To evaluate this classifier’s performance, we built a receiver operating characteristic (ROC) curve by varying the classification threshold across the entire domain of the feature, and at each value of the threshold, computing the empirical true positive rate and false negative rate of the classifier. With the threshold fixed in the ROC analysis, the classifier did not have any remaining free parameters, so did not need to be trained on data and was therefore not a function of any of the data, obviating the need for cross-validation. We computed the area under the ROC curve (AUC) using the trapezoidal rule. To determine the distribution of the observed AUC statistic, we performed this same analysis on 10,000 surrogate datasets generated by bootstrapping (*i.e.*, resampling FOVs with replacement). To determine whether the observed

AUC statistic was above 0.5 (indicating completely non-informative decoding) to a degree greater than expected by chance alone, we performed this same analysis on 10,000 surrogate datasets generated by permuting the NT labels.

Determining correlations between GABA and glutamate responses (Fig. 3.4I): To determine whether individual cells' responses to GABA and glutamate—as determined in 4h above—were correlated, we computed the Spearman ρ between the binary paired responses to GABA and glutamate across cells which could be assessed in both conditions (*i.e.*, had > 0 propagating baseline Ca^{2+} events in both recordings) using SciPy 1.6.2 ⁷⁰. To determine the probability of observing a correlation at least this large under a null hypothesis of independence between cells' responses for GABA and glutamate, we computed Spearman ρ on surrogate data in which the identities of the cells' responses to GABA and glutamate were independently permuted; this procedure was repeated 10,000 times. To maintain the ability to identify correlation or anticorrelation, we estimated a two-sided p -value from these surrogate values, as in equation (2).

To complement this analysis, we computed the fraction of overlap (*i.e.*, Jaccard index) between the sets C_{GABA} and C_{glu} of cells that were responders to GABA and glutamate, respectively:

$$O = \frac{|C_{\text{GABA}} \cap C_{\text{glu}}|}{|C_{\text{GABA}} \cup C_{\text{glu}}|}$$

This statistic is larger when the fraction of overlap between responders for the two neurotransmitters is larger. To determine the probability of observing an overlap at least this large under a null hypothesis of independent responses for GABA and glutamate, we computed

this same statistic, but on 10,000 permuted surrogate datasets, as above. To determine significant overlap, we estimated a one-sided p -value from these surrogate values, as in equation (1).

Segregating responding cells based on baseline propagation (Fig. 3.4m): For each neighboring astrocyte with propagative events during the baseline period of 60–0s pre-uncaging, we computed the fraction of baseline events that were propagative ($\#$ propagative baseline events / $\#$ all baseline events). Separately for GABA and glutamate, we used the propagative fraction across all given astrocytes to define the threshold fraction of baseline propagative activity, f_{50} , as the 50th percentile of all observed values; cells with fractions $< f_{50}$ were said to have “low baseline propagation”, while cells with fractions $\geq f_{50}$ were said to have “high baseline propagation” (Extended Data Fig. 3.5e, top). The fraction of astrocytes that were responders with propagative events to GABA or glutamate were separately estimated from amongst those astrocytes that had low baseline propagation and those that had high baseline propagation, as described above in *Determining responding cells based on static and propagative events*.

Similarly for each neighboring astrocyte with baseline propagative events, we computed the rate of all events within the baseline period. Separately for GABA and glutamate, we used the baseline event rate across all neighboring astrocytes to define the threshold baseline event rate, r_{50} , as the 50th percentile of all observed values; cells with baseline rates $< r_{50}$ were said to have “low overall baseline event rates”, while cells with fractions $\geq r_{50}$ were said to have “high overall baseline event rates” (Extended Data Fig. 3.5e, bottom). The fraction of astrocytes that were responders with propagative events to GABA or glutamate were separately estimated from amongst those astrocytes that had low overall baseline event rates and those that had high overall baseline event rates, as above.

To determine the distribution of these responder fractions (amongst astrocytes with low and high baseline propagation, or amongst astrocytes with low and high overall baseline event rates), we performed the same procedure for estimating these fractions on surrogate data generated by hierarchically bootstrapping Ca^{2+} event data 10,000 times (as above in *Propagation probability*). Standard errors were computed as the standard deviation of these empirical distributions.

For each NT, we next sought to determine whether there were significant differences between the fraction of astrocytes that were responders with propagative events amongst cells within the two groupings (*i.e.*, low vs. high baseline propagation; low vs. high overall baseline event rate). Separately for GABA and glutamate, for each group comparison, we computed the difference between the two responder fractions, as well as the distribution of this difference under an imposed condition in which there was no systematic difference in uncaging response between astrocytes in the two groups. To do this, we performed the same procedure as above for estimating responder fractions in the specified groups (*e.g.*, “low baseline propagation” and “high baseline propagation”) as well as the difference between the two, but on surrogate data generated by permuting the group labels; this procedure was repeated 10,000 times. As it was unknown *a priori* which group in either comparison—low or high baseline propagation, or low or high overall baseline event rate—would have a higher fraction of responder cells, a two-sided *p*-value was estimated from these surrogate values, as in equation (2).

Figures

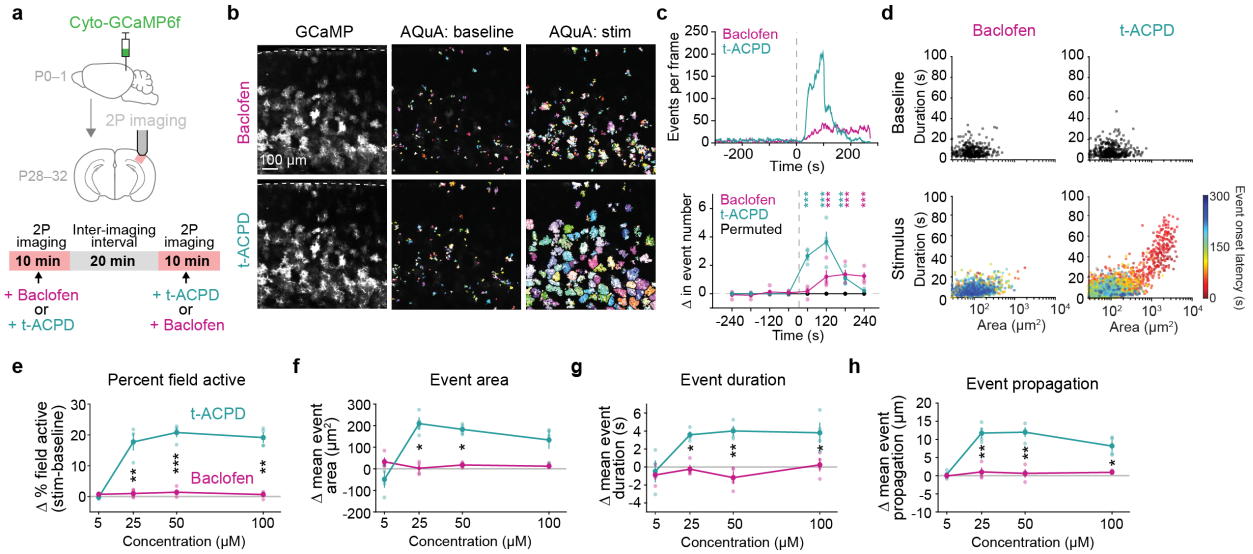


Figure 3.1. Direct GABAergic and glutamatergic receptor activation drive distinct astrocyte Ca^{2+} activity.

(a) Experimental strategy for expression of cyto-GCaMP6f and 2P imaging astrocytic Ca^{2+} in acute V1 cortical slices during pharmacological activation via bath-application. Receptor agonists were sequentially bath-applied to the same slice, with an inter-imaging interval of >20min, including >10min wash-out period. (b) Representative astrocytic GCaMP6f fluorescence (left column) during bath-application of GABA_B-specific agonist baclofen (50 μM , top row) and mGluR agonist t-ACPD (50 μM , bottom row). Dotted line denotes pia. All AQUA-detected events 300s before (middle column) and after (right column) bath-application of agonists, from the same slice shown on left. (c) Top: Representative time-series traces (AQUA events per frame) of FOVs in B. Bottom: Average change in the events/minute compared to average baseline. 300–0s before and 0–240s after bath-application of agonists used to calculate change in events/60s for each active astrocyte (≥ 1 AQUA-detected event) and averaged for each slice. Data shown by slice ($n = 4$ slices stimulated with 50 μM agonist, light dots) and mean \pm standard error of the mean (sem) (solid dots and error bars). Permutation test used to determine significance. p -values for all timepoints are in Extended Data Table 3.1. All traces are aligned to 0s, the frame of agonist entry in the imaging chamber. (d) Scatter plots of the area and duration of individual Ca^{2+} events at baseline (top row, black) and after bath-application of baclofen (bottom left) or t-ACPD (bottom right). Bottom row: events following bath-application of agonists color-coded by onset time. Dots represent individual Ca^{2+} events from $n = 4$ slices stimulated with 50 μM agonist. (e–h) Dose-response curves showing average change in Ca^{2+} features with bath-application of baclofen (pink) or t-ACPD (green) at four concentrations. Agonist order alternated between conditions: Baclofen was added first at 5 and 50 μM and second at 25 and 100 μM . Change calculated by comparing 120s before and after agonist entry. Data shown by slice ($n = 4$ slices, 4 mice for each concentration, light dots) and mean \pm sem (solid dots and error bars). Paired t-tests at each concentration compare activity changes induced by each agonist. p -values corrected for multiple comparisons using Bonferroni-Holm correction with FWER ≤ 0.05 . p -values for all concentrations and features are in Extended Data Table 3.2.

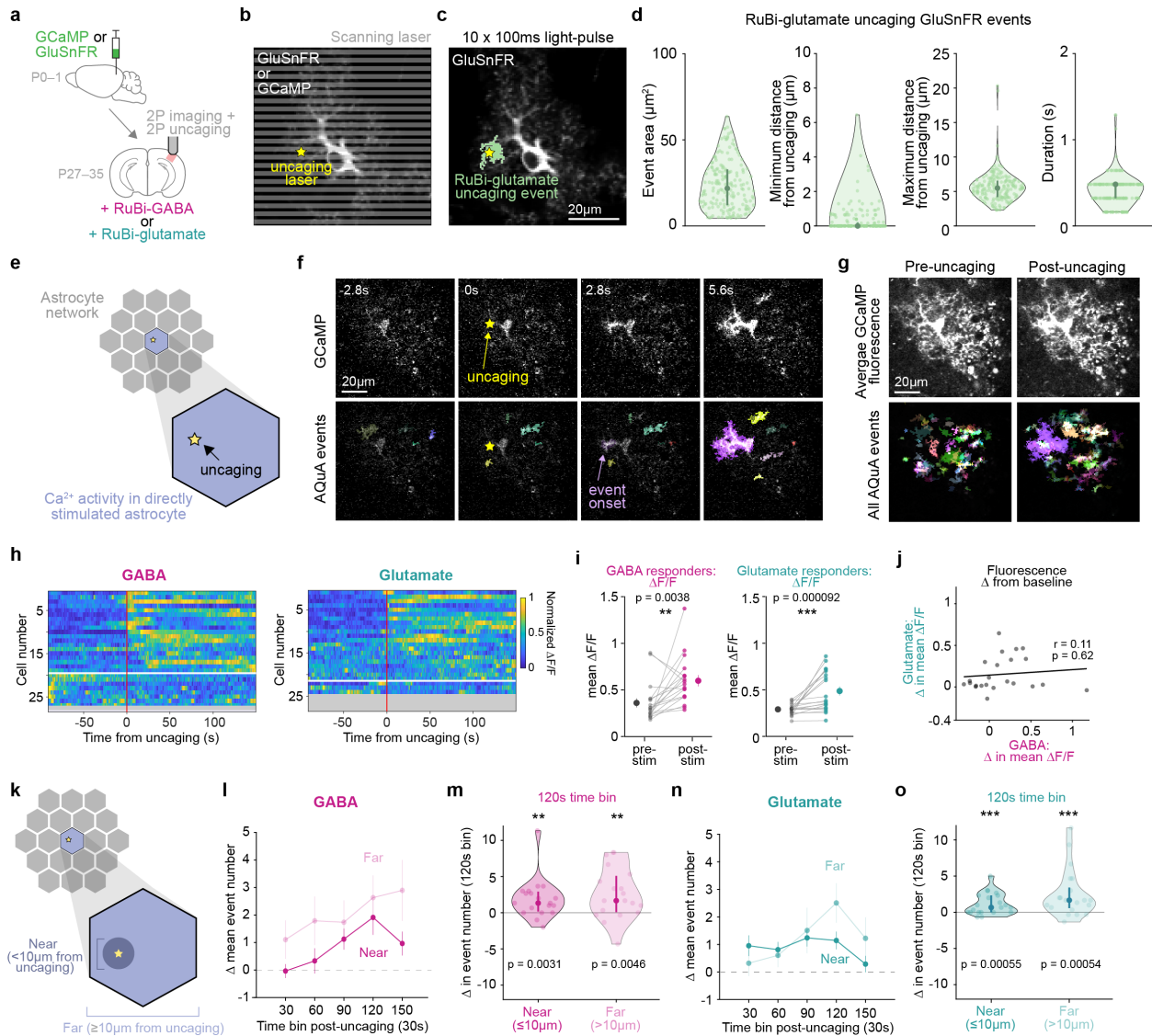


Figure 3.2. Subcellular, spatiotemporally restricted release of NTs increases Ca^{2+} activity within directly stimulated astrocytes.

(a) Experimental strategy for simultaneous 2P imaging of astrocyte Ca^{2+} (Cyto-GCaMP6f) or extracellular glutamate (GluSnFR), and 2P uncaging of NTs in acute V1 cortical slices. (b) Imaging/uncaging schematic. Gray lines = scanning laser. Yellow star = NT uncaging site. (c) To validate spatial precision of 2P uncaging, RuBi-glutamate was uncaged at a GluSnFR-expressing astrocyte. Yellow star = uncaging laser location; green = GluSnFR event footprint post-uncaging. (d) GluSnFR event features after RuBi-glutamate uncaging. Data shown by individual glutamate events, median, 25th and 75th percentile ($n = 72$ trials, 12 recordings, 4 slices, 2 mice).

(e) Schematic illustrating analysis throughout figure is of Ca^{2+} activity from astrocyte directly stimulated by uncaging. (f) Representative GCaMP6f fluorescence time-course in an individual astrocyte seconds before and after RuBi-GABA uncaging. Top row: raw fluorescence; bottom

Figure 3.2 continued on next page

Figure 3.2 continued

row: overlaid AQuA events. Yellow star = uncaging location and frame. **(g)** Average GCaMP fluorescence 150–0s pre-uncaging (left column) and 0–150s post-uncaging (right column) from astrocyte in **f**. Top row: raw fluorescence; bottom row: all AQuA-detected Ca^{2+} events. **(h)** Ca^{2+} activity in astrocytes directly stimulated by GABA (left) or glutamate (right) uncaging. Each row shows average $\Delta\text{F}/\text{F}$ traces from AQuA-detected events/cell, normalized individually between 0–1 for each cell. Cells sorted by onset time (first post-stim peak \geq threshold [mean baseline $\Delta\text{F}/\text{F} + 3\text{SD}$], with threshold calculated by cell). Red line = NT uncaging time. White line separates responding (above) and non-responding cells (below). Responders are defined as any astrocyte with ≥ 1 post-stim frame with $\Delta\text{F}/\text{F} \geq$ threshold. Greyed-out rows represent cells excluded due to significant event frequency increases or decreases during the baseline period (see *2P uncaging event-based analysis* methods). **(i)** Mean fluorescence pre- and post-stim from astrocytes responding to direct GABA (left) or glutamate (right) uncaging. 90–0s before and 0–150s after uncaging used to calculate mean $\Delta\text{F}/\text{F}$ pre- and post-stim/astrocyte. Data shown by cell (light dots and grey lines) and mean \pm sem (dark dots and error bars). (For **i**, **l–o**, $n = 19/27$ directly stimulated cells responded to GABA and 21/24 to glutamate from $n = 7$ slices, 4 mice). Wilcoxon signed-rank test compare pre-and post-stim values. **(j)** Fluorescence change in directly stimulated astrocytes following GABA and glutamate uncaging. 90–0s before and 0–150s after uncaging used to calculate mean change per cell. Pearson’s correlation shows no significant relationship between fluorescence change following GABA and glutamate uncaging ($p = 0.62$). **(k)** Schematic illustrating that Ca^{2+} events within directly stimulated astrocyte are divided into events *near* and *far* from uncaging site. Note: events far from uncaging site are outside the radius of NT spread (d, “maximum distance from uncaging”), but still within the directly stimulated cell. **(l, n)** Event frequency change near and far from GABA **(l)** and glutamate **(n)** uncaging within responding, directly stimulated cells. 90–0s before and 0–150s after uncaging used to calculate event number/30s. Data shown as mean \pm sem. **(m, o)** Event frequency change during a period of generally high activity (90–120s after uncaging, “120s” bin) from **l** & **n**. Data shown by cell, median, 25th and 75th percentile. Wilcoxon signed-rank test compare change from baseline for each cell compartment.

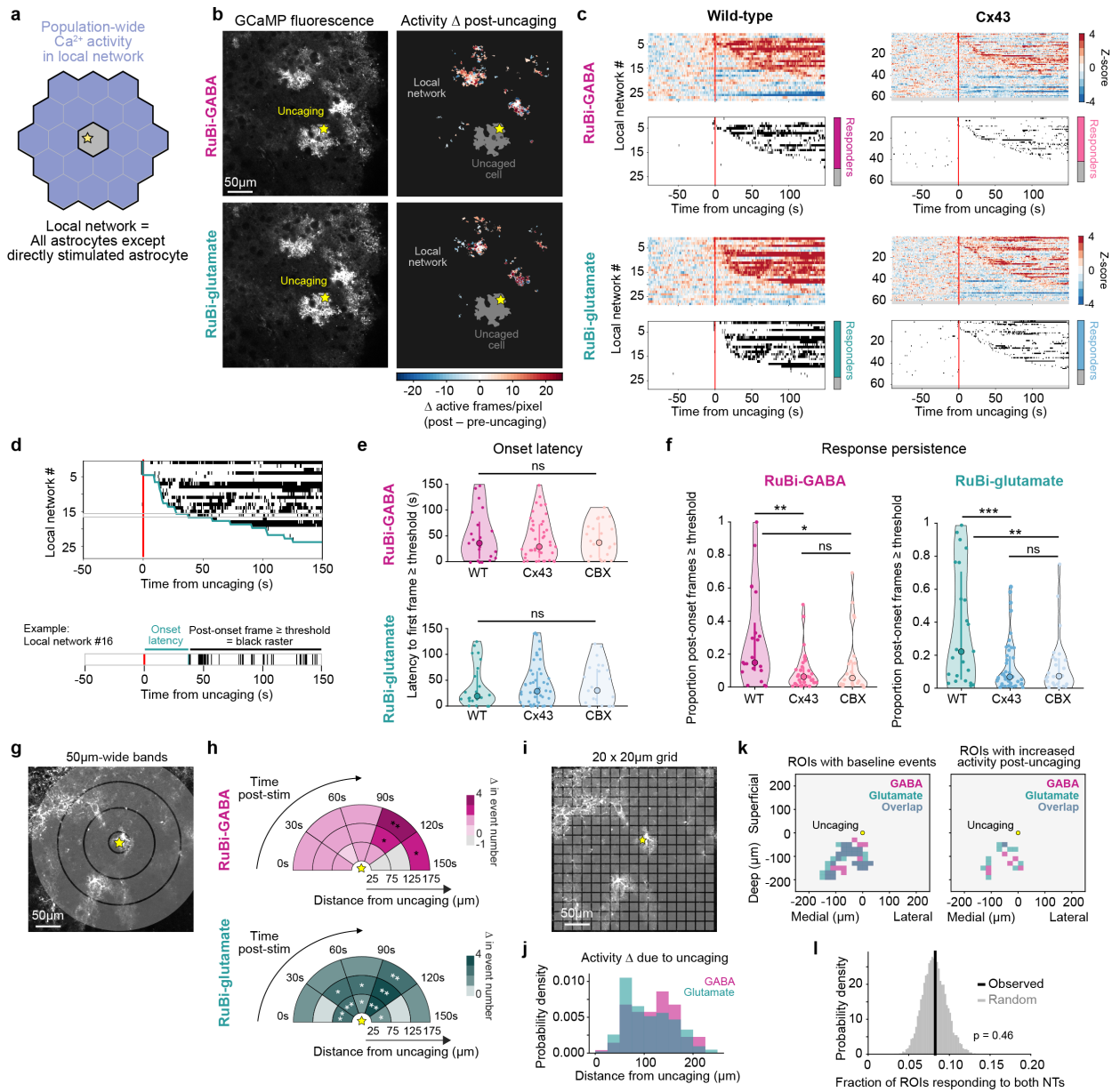


Figure 3.3. Subcellular release of GABA and glutamate increases Ca^{2+} activity in the local astrocyte network via Cx43.

(a) Schematic illustrating analysis throughout figure is of population-wide Ca^{2+} activity of all astrocytes in the FOV that are not directly stimulated by uncaging (*local network*). (b) Left: Representative astrocytic GCaMP6f fluorescence in a V1 slice during 2P uncaging of RuBi-GABA (top) and RuBi-glutamate (bottom). Right: Representative spatial heatmaps of Ca^{2+} activity changes in the local astrocyte network from left following RuBi-GABA (top) and RuBi-glutamate (bottom) uncaging. Yellow star = uncaging site, same for each NT. Colors denote change in active frame number/pixel (all AQUA-detected events 150s before and after uncaging; red = activity increase, blue = decrease; activity in the uncaged cell [dark grey] is excluded). (c) Top: Ca^{2+} activity from all recorded local astrocyte networks. Each row shows activity of one

Figure 3.3 continued on next page

Figure 3.3 continued

local network as the z-score of the mean $\Delta F/F$ from AQUA-detected events in the network. Mean $\Delta F/F$ and SD calculated using a baseline period 90–0s before uncaging. Networks sorted by onset time (first post-stim peak \geq threshold [mean baseline $\Delta F/F + 3$ SD]), with threshold calculated by trial). Red line = NT uncaging time. Greyed-out rows represent networks in which no events were detected outside of the uncaged cell. Bottom: binarized raster plots show each frame $\Delta F/F \geq$ threshold. Stacked bar graphs show proportion of local networks exhibiting an initial fluorescence increase following uncaging (responder). Responders defined as any network with ≥ 1 post-stim frame $\Delta F/F \geq$ threshold. WT (left) and Cx43^{floxed} slices (right). Fisher's exact test compares proportion of responders across conditions: $p = 0.62$ (GABA WT vs Cx43^{floxed}), $p = 0.78$ (glutamate WT vs Cx43^{floxed}), $p = 0.75$ (GABA WT vs glutamate WT). (d) Top: example binarized raster plot from C. Green line = response onset for each network (first post-stim frame \geq threshold). Bottom: Example local network, showing onset latency (green) as time between NT-uncaging and response onset, and post-onset frames \geq threshold (black tick marks). (e) One-way ANOVA compares the onset latency across conditions (WT, Cx43^{floxed}, and CBX). $p = 0.82$ (GABA), $p = 0.89$ (glutamate). (For e, f, Data shown by responding network, median, and 25th and 75th percentile. WT: $n = 21$ networks responding to GABA and 23 networks to glutamate; $n = 7$ slices, 4 mice; Cx43^{floxed}: $n = 42$ networks responding to GABA and 47 networks to glutamate; $n = 16$ slices, 8 mice; CBX: $n = 24$ networks responding to GABA and 24 networks to glutamate; $n = 8$ slices, 4 mice). (f) Persistence of network-level responses calculated as the proportion of post-onset frames \geq threshold. One-way ANOVA followed by Tukey-Kramer Test determine significant pairwise comparisons between conditions for each NT. GABA: $p = 0.0010$ (WT v Cx43^{floxed}), 0.025 (WT v CBX) and 0.72 (Cx43^{floxed} v CBX). Glutamate: $p = 0.00034$ (WT v Cx43^{floxed}), 0.0032 (WT v CBX) and 0.98 (Cx43^{floxed} v CBX). (g) Sholl-like analysis schematic. Grey concentric circles = 50 μ m bands. Yellow star = NT uncaging site. Inner radius of innermost band begins 25 μ m from uncaging, as events $<25\mu$ m from the uncaging site are likely to occur within stimulated astrocyte. Outer radius of outermost band is 175 μ m from uncaging, as $>175\mu$ m from the uncaging site can be outside the FOV; see Extended Data Fig. 3.3i. (h) Ca²⁺ event frequency change in the local network after GABA (top) and glutamate (bottom) uncaging. 90–0s before and 0–150s after uncaging used to calculate event number/30s. Permutation test used to determine significance. p -values for all timepoints and bands are in Extended Data Table 3.6. (i) Grid-based ROI (20 x 20 μ m) schematic. (j) Distribution of distances from uncaging site to center of ROIs active post-uncaging. Active ROIs are defined as any region with $\geq 50\%$ event frequency increase post-uncaging; see Extended Data Fig. 3.3j (GABA: $n = 195$ active ROIs; glutamate: $n = 171$ active ROIs from 27 paired FOVs). (k) Example FOV of ROIs with any baseline events (left) and active ROIs following uncaging (right). Yellow dot = NT uncaging site. (l) Fraction of ROIs active (*responding*) following both GABA and glutamate uncaging, among all active ROIs for uncaging of either NT (black vertical line; $8.27 \pm 1.34\%$, mean \pm sem; $n = 27$ paired FOVs). This overlap fraction is compared with a distribution of 10,000 surrogate overlap fractions obtained by choosing an equal number of active ROIs as observed in each FOV, but at random from among all ROIs with any baseline events for GABA and glutamate (grey distribution).

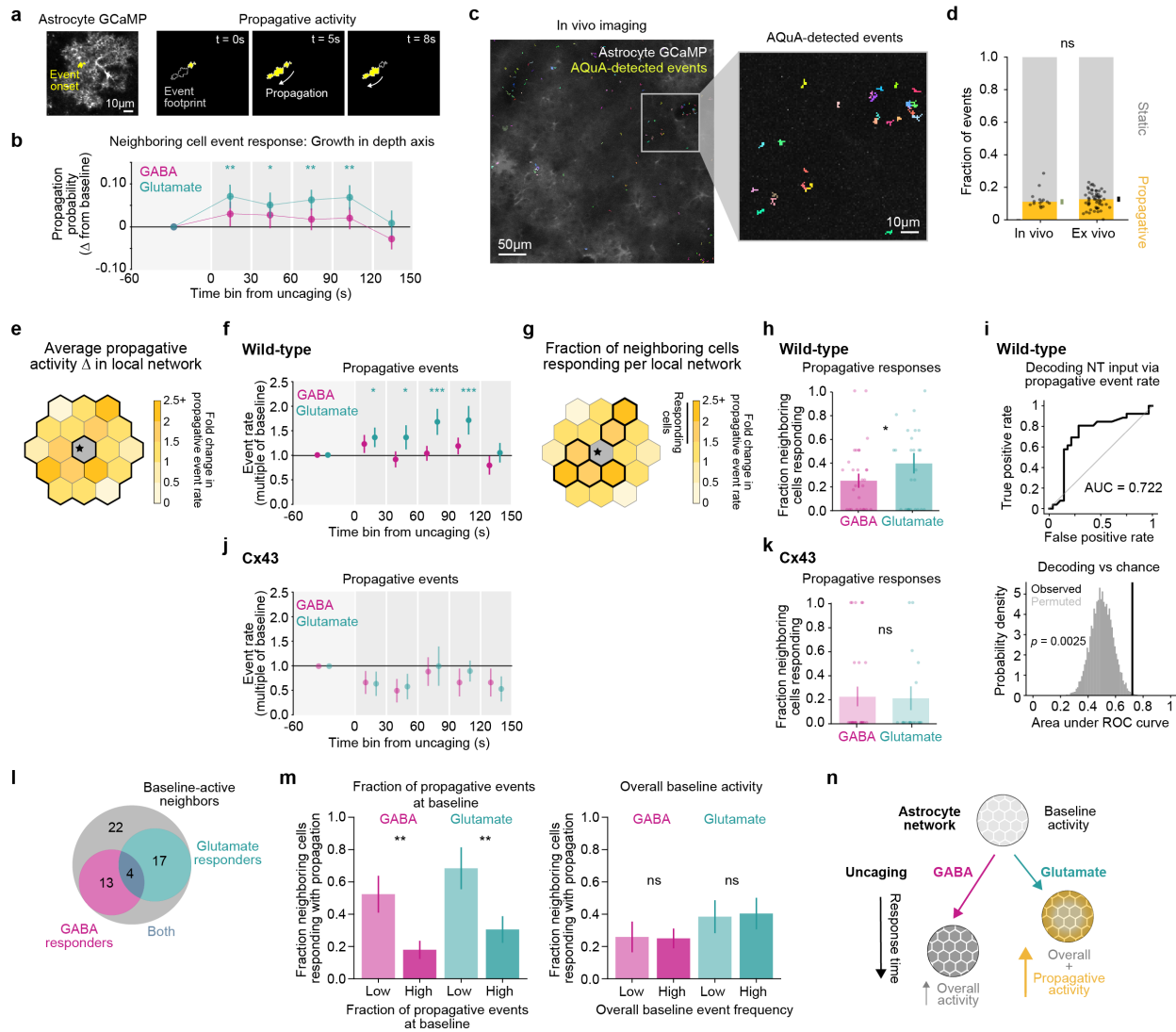


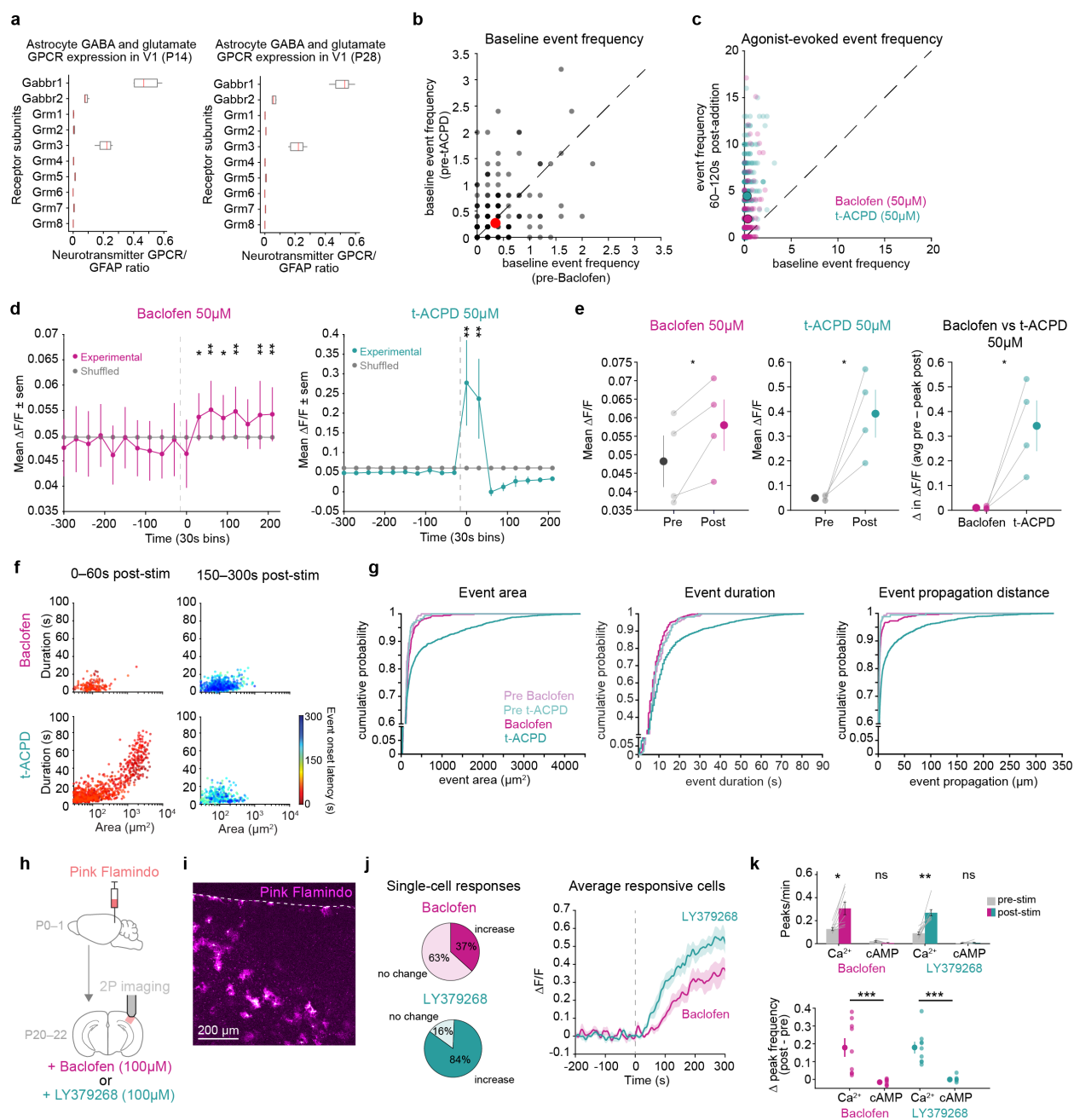
Figure 3.4. Propagative activity distinguishes astrocyte network responses to GABA and glutamate.

(a) GCaMP6f fluorescence in an individual astrocyte highlighting the initial territory of a propagating event (left). Trajectory of the propagative event over time (3 right panels). The total territory of the event (‘event footprint’) is outlined in grey. The territory of the event at each time point is shown in yellow. (b) Change in probability of a Ca^{2+} event growing in the depth-axis (toward or away from the pia) among all events from neighboring cells after GABA or glutamate uncaging, relative to 60–0s pre-uncaging. Data shown as overall probability \pm standard error determined from hierarchical bootstrapping (Methods; GABA: $n = 142$ cells in 28 FOV; glutamate: $n = 120$ cells in 27 FOV). Two-sided p - and q -values for changes versus baseline were obtained by circularly shifting each cell’s events in time (Methods; Extended Data Table 3.8). (c) *In vivo* 2P image showing expression of astrocyte GCaMP6f in V1. Colored overlay: all AQuA-detected Ca^{2+} events from a 90s stationary period from a 400 x 400 μ m FOV (left) and 100 x 100 μ m inset (right). (d) Fraction of astrocyte Ca^{2+} events that exhibit growth $>1\mu$ m in any direction (“propagative” events) observed in V1 during stationary wakefulness *in vivo*

Figure 3.4 continued on next page

Figure 3.4 continued

(left, markers are individual recordings) and at baseline in acute V1 slices (right, markers are individual FOV). Data shown as median across recordings \pm standard error via bootstrapping (*in vivo*: $n = 15$ recordings, 5 mice; *ex vivo*: $n = 55$ recordings, 4 mice). *In vivo* and *ex vivo* setting were compared with a two-sided rank-sum test ($p = 0.57$). (e) Analysis schematic illustrating average propagative activity change across all neighboring cells in the local network, as in f & j. Note heterogeneity of responses of individual neighboring cells averaged over in f & j. As in Fig. 3.3, activity from the directly stimulated astrocyte is excluded from all analyses in this figure. (f, j) Fold-change in rate of propagative Ca^{2+} events among neighboring cells after GABA or glutamate uncaging in acute slices from WT mice (f) or Cx43^{flox^{ed}} mice (j), relative to 60–0s pre-uncaging. Data shown as median across FOVs \pm standard error via hierarchical bootstrapping (Methods; n for all conditions are in Extended Data Table 3.9). One-sided p - and q -values were obtained via circular permutation testing (Methods; Extended Data Table 3.10). (g) Analysis schematic illustrating the fraction of neighboring cells per FOV that respond to NT with increases in propagative activity, as in h & k. Note that a subset of neighboring cells in the local network exhibit activity changes following NT uncaging. (h, k) Fraction of neighboring cells per FOV with $\geq 50\%$ increase propagative Ca^{2+} events (“responding”) after GABA or glutamate uncaging in WT (h) or Cx43^{flox^{ed}} slices (k). Data shown as mean \pm sem via hierarchical bootstrapping; dots denote individual FOVs (see Methods; n for all conditions are in Extended Data Table 3.9). Permutation testing was used to compare fraction of cells responding to GABA and glutamate in WT slices ($p = 0.046$) and Cx43^{flox^{ed}} slices ($p = 1.0$). (i) Top: Receiver operating characteristic (ROC) curve of decoding NT identity by thresholding the relative change in propagative event rate from 60–0s pre-uncaging to 0–120s post-uncaging across all neighboring cells in a FOV indicates that propagative events reliably distinguish NT input in WT slices. Bottom: Observed area under the ROC curve = 0.72 ± 0.077 (value \pm bootstrapped standard error), compared to a permuted distribution *via* permuting NT labels ($p = 0.0025$, $n = 55$ FOVs). Feature values \geq threshold were classified as glutamate, and values $<$ threshold as GABA. (l) Number of neighboring cells responding to one or both NTs with propagative activity increases, among cells with baseline propagative activity ($n = 56$ cells, 24 paired recordings, 7 slices, 4 mice). Permutation testing measures of correlation (Spearman rho, $p = 0.24$) or overlap (Jaccard index, $p = 0.96$) between GABA and glutamate responses does not reject the null hypothesis of independent responses. (m) Fraction of neighboring cells per FOV with $\geq 50\%$ increase in propagative Ca^{2+} events (“responding”) after GABA or glutamate uncaging in WT slices, split between cells with fraction of propagative events at baseline (left) or overall baseline event rates (right) in the bottom 50% (“Low”, light bars) or top 50% (“High”, dark bars) across all cells (see Extended Data Fig. 3.5e). Data shown as mean \pm sem via hierarchical bootstrapping (n in Extended Data Table 3.11). Response fractions for cells with “Low” and “High” baseline fractions were compared by permuting cells’ baseline propagation fractions for GABA ($p = 0.0022$) and glutamate ($p = 0.0059$); responses for cells with “Low” and “High” overall baseline event rates were compared similarly (GABA: $p = 1.0$; glutamate: $p = 1.0$). (n) Integrated model of astrocyte network response to GABA and glutamate from data in Fig. 3.3–4. Astrocyte networks increase general Ca^{2+} activity in response to both NTs, and propagative activity increases specifically in response to glutamate. Network responses to glutamate occur soon after stimulation, while responses to GABA are delayed. For b & f: *: $q < 0.05$, **: $q < 0.01$, ***: $q < 0.001$. For h & m: *: $p < 0.05$, **: $p < 0.01$.



Extended Data Figure 3.1: Different responses to activation of astrocytic glutamatergic and GABAergic receptors via pharmacological bath-application.

(a) Ribosomal-mRNA expression in visual cortex astrocytes of P14 ($n = 4$ biological replicates) and P28 ($n = 5$ biological replicates) mice from the Farhy-Tselnicker et. al. publicly available dataset (NCBI Gene Expression Omnibus, GSE161398). Visual cortex astrocytes show expression of GABA_B receptors and mGluR₃, but low expression of all other mGluRs, including mGluR₅ (ref. ¹⁹). Similar expression levels are found in the Srinivasan et. al. dataset available at <http://astrocytarnaseq.org/>. Ratio of FPKM for the gene of interest / FPKM for GFAP were calculated to normalize for potential differences in the sequencing depth of replicates.

Extended Data Figure 3.1 continued on next page

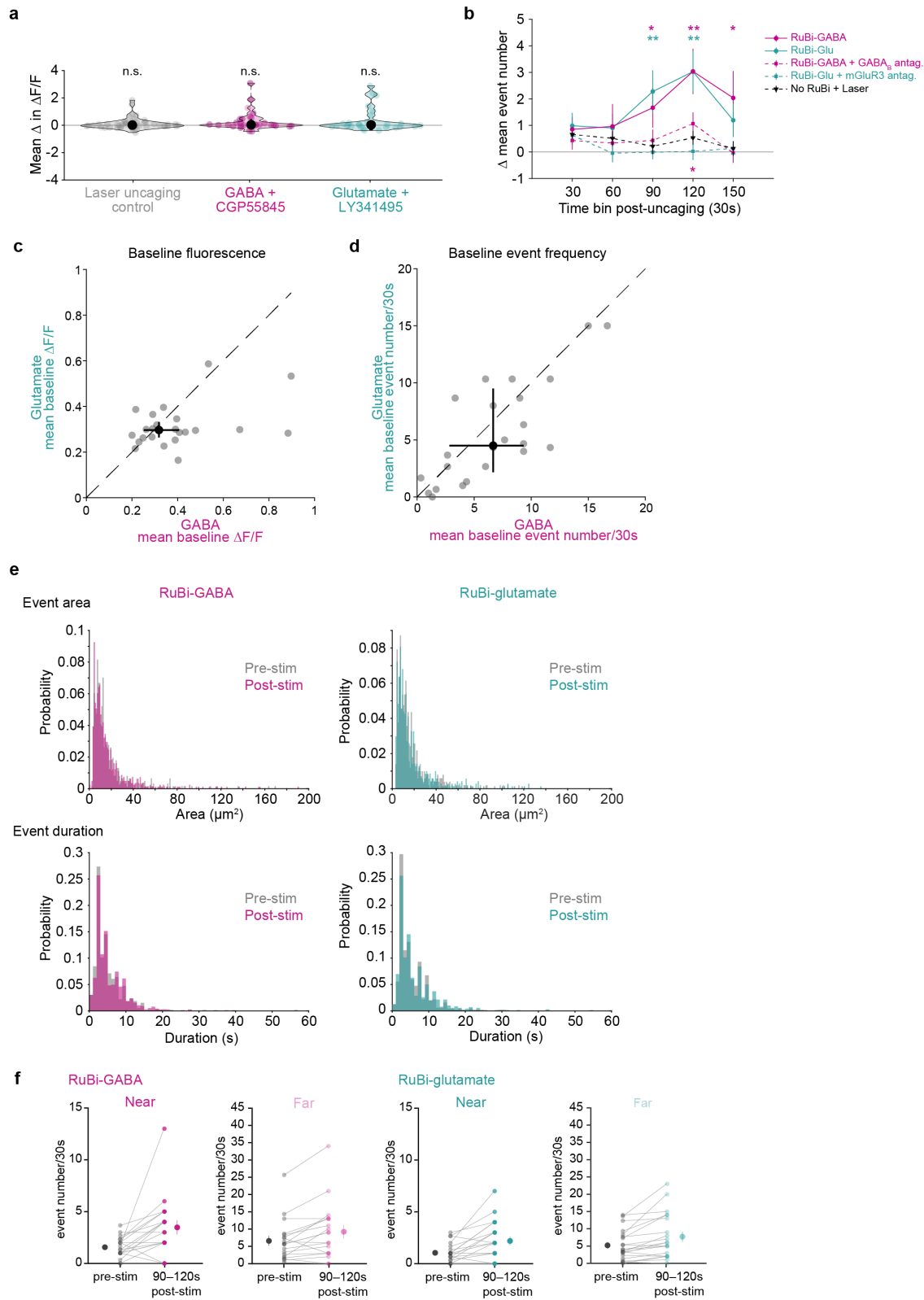
Extended Data Figure 3.1 continued

(b) Baseline event frequency for each active astrocyte prior to bath application of baclofen (50 μ M, x-axis) and t-ACPD (50 μ M, y-axis). Data shown by astrocyte (grey dots, from $n = 4$ slices) and mean (red dot). Dashed line = unity line. Baseline event frequencies prior to baclofen and t-ACPD application were compared for each astrocyte using a paired two-sided t-test ($p = 0.14$). **(c)** Event frequency for each active astrocyte 300–0s before and 60–120s after addition of agonist (50 μ M). Data shown by astrocyte (light dots, from $n = 4$ slices) and mean (solid dots) for baclofen (pink) and t-ACPD (green). Dashed line = unity line; all astrocytes above the unity line display increased activity in presence of agonist. For b & c, 300–0s before addition of agonist was used to calculate mean baseline event frequency (events/60s) per astrocyte; an active astrocyte is any cell with ≥ 1 AQuA-detected event. Note the difference in axes between graphs in b & c, reflecting the low baseline event frequency for all astrocytes. **(d)** Time-series traces of average $\Delta F/F$ in 30 s windows from active cells in each slice. 300–0s before and 0–240s after bath-application of agonist used to calculate event average $\Delta F/F$ /30s. Data shown as mean \pm sem ($n = 4$ slices, 4 mice stimulated with 50 μ M agonist). Permutation test used to determine significance. p -values for all timepoints are in Extended Data Table 3.3. All traces are aligned to 0s, the frame of agonist entry into the imaging chamber. $\Delta F/F$ values were calculated using a moving 10s baseline window, averaging the lower 50% of values in the window. Active cells were cells with ≥ 1 AQuA event detected in either the baclofen or t-ACPD recording. **(e)** Left and center: Average $\Delta F/F$ before and after bath-application of baclofen (50 μ M, left) and t-ACPD (50 μ M, center). $\Delta F/F$ after bath-application of agonist is from the 30 s time window with the highest average $\Delta F/F$ for each slice (“peak post”). Right: Change in average $\Delta F/F$ after bath-application of agonist. Data shown as slices (light dots and grey lines, $n = 4$ slices, 4 mice) and mean \pm sem (dark dots and error bars). Paired t-test compares conditions. Baclofen: $p = 0.046$, t-ACPD: $p = 0.031$ and Δ in $\Delta F/F$: $p = 0.033$. **(f)** Scatter plots of the area and duration of individual Ca^{2+} events 0–60 s (left) and 150–300 s (right) after bath-application of baclofen (top) or t-ACPD (bottom). Separating events into these two time-windows highlights events occurring early that are covered in Fig. 3.1d by those with longer onset latencies. Events following bath-application of agonists color-coded by onset time. Dots represent individual Ca^{2+} events from $n = 4$ slices stimulated with 50 μ M agonist. Note: these are the same data, with the same onset latency color scale, as shown in Fig. 3.1d, bottom. **(g)** Distributions of event area, duration and propagation 120–0s before (“Pre”) or 0–120s after addition of baclofen (50 μ M) or t-ACPD (50 μ M). One-way ANOVA followed by Tukey-Kramer Test determine significant pairwise comparisons between conditions. p -values for all conditions and features are in Extended Data Table 3.4. Note that, for all features, pre-baclofen, pre-tACPD, and baclofen events are not significantly different from one another. Only events following addition of t-ACPD show a rightward shift for all features. **(h)** Experimental strategy for Pink Flamindo expression and 2P imaging of astrocytic cAMP in acute cortical slices. **(i)** Representative Pink Flamindo fluorescence in V1 FOV; dotted line denotes pia. **(j)** Left: Percent of total astrocytes that increase fluorescence or show no change with bath-application of baclofen (top, pink) or mGluR₃-specific agonist LY379268 (bottom, green) ($n = 147$ astrocytes) in the presence of TTX and CBX. Right: Average $\Delta F/F$ trace only from responsive cells in each slice (mean \pm sem across slices from $n = 54$ responsive astrocytes (baclofen) and 123 responsive astrocytes (LY379268) from $n = 8$ slices, 3 mice).

Extended Data Figure 3.1 continued on next page

Extended Data Figure 3.1 continued

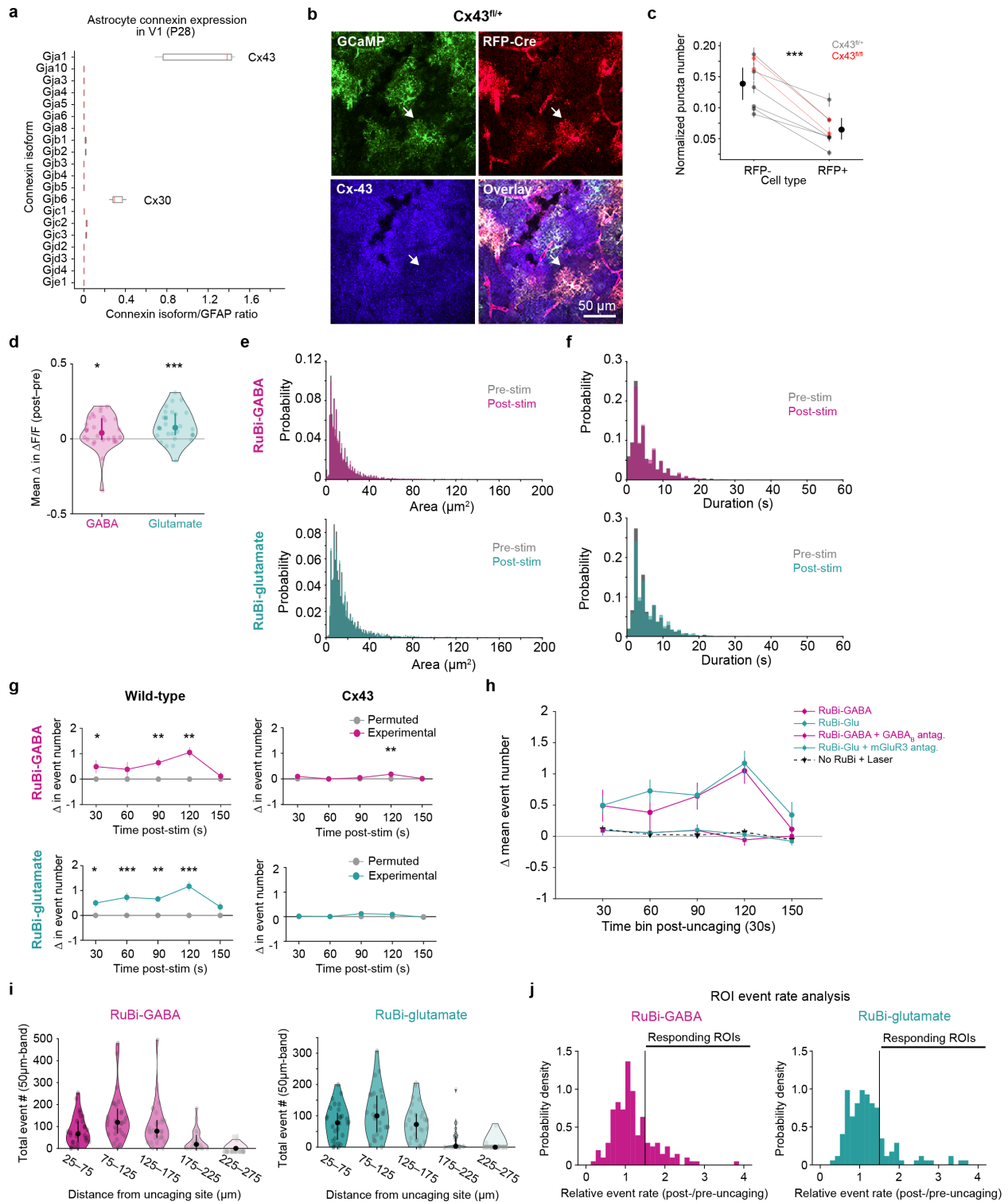
To capture steady-state changes, $\Delta F/F$ values were calculated using raw – background fluorescence and a fixed baseline window (frames 1–100), then lowpass filtered at 0.01Hz. **(k)** Top: Average Ca^{2+} or cAMP peaks/minute/astrocyte before and after bath-application of baclofen (pink) or LY379268 (green). Data shown as slices (grey lines) and corresponding mean \pm sem. Paired t-test compares pre- and post-agonist values for each condition. *p*-values corrected for multiple comparisons using Bonferroni-Holm correction $\text{FWER} \leq 0.05$. Baclofen: *p* = 0.019 (Ca^{2+}) and 0.057 (cAMP). LY379268: *p* = 0.0017 (Ca^{2+}) and 0.66 (cAMP). Bottom: Average change in Ca^{2+} or cAMP peaks/minute following bath-application of baclofen (pink) or LY379268 (green). Data shown by slice (light dots) and corresponding mean \pm sem (dark dots and error bars). Rank sum tests compare Ca^{2+} and cAMP frequency changes for each agonist. *p* = 0.000082 (baclofen) and 0.000082 (LY379268). Cyto-GCaMP: *n* = 809 active astrocytes (baclofen) and 1033 active astrocytes (LY379268) from *n* = 9 slices, 3 mice. Pink Flamingo: *n* = 147 astrocytes, 8 slices, 3 mice. To detect transient fluctuations, $\Delta F/F$ was calculated using a moving 10s baseline window, with peaks determined for each astrocyte if $\Delta F/F \geq 3\text{SD}$ above mean baseline $\Delta F/F$.



Extended Data Figure 3.2: Characterization of, and controls for, increased Ca^{2+} activity in astrocytes directly stimulated by NT uncaging.
Extended Data Figure 3.2 continued on next page

Extended Data Figure 3.2 continued

(a) Average change in $\Delta F/F$ with laser uncaging control (laser stimulation without RuBi, grey, $n = 46$ astrocytes, 9 slices, 3 mice) and with uncaging in the presence of antagonist (RuBi-GABA + GABA_BR antagonist [magenta, $n = 28$ astrocytes, 8 slices, 5 mice] or RuBi-glutamate + mGluR_{2/3} antagonist [green, $n = 28$ astrocytes, 7 slices, 4 mice]). GABA_BR antagonized using CGP55845, a potent and selective GABA_BR antagonist, and mGluR₃ antagonized using LY341495, a potent mGluR_{2/3} antagonist also known to antagonize other mGluR subtypes at higher concentrations⁷¹. Data shown by astrocyte, median, 25th and 75th percentile. Wilcoxon signed-rank test compares change from baseline. p -values corrected for multiple comparisons using Bonferroni-Holm correction with FWER ≤ 0.05 . Laser uncaging control: $p = 0.50$, RuBi-GABA + CGP55845: $p = 0.11$ and RuBi-glutamate + LY341495: $p = 0.41$. **(b)** Event frequency change after NT uncaging (GABA: solid magenta lines, $n = 27$ astrocytes, 7 slices, 4 mice; glutamate: solid green lines, $n = 24$ astrocytes, 7 slices, 4 mice), NT uncaging in the presence of antagonist (dotted magenta and green lines), and laser uncaging control (dotted black line). 90–0s before and 0–150s after uncaging used to calculate event number/30s. Data shown by mean \pm sem. Permutation test used to determine significance. p -values for all conditions and timepoints are in Extended Data Table 3.5. **(c)** Baseline fluorescence prior to GABA and glutamate uncaging. 90–0s before uncaging used to calculate mean $\Delta F/F$ per cell. Data shown by cell (grey dots, $n = 24$ astrocytes), median, and 25th and 75th percentile (black dots and crosshairs). Dashed line = unity line. Wilcoxon signed-rank test shows no significant difference between baseline fluorescence of directly stimulated astrocytes prior to GABA and glutamate uncaging ($p = 0.089$). **(d)** Baseline event frequency prior to GABA and glutamate uncaging. 90–0s before uncaging used to calculate mean number of events/30s for each cell. Data shown by cell (grey dots, $n = 24$ astrocytes), median and 25th and 75th percentile (black dots and crosshairs). Dashed line = unity line. Wilcoxon signed-rank test shows no significant difference between baseline event frequency of directly stimulated astrocytes prior to GABA and glutamate uncaging ($p = 0.068$). **(e)** Distribution of event area and duration pre- and post-uncaging of RuBi-GABA (left) and RuBi-glutamate (right) from “responder” uncaging cells. Detected events 120 s pre- and post-uncaging are included from $n = 19$ astrocytes, 7 slice, 4 mice (GABA) and $n = 21$ astrocytes, 7 slices, 4 mice (glutamate). Rank-sum test compares pre- and post-uncaging event features. Area: $p = 0.58$ (GABA) and 0.95 (glutamate). Duration: $p = 0.083$ (GABA) and 0.13 (glutamate). **(f)** Event frequency in responding astrocytes directly stimulated with NT. Events from directly stimulated astrocytes were separated into events near and far from GABA and glutamate uncaging. 90–0s before used to calculate average event number/30s (“pre-stim”). Data shown by cell (light dots and grey lines) and mean \pm sem (dark dots and error bars).

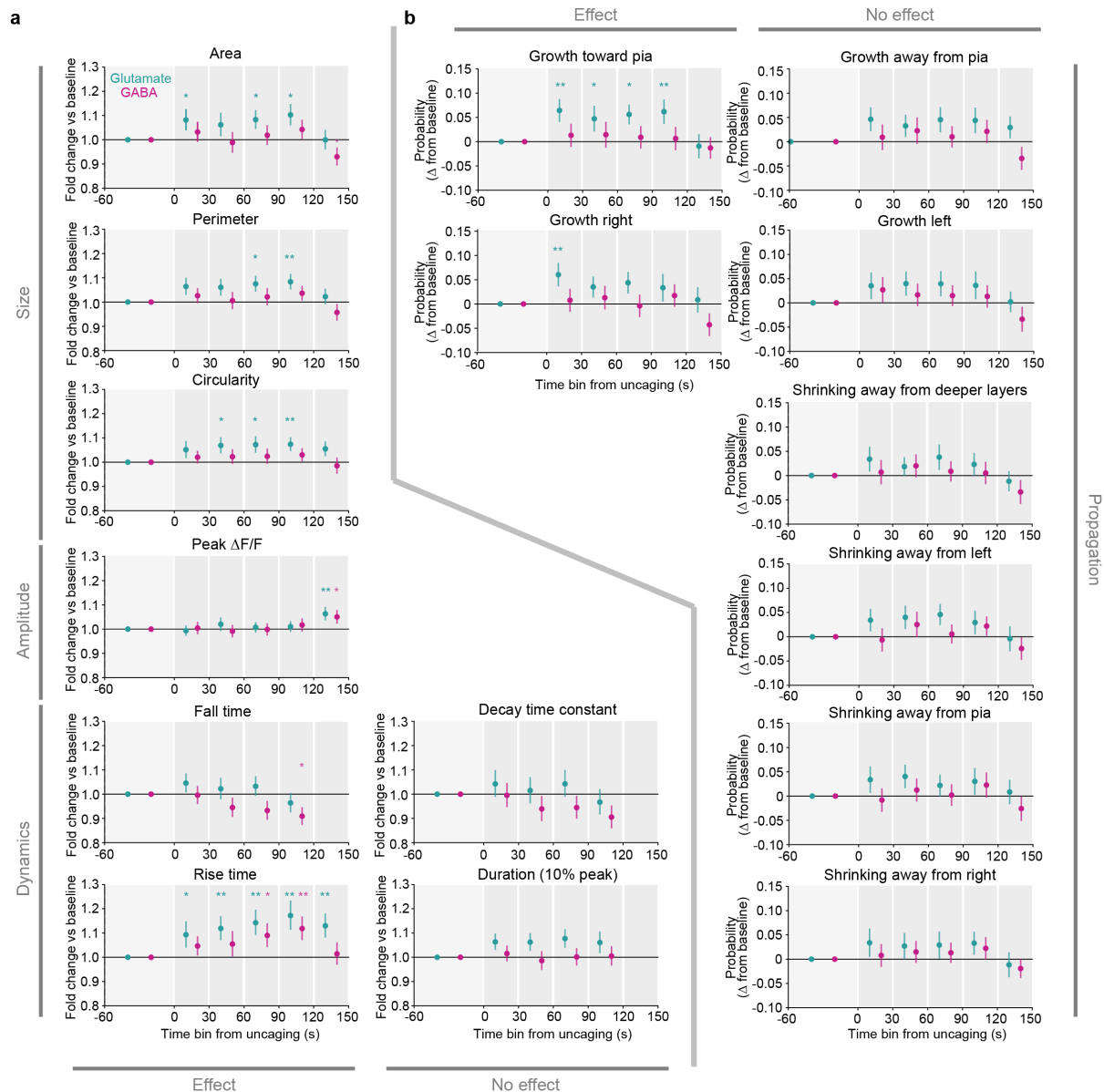


Extended Data Figure 3.3: Confirmation of Cx43 knockdown and network-level controls after NT uncaging.

Extended Data Figure 3.3 continued on next page

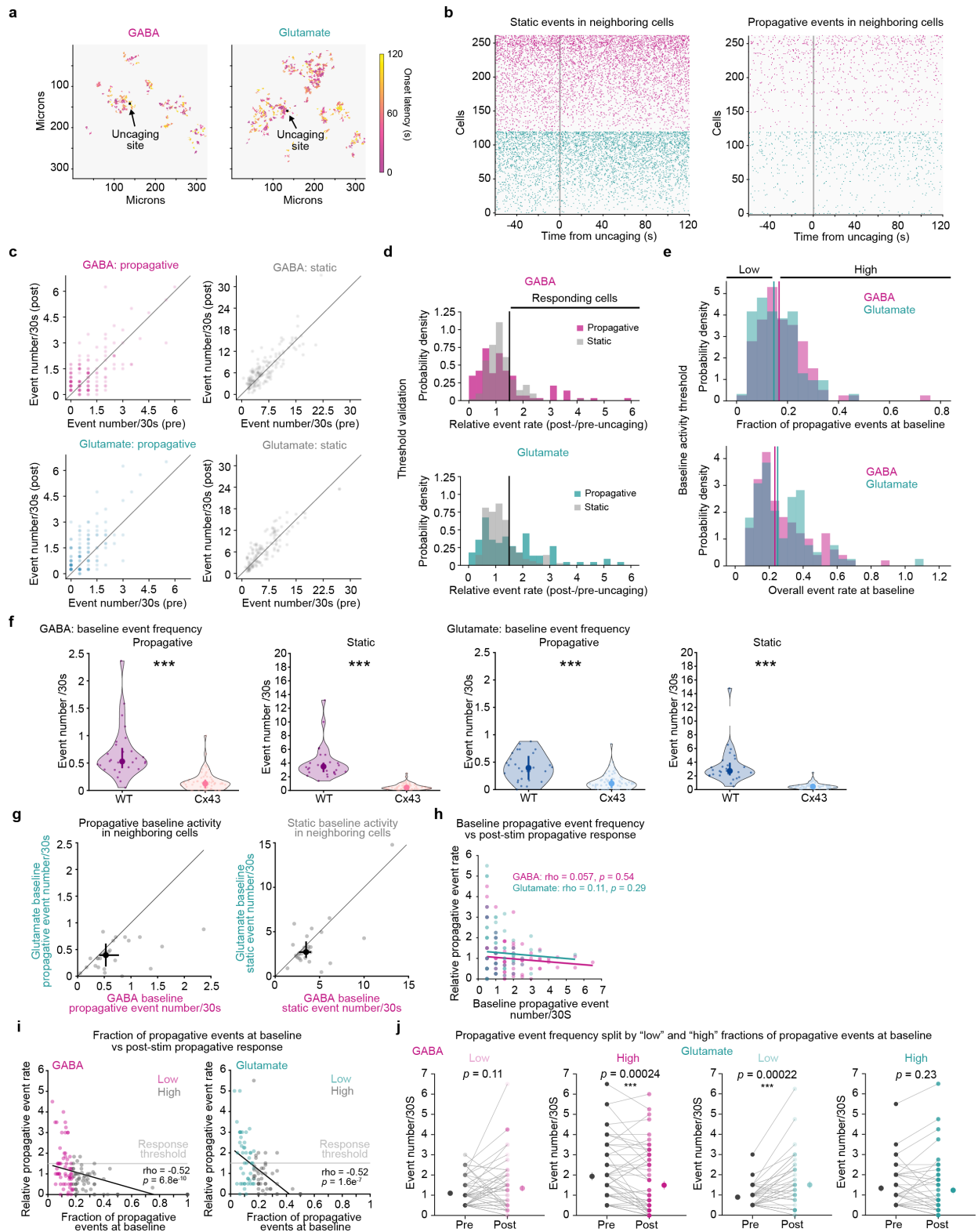
Extended Data Figure 3.3 continued

(a) Ribosomal-mRNA expression in visual cortex astrocytes of P28 mice ($n = 5$ biological replicates) from the Farhy-Tselnicker et. al. publicly available dataset (NCBI Gene Expression Omnibus, GSE161398). Visual cortex astrocytes preferentially express Cx43 (*Gja1*) over other connexins, including Cx30 (*Gjb6*). Similar expression levels are found in the Srinivasan et. al. dataset available at <http://astrocytarnaseq.org>. Ratio of FPKM for the gene of interest / FPKM for GFAP were calculated to normalize for potential differences in the sequencing depth of replicates. **(b)** Representative micrographs of immunohistochemistry in a Cx43^{fl/+} slice demonstrating reduced numbers of Cx43 puncta in Cre⁺ astrocytes. White arrow points to individual cell expressing GCaMP (green) and RFP-Cre (red), with reduced Cx43 (blue). **(c)** Average Cx43 puncta/astrocyte in RFP-Cre⁻ and RFP-Cre⁺ astrocytes; puncta counts are normalized by area of each astrocyte. Data are shown by mouse averages (light dots, error bars and connecting lines, grey = Cx43^{fl/+} and red = Cx43^{fl/fl} mice) and mean \pm sem (dark dots and error bars). Cx43 puncta counts were similar for Cx43^{fl/+} and Cx43^{fl/fl} mice; data from both genotypes were pooled together for all analyses and referred to as Cx43^{fl/oxed}. Paired two-sided *t*-test compares average Cx43 puncta counts in RFP-Cre⁻ and RFP-Cre⁺ astrocytes. $p = 0.00013$. **(d)** Average change in $\Delta F/F$ in WT astrocyte networks after RuBi-GABA (magenta) and RuBi-glutamate (green) uncaging. Data shown by trial/FOV, median and 25th and 75th percentile. (For d–i, WT: $n = 28$ networks, 7 slices, 4 mice). Wilcoxon signed-rank test compares change from baseline. $p = 0.016$ (GABA) and 0.00032 (glutamate). **(e,f)** Distribution of event area and duration pre- and post-uncaging of RuBi-GABA (top) and RuBi-glutamate (bottom). Detected events 120 s pre- and post-uncaging are included. Rank-sum test compares pre- and post-uncaging event features. Area: $p = 0.025$ (GABA) and 0.0050 (glutamate). Duration: $p = 0.063$ (GABA) and 0.0000045 (glutamate). **(g,h)** Event frequency change in neighboring astrocytes after GABA (g, top) and glutamate (g, bottom) uncaging in WT and Cx43^{fl/oxed} slices ($n = 61$ networks, 16 slices, 8 mice). WT data from g replotted in h (circular markers) with laser uncaging control (laser stimulation without RuBis, dotted black line and triangular markers, $n = 48$ networks, 9 slices, 3 mice) and with uncaging in the presence of antagonist (RuBi-GABA + GABA_BR antagonist [magenta line and square markers, $n = 32$ networks, 8 slices, 5 mice] or RuBi-glutamate + mGluR_{2/3} antagonist [green line and square markers, $n = 28$ networks, 7 slices, 4 mice]). 90–0s before and 0–150s after uncaging used to calculate event number/30s in neighboring astrocytes with ≥ 1 AQUA-detected event. Data shown by mean \pm sem. Permutation test used to determine significance. *p*-values for all conditions and timepoints are in Extended Data Table 3.7. **(i)** Total number of AQUA-detected events in 50 μ m bands radiating out from the uncaging site. All events 90s before and 150s after NT uncaging are included. Data shown by trial/FOV, median and 25th and 75th percentile. **(j)** Distribution of relative event rates from 20x20 μ m ROIs following uncaging of RuBi-GABA (left) and RuBi-glutamate (right). Validation for threshold used to define ROIs with increased activity post-uncaging; chosen threshold: $\geq 50\%$ event frequency increase post-uncaging.



Extended Data Figure 3.4: Change in individual astrocyte Ca^{2+} event features post NT-uncaging.

(a) Fold change in indicated Ca^{2+} event features among all events from all neighboring cells after GABA or glutamate uncaging, relative to 60–0s pre-uncaging. Data shown as overall fold change \pm standard error determined from hierarchical bootstrapping (Methods; GABA: $n = 142$ cells in 28 FOV; glutamate: $n = 120$ cells in 27 FOV). Two-sided p - and q -values for changes versus baseline were obtained by circularly shifting each cell’s events in time (see Methods; Extended Data Table 3.12). **(b)** Change in the probability of a Ca^{2+} event growing or shrinking in the indicated direction among all events from neighboring cells after GABA or glutamate uncaging, relative to 60–0s pre-uncaging. Data shown as overall probability \pm standard error determined from hierarchical bootstrapping (Methods; GABA: $n = 142$ cells in 28 FOV; glutamate: $n = 120$ cells in 27 FOV). Two-sided p - and q -values for changes versus baseline were obtained by circularly shifting each cell’s events in time (see Methods; Extended Data Table 3.13).



Extended Data Figure 3.5: Validating changes in propagative event activity following NT-uncaging.

Extended Data Figure 3.5 continued on next page

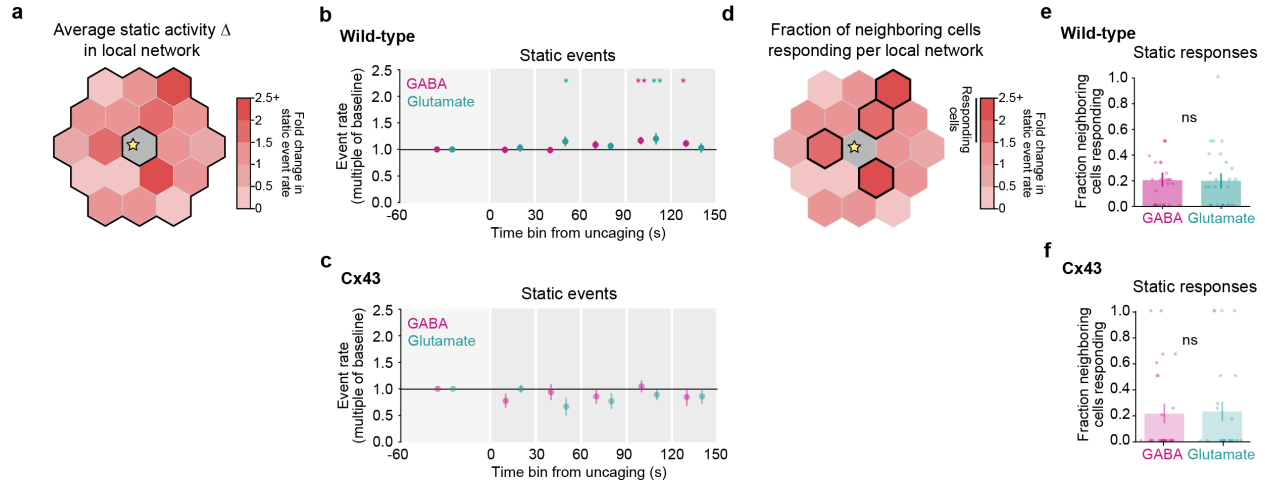
Extended Data Figure 3.5 continued

(a) Representative spatial maps of Ca^{2+} events in the same astrocyte network 0–120 s after either GABA (left) or glutamate (right) uncaging. Events are color-coded by onset time. Black dot = NT uncaging site. Events from all time-points are distributed throughout the imaging field. There is no visible wavefront of activity traveling across the imaging field or emanating from the uncaging site. Note that all panels except for (f) are data from WT slices. **(b)** Raster plots of Ca^{2+} event onsets for static (left) or propagative (right) events before and after GABA (magenta) or glutamate (green) uncaging. Raster plots show all neighboring cells (astrocytes not directly stimulated by NT-uncaging) from all FOVs, with each row showing events from an individual astrocyte. Within each NT and event type, cells were sorted by the overall rate of static events from 0–120s post-uncaging (*i.e.*, the same sorting was used for the left and right raster plots). Grey line = NT uncaging start. **(c)** Scatter plots of event rates (event number/30s) within neighboring cells during the period 60–0s pre-uncaging (*x*-axis) versus 0–120s post-uncaging (*y*-axis). Rates of propagative (left) and static (right) events are shown for recordings of GABA (top) and glutamate (bottom) uncaging. Dots are individual neighboring cells; darker dots indicate multiple overlapping cells. **(d)** Distribution of post-/pre-uncaging ratio of static (grey) or propagative (color) event rates among neighboring cells with any baseline events of the corresponding type, after GABA (magenta, top) or glutamate (green, bottom) uncaging. Ratios computed per-cell as the rate from 0–120s post-uncaging divided by the rate from 60–0s pre-uncaging. Vertical black lines indicate the threshold used to determine “responding” cells in Fig. 3.4h, l, m and Extended Data Fig. 3.6e (*i.e.*, ≥ 1.5 -fold). **(e)** Top: Distribution of the fraction of events during the baseline window (60–0s pre-uncaging) that were propagative in each neighboring cell before GABA (magenta) or glutamate (green) uncaging, among those cells that had any baseline propagative activity. Vertical magenta and green lines indicate the thresholds (50th percentile) for recordings of GABA and glutamate uncaging, respectively, used in Fig. 3.4m left to delineate “Low” and “High” fraction of propagative events at baseline among neighboring cells. Bottom: Distribution of the overall event rate during the baseline window of 60–0s pre- GABA (magenta) or glutamate (green) uncaging, in each neighboring cell that had baseline propagative activity. Vertical magenta and green lines indicate the thresholds (50th percentile) for recordings of GABA and glutamate uncaging, respectively, used in Fig. 3.4m right to delineate cells with “Low” and “High” overall event rates at baseline. **(f)** Baseline propagative (left) and static (right) event frequencies of astrocytes in WT or Cx43^{flxed} slices. Baseline period: 90–0s prior to uncaging. Individual data points show average event rate from active neighboring astrocytes (≥ 1 AQuA-detected event during recording) for each FOV. Data shown by FOV (WT: $n = 28$ FOV for GABA and glutamate, 7 slices, 4 mice; Cx43^{flxed}: $n = 63$ FOV for GABA and 61 FOV for glutamate, 16 slices, 8 mice), median, 25th and 75th percentile. Wilcoxon rank sum test compares WT and Cx43^{flxed} baseline event frequencies (GABA: $p = 1.6\text{e-}10$ [propagative], $7.7\text{e-}14$ [static]; glutamate: $p = 9.0\text{e-}7$ [propagative], $1.1\text{e-}12$ [static]). **(g)** Baseline propagative (left) and static (right) event frequencies in WT networks prior to GABA and glutamate uncaging. 90–0s before uncaging used to calculate mean number of events/30s. Event rate per FOV calculated by averaging the event rates of active astrocytes in the FOV (≥ 1 AQuA-detected event during the recording), excluding the uncaging astrocyte. Data shown by FOV (grey dots, $n = 28$), median, 25th and 75th percentile (black dot and crosshairs).

Extended Data Figure 3.5 continued on next page

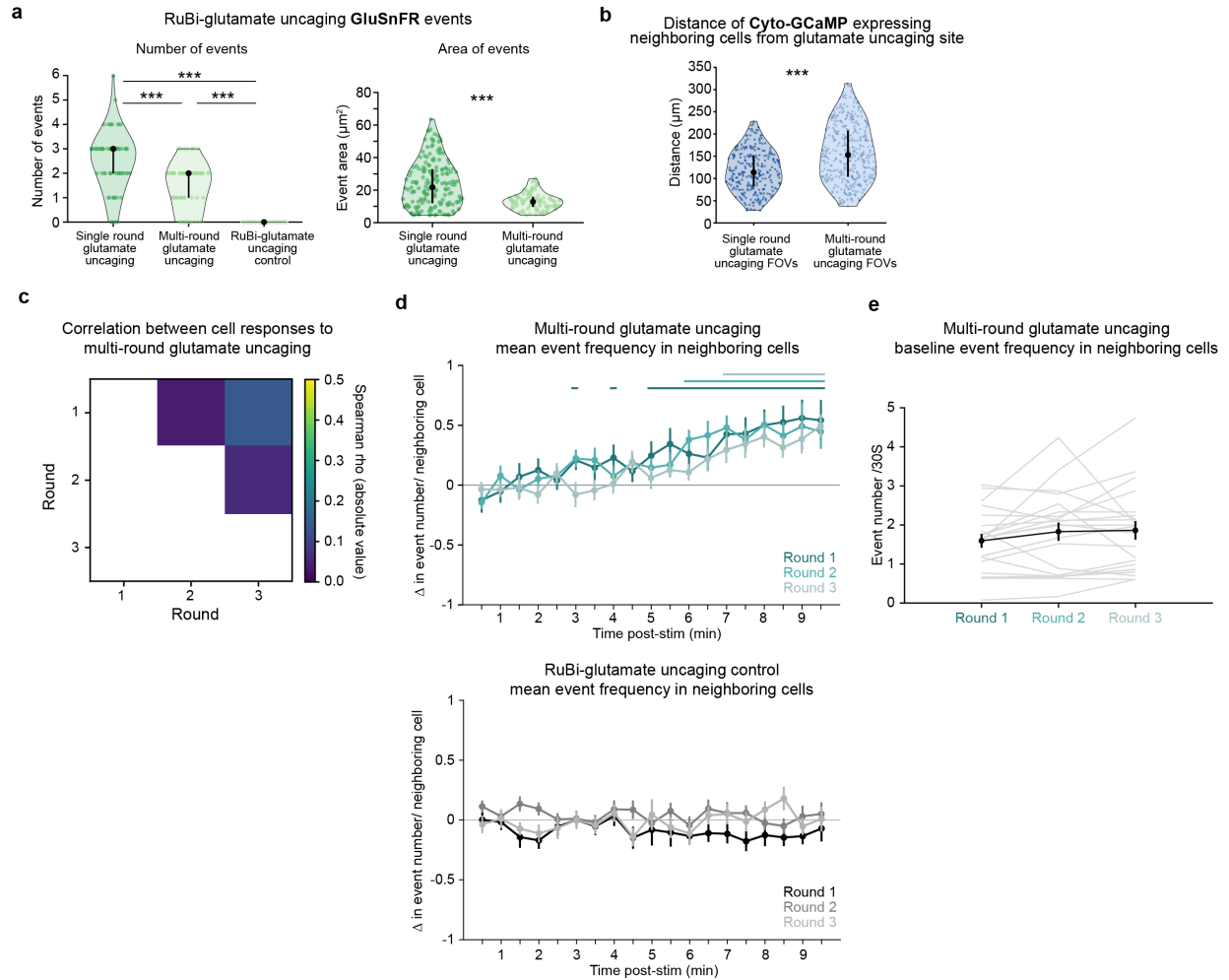
Extended Data Figure 3.5 continued

Wilcoxon signed-rank test compares baseline event frequencies prior to GABA and glutamate uncaging ($p = 0.00022$ [propagative] and 0.052 [static]). **(h)** Spearman correlation between baseline propagative event rate and relative post-stim propagative event rate for neighboring cells in GABA (magenta) and glutamate (turquoise) recordings. Data shown by individual neighboring astrocyte (for h–i, $n = 121$ cells [GABA], 91 cells [glutamate] with ≥ 1 baseline propagative event). For h–i, 60–0s before uncaging used for baseline window and relative post-stim propagative rate calculated as in d. **(i)** Spearman correlation between fraction of propagative events at baseline and relative post-stim propagative event rate for neighboring cells in GABA (left) and glutamate (right) recordings. Data shown by individual neighboring astrocyte color-coded by baseline activity composition category (“low” in magenta or turquoise, “high” in grey). Light grey horizontal line = response threshold (responders ≥ 1.5 -fold increase in propagative activity from baseline). Note a majority of astrocytes responding to either NT (at or above the response threshold line) display a low fraction of propagative events at baseline. **(j)** Propagative event frequency pre- and post-uncaging for neighboring cells with “low” and “high” fractions of propagative events at baseline (as for Fig. 3.4m, left). 60–0s before (“Pre”) and 0–120s after (“Post”) used to calculate average event number/30s. Data shown by cell (light dots and grey lines; $n = 61$ cells [GABA “low”], 60 cells [GABA “high”], 46 cells [glutamate “low”], 45 cells [glutamate “high”]) and mean \pm sem (dark dots and error bars). Wilcoxon signed-rank test compare pre-and post-stim frequencies for each category.



Extended Data Figure 3.6: Static activity changes in the local astrocyte network are similar in response to GABA and glutamate.

(a) Analysis schematic illustrating average static activity change across all neighboring cells in the local network, as reported in b and c. Heterogeneous responses of individual neighboring cells are averaged in b and c. (b–c) Fold-change in rate of static Ca^{2+} events among neighboring cells after GABA or glutamate uncaging in acute slices from WT mice (b) or Cx43^{flox^{ed}} mice (c), relative to 60–0s pre-uncaging. Data shown as median across FOVs \pm standard error via hierarchical bootstrapping (Methods; *n* for all conditions are in Extended Data Table 3.9). One-sided *p*- and *q*-values were obtained via circular permutation testing (Methods; Extended Data Table 3.10); *: *q* < 0.05, **: *q* < 0.01. (d) Analysis schematic illustrating the fraction of neighboring cells per FOV that respond to NT with increases in static activity, as reported in e and f. Note that a subset of neighboring cells in the local network exhibit activity changes following NT uncaging. (e–f) Fraction of neighboring cells per FOV with $\geq 50\%$ increase in static Ca^{2+} events (*responding*) after GABA or glutamate uncaging in WT (e) or Cx43^{flox^{ed}} slices (f). Data shown as mean \pm sem via hierarchical bootstrapping; dots denote individual FOVs (see Methods; *n* for all conditions are in Extended Data Table 3.9). Permutation testing was used to compare fraction of cells responding to GABA and glutamate in WT slices (*p* = 1.0) and Cx43^{flox^{ed}} slices (static: *p* = 1.0).



Extended Data Figure 3.7: Individual neighboring astrocytes exhibit variable Ca^{2+} responses across multiple rounds of glutamate uncaging.

(a) GluSnFR event features after RuBi-glutamate uncaging for three types of uncaging datasets. For number of events/uncaging site (left), data shown by uncaging trial, median, 25th and 75th percentile. For GluSnFR event area (right), data shown by GluSnFR event, median, 25th and 75th percentile (single round glutamate uncaging: $n = 72$ trials, 12 recordings, 4 slices, 2 mice; multi-round glutamate uncaging: $n = 66$ trials, 11 recordings, 2 slices, 1 mouse; RuBi-glutamate uncaging control: $n = 66$ trials, 11 recordings, 2 slices, 1 mouse). For number of events, one-way ANOVA followed by Tukey-Kramer Test determine significant pairwise comparisons between laser stimulation conditions. $p = 9.7\text{e-}10$ (single round glutamate uncaging v multi-round glutamate uncaging), $9.6\text{e-}10$ (single round glutamate uncaging v RuBi-glutamate uncaging control) and $9.6\text{e-}10$ (multi-round glutamate uncaging vs RuBi-glutamate uncaging control). For event area, rank sum test compares single round glutamate uncaging vs. multi-round glutamate uncaging, $p = 3.6\text{e-}10$. All datasets were collected in the presence of RuBi-glutamate. For single round and multi-round glutamate uncaging, the uncaging laser power was set to 70 A.U. ($\sim 8\text{mW}$ at the sample). Laser re-alignment between these datasets leads to a small difference in amount of glutamate uncaged with laser stimulation (see event area on right).

Extended Data Figure 3.7 continued on next page

Extended Data Figure 3.7 continued

For RuBi-glutamate uncaging controls, the uncaging laser power was set to 25 A.U. (~2mW at the sample), a stimulation that did not lead to detectable glutamate uncaging (see event number on left). **(b)** Distance of Cyto-GCaMP-expressing neighboring astrocytes from the glutamate uncaging site. Distance measured from the centroid of each neighboring astrocyte to the centroid of the uncaging site. Data shown by active astrocyte (≥ 1 AQuA-detected event 0–300s from recording onset), median, 25th and 75th percentile (single round glutamate uncaging: $n = 28$ FOV, 7 slices, 4 mice; multi-round glutamate uncaging: $n = 23$ FOV, 9 slices, 5 mice). Rank sum test compares datasets; $p = 3.4e-15$. **(c)** Correlation between the propagative Ca^{2+} responses of individual neighboring cells to multiple rounds of glutamate uncaging. Individual cells' binary responses to glutamate uncaging are not significantly correlated across rounds (Spearman rho = 0.040, $p = 1.0$, $n = 32$ cells, 15 recordings, 8 slices, 5 mice [round 1 vs 2]; Spearman rho = 0.14, $p = 0.70$, $n = 30$ cells, 16 recordings, 7 slices, 5 mice [round 1 vs 3]; Spearman rho = 0.059, $p = 0.74$, $n = 38$ cells, 17 recordings, 8 slices, 5 mice [round 2 vs 3]), showing that the response of an individual cell is variable from round to round. In each round, activity was recorded 150–0s before and 0–600s following uncaging, with glutamate uncaged over an area of $\sim 12\mu m^2$ (as in a, right “Multi-round glutamate uncaging”). Rounds of imaging/uncaging for each FOV were separated by ≥ 25 minutes. Cells included in analysis for each round had ≥ 1 propagative event during 60–0s before uncaging. Responding cells exhibited $\geq 50\%$ increase in propagative event frequency 300–420s following uncaging, a time window in which activity began to increase across rounds, compared to 60–0s before uncaging. **(d)** Event frequency change in neighboring astrocytes across three rounds of glutamate uncaging (top) and RuBi-glutamate uncaging controls (bottom). 90–0s before and 0–570s after uncaging used to calculate mean event number/30s in active astrocytes (astrocytes in the local network with ≥ 1 AQuA-detected event during recording, excluding the stimulated cell). Data shown by mean \pm sem (multi-round glutamate uncaging: $n = 23$ FOV for Round 1 and 3, 21 FOV for Round 2, 9 slices, 5 mice; RuBi-glutamate uncaging control: $n = 20$ FOV, 8 slices, 5 mice). Permutation test used to determine significance. p -values for all conditions, rounds, and time points are in Extended Data Table 3.14. The responses in multi-round glutamate uncaging are delayed compared to the single round glutamate uncaging dataset (Extended Data Fig. 3.3g). Two factors may account for this delay. First, less NT is released in the multi-round glutamate uncaging dataset (a). Second, the distance of astrocytes in the local network from the uncaging site is greater in the multi-round uncaging dataset compared to the single round uncaging dataset (b). **(e)** Baseline event frequencies for neighboring astrocytes across three rounds of glutamate uncaging. 90–0s before uncaging used to calculate mean event number/30s/active astrocytes in each FOV. Data shown FOV (light grey lines, $n = 21$ FOV, 9 slices, 5 mice) and mean \pm sem (black dots and error bars). Repeated measures ANOVA compares baseline frequencies across rounds ($F(2,40) = 1.51$, $p = 0.23$).

Tables

Extended Data Table 3.1. Statistics for Fig. 3.1c

Change in event frequency in astrocytes during bath-application of agonist. Permutation testing used to identify time-points with changes in event frequency greater than chance for each agonist. *p*-values corrected for multiple comparisons using Benjamini-Yekutieli procedure with $FDR \leq 0.05$. Adjusted *p*-values < 0.05 are bold.

Condition	Time relative to agonist entry (s)	<i>p</i> -values (raw)	<i>p</i> -values (adjusted)
Baclofen	-240 – -180	0.598040195980402	1.90331632015370
	-180 – -120	0.429157084291571	1.82110765113965
	-120 – -60	0.374462553744626	1.82110765113965
	-60 – 0	0.570242975702430	1.90331632015370
	0–60	0.339466053394661	1.82110765113965
	60–120	9.99900009999000e-05	0.000848605615628913
	120–180	9.99900009999000e-05	0.000848605615628913
	180–240	9.99900009999000e-05	0.000848605615628913
t-ACPD	-240 – -180	0.950704929507049	2.80096426865250
	-180 – -120	0.939206079392061	2.80096426865250
	-120 – -60	0.851514848515149	2.80096426865250
	-60 – 0	0.990100989901010	2.80096426865250
	0–60	9.99900009999000e-05	0.000848605615628913
	60–120	9.99900009999000e-05	0.000848605615628913
	120–180	9.99900009999000e-05	0.000848605615628913
	180–240	0.0241975802419758	0.154021919236648

Extended Data Table 3.2. Statistics for Fig. 3.1e–h

Dose-response curves. Paired t-tests at each concentration compare response to each agonist for each feature. *p*-values corrected for multiple comparisons using Bonferroni-Holm correction with FWER ≤ 0.05 . Adjusted *p*-values < 0.05 are bold.

Feature	Agonist concentration (μM)	<i>p</i> -values (raw)	<i>p</i> -values (adjusted)
Percent field active	5	0.106884262919877	0.106884262919877
	25	0.00453636186896923	0.00907272373793845
	50	0.000175165474580620	0.000700661898322481
	100	0.000644835771994738	0.00193450731598421
Event area	5	0.134291909278406	0.134291909278406
	25	0.00336246922231183	0.0100874076669355
	50	0.00274661524985296	0.0109864609994119
	100	0.0355015432722231	0.0710030865444463
Event duration	5	0.794523834669017	0.794523834669017
	25	0.00693357100768626	0.0208007130230588
	50	0.000707221042301198	0.00282888416920479
	100	0.0222444305319271	0.0444888610638542
Event propagation	5	0.503037904758348	0.503037904758348
	25	0.00201639415469164	0.00806557661876658
	50	0.00332572662050501	0.00997717986151502
	100	0.0102174453241840	0.0204348906483680

Extended Data Table 3.3. Statistics for Extended Data Fig. 3.1d

Mean $\Delta F/F$ in astrocytes during bath-application of agonist. Permutation testing used to identify time-points with increases in $\Delta F/F$ greater than chance for each agonist. p -values corrected for multiple comparisons using Benjamini-Yekutieli procedure with $FDR \leq 0.05$. Adjusted p -values < 0.05 are bold.

Condition	Time relative to agonist entry (s)	p -values (raw)	p -values (adjusted)
Baclofen	-300 – -270	0.950904909509049	3.48427432652907
	-270 – -240	0.617338266173383	3.48427432652907
	-240 – -210	0.853814618538146	3.48427432652907
	-210 – -180	0.391760823917608	3.08080444588937
	-180 – -150	0.996900309969003	3.48427432652907
	-150 – -120	0.528947105289471	3.48427432652907
	-120 – -90	0.957004299570043	3.48427432652907
	-90 – -60	0.982301769823018	3.48427432652907
	-60 – -30	0.995700429957004	3.48427432652907
	-30–0	0.654434556544346	3.48427432652907
	0–30	0.994300569943006	3.48427432652907
	30–60	0.00129987001299870	0.0157264137105124
	60–90	9.99900009999000e-05	0.00314528274210247
	90–120	0.00149985001499850	0.0157264137105124
	120–150	9.99900009999000e-05	0.00314528274210247
	150–180	0.0198980101989801	0.178831790193826
180–210	0.000499950004999500	0.00786320685525618	
210–240	0.000199980001999800	0.00419371032280330	
t-ACPD	-300 – -270	0.925507449255074	3.49510807819631
	-270 – -240	0.923607639236076	3.49510807819631
	-240 – -210	0.895510448955105	3.49510807819631
	-210 – -180	0.886511348865114	3.49510807819631
	-180 – -150	0.888211178882112	3.49510807819631
	-150 – -120	0.865413458654135	3.49510807819631
	-120 – -90	0.952504749525048	3.49510807819631
	-90 – -60	0.707029297070293	3.49510807819631
	-60 – -30	0.919608039196080	3.49510807819631
	-30–0	0.905409459054095	3.49510807819631
	0–30	9.99900009999000e-05	0.00314528274210247
	30–60	9.99900009999000e-05	0.00314528274210247
	60–90	1	3.49510807819631
	90–120	1	3.49510807819631
	120–150	1	3.49510807819631
	150–180	1	3.49510807819631
180–210	1	3.49510807819631	
210–240	1	3.49510807819631	

Extended Data Table 3.4. Statistics for Extended Data Fig. 3.1g

Event features pre- and post-agonist addition. Comparison of distributions of event area, duration, and propagation 120–0s before (“Pre”) or 0–120s after (“Post”) addition of baclofen (50 μ M) or t-ACPD (50 μ M). One-way ANOVA followed by Tukey-Kramer Test determine significant pairwise comparisons between conditions. *p*-values < 0.05 are bold, greyed-out cells are pairwise comparisons that are not relevant.

Feature	Test	Comparison	<i>p</i> -values
Area	1-way ANOVA		2.64502036644004e-13
	Tukey-Kramer Test	Bac_pre v Bac_post	0.898277274752255
		Bac_pre v tACPD_pre	0.995109946477354
		Bac_pre v tACPD_post	7.59031018511269e-05
		Bac_post v tACPD_pre	0.975557200328527
		Bac_post v tACPD_post	8.83569961640518e-09
	tACPD_pre v tACPD_post	0.000158328341554381	
Duration	1-way ANOVA		2.90200679997044e-19
	Tukey-Kramer Test	Bac_pre v Bac_post	0.705179159520994
		Bac_pre v tACPD_pre	0.997414358965489
		Bac_pre v tACPD_post	0.000778858034344410
		Bac_post v tACPD_pre	0.822905967024531
		Bac_post v tACPD_post	3.76825814996096e-09
	tACPD_pre v tACPD_post	0.000133775981740025	
Propagation distance	1-way ANOVA		5.06378633615887e-15
	Tukey-Kramer Test	Bac_pre v Bac_post	0.913414390535003
		Bac_pre v tACPD_pre	0.998952459006666
		Bac_pre v tACPD_post	3.10437553621146e-05
		Bac_post v tACPD_pre	0.959725706670736
		Bac_post v tACPD_post	4.12490908097141e-09
	tACPD_pre v tACPD_post	3.44219605847851e-05	
$\Delta F/F$	1-way ANOVA		1.35022940218368e-148
	Tukey-Kramer Test	Bac_pre v Bac_post	0.787076385709762
		Bac_pre v tACPD_pre	0.988259466617291
		Bac_pre v tACPD_post	3.76825814996096e-09
		Bac_post v tACPD_pre	0.518577476864315
		Bac_post v tACPD_post	3.76825814996096e-09
	tACPD_pre v tACPD_post	3.76825814996096e-09	

Extended Data Table 3.5. Statistics for Extended Data Fig. 3.2b

Change in event frequency in astrocytes directly stimulated with NT. Permutation testing used to identify time-points with changes in event frequency greater than chance for each condition. *p*-values corrected for multiple comparisons using Benjamini-Yekutieli procedure with FDR ≤ 0.05. Adjusted *p*-values < 0.05 are bold.

Condition	Time relative to uncaging (s)	<i>p</i> -values (raw)	<i>p</i> -values (adjusted)
GABA	0–30	0.196880311968803	0.449543378995434
	30–60	0.149385061493851	0.426369863013699
	60–90	0.0115988401159884	0.0441400304414003
	90–120	9.99900009999000e-05	0.00114155251141553
	120–150	0.00229977002299770	0.0131278538812785
Glutamate	0–30	0.118788121187881	0.339041095890411
	30–60	0.153984601539846	0.351598173515982
	60–90	0.000399960003999600	0.00228310502283105
	90–120	9.99900009999000e-05	0.00114155251141553
	120–150	0.0591940805919408	0.225266362252664
GABA + CGP55845	0–30	0.237476252374763	0.906392694063927
	30–60	0.363263673632637	1.03681506849315
	60–90	0.238176182381762	0.906392694063927
	90–120	0.00279972002799720	0.0319634703196347
	120–150	0.927407259274073	2.11757990867580
Glutamate + LY341495	0–30	0.0266973302669733	0.304794520547945
	30–60	0.883111688831117	2.23515981735160
	60–90	0.978902109789021	2.23515981735160
	90–120	0.919108089191081	2.23515981735160
	120–150	0.650334966503350	2.23515981735160
Laser uncaging control	0–30	0.0105989401059894	0.121004566210046
	30–60	0.0492950704929507	0.187595129375951
	60–90	0.407059294070593	1.16181506849315
	90–120	0.0379962003799620	0.187595129375951
	120–150	0.622337766223378	1.42100456621005

Extended Data Table 3.6. Statistics for Fig. 3.3h

Change in event frequency in the astrocyte network via Sholl-like analysis. Permutation testing used to identify time-points with changes in event frequency greater than chance for each distance band and NT. *p*-values corrected for multiple comparisons using Benjamini-Yekutieli procedure with $FDR \leq 0.05$. Adjusted *p*-values < 0.05 are bold.

NT	Distance from uncaging (μm)	Time relative to uncaging (s)	<i>p</i> -values (raw)	<i>p</i> -values (adjusted)
GABA	25–75	0–30	0.0569943005699430	0.216894977168950
		30–60	0.798720127987201	1.82374429223744
		60–90	0.0429957004299570	0.216894977168950
		90–120	0.00599940005999400	0.0684931506849315
		120–150	0.535546445355465	1.52853881278539
	75–125	0–30	0.0666933306669333	0.276636225266362
		30–60	0.187281271872813	0.534531963470320
		60–90	0.0726927307269273	0.276636225266362
		90–120	0.00299970002999700	0.0342465753424658
		120–150	0.307269273072693	0.701598173515982
	125–175	0–30	0.0418958104189581	0.0956621004566210
		30–60	0.0140985901409859	0.0536529680365297
		60–90	0.0192980701929807	0.0550799086757991
		90–120	9.99900009999000e-05	0.00114155251141553
		120–150	0.00379962003799620	0.0216894977168950
	glutamate	25–75	0–30	0.00169983001699830
30–60			0.00119988001199880	0.00646879756468798
60–90			0.00799920007999200	0.0228310502283105
90–120			9.99900009999000e-05	0.00114155251141553
120–150			0.0128987101289871	0.0294520547945206
75–125		0–30	0.255074492550745	0.728025114155251
		30–60	0.00459954004599540	0.0262557077625571
		60–90	0.00779922007799220	0.0296803652968037
		90–120	9.99900009999000e-05	0.00114155251141553
		120–150	0.576442355764424	1.31621004566210
125–175		0–30	0.113988601139886	0.260273972602740
		30–60	0.0355964403559644	0.135464231354642
		60–90	0.00949905009499050	0.0542237442922375
		90–120	9.99900009999000e-05	0.00114155251141553
		120–150	0.0554944505549445	0.158390410958904

Extended Data Table 3.7. Statistics for Extended Data Fig. 3.3g, h

Change in event frequency in individual astrocytes in the network. Permutation testing used to identify time-points with changes in event frequency greater than chance for each condition. *p*-values corrected for multiple comparisons using Benjamini-Yekutieli procedure with FDR \leq 0.05. Adjusted *p*-values < 0.05 are bold.

Condition	Time relative to uncaging (s)	<i>p</i> -values (raw)	<i>p</i> -values (adjusted)
GABA WT	0–30	0.00409959004099590	0.0156012176560122
	30–60	0.0294970502949705	0.0841894977168950
	60–90	0.000299970002999700	0.00171232876712329
	90–120	9.99900009999000e-05	0.00114155251141553
	120–150	0.519848015198480	1.18698630136986
Glutamate WT	0–30	0.00479952004799520	0.0136986301369863
	30–60	9.99900009999000e-05	0.000570776255707763
	60–90	0.000299970002999700	0.00114155251141553
	90–120	9.99900009999000e-05	0.000570776255707763
	120–150	0.0480951904809519	0.109817351598174
GABA Cx43 ^{flxed}	0–30	0.0586941305869413	0.335045662100457
	30–60	0.943105689431057	2.15342465753425
	60–90	0.373262673732627	1.42047184170472
	90–120	0.000499950004999500	0.00570776255707763
	120–150	0.814718528147185	2.15342465753425
Glutamate Cx43 ^{flxed}	0–30	0.668933106689331	1.90924657534247
	30–60	0.878712128787121	2.00639269406393
	60–90	0.0154984501549845	0.176940639269406
	90–120	0.0617938206179382	0.352739726027397
	120–150	0.666933306669333	1.90924657534247
GABA + CGP55845	0–30	0.229877012298770	1.32363013698630
	30–60	0.460253974602540	1.32363013698630
	60–90	0.234976502349765	1.32363013698630
	90–120	0.463753624637536	1.32363013698630
	120–150	0.971902809719028	2.21917808219178
Glutamate + LY341495	0–30	0.181181881811819	0.997716894977169
	30–60	0.427057294270573	1.21889269406393
	60–90	0.160683931606839	0.997716894977169
	90–120	0.660733926607339	1.50867579908676
	120–150	0.262173782621738	0.997716894977169
Laser uncaging control	0–30	0.00899910008999100	0.102739726027397
	30–60	0.498050194980502	1.42151826484018
	60–90	0.668633136686331	1.52671232876712
	90–120	0.130786921307869	0.746575342465753
	120–150	0.239876012398760	0.912861491628615

Extended Data Table 3.8. Statistics for Fig. 3.4b

Change in probability of Ca²⁺ events propagating toward or away from pia compared to baseline. Two-sided permutation testing was used to identify time bins with changes in propagative event probability compared to baseline. *p*-values were adjusted across tested time bins using the Benjamini-Hochberg procedure to obtain *q*-values. *q*-values < 0.05 are bold.

NT	Time relative to uncaging	<i>p</i> -value	<i>q</i> -value
GABA	-60-0	1.0	—
	0-30	0.10908909109089	0.218178182181781
	30-60	0.132586741325867	0.219406630765494
	60-90	0.350264973502649	0.389183303891833
	90-120	0.276672332766723	0.345840415958404
	120-150	0.153584641535846	0.219406630765494
glutamate	-60-0	1.0	—
	0-30	0.0011998800119988	0.005999400059994
	30-60	0.0161983801619838	0.0404959504049595
	60-90	0.002999700029997	0.00999900009999
	90-120	0.0008999100089991	0.005999400059994
	120-150	0.651534846515348	0.651534846515348

Extended Data Table 3.9. N for Fig. 3.4f, h, j, k and Extended Data Fig. 3.6

Fold-change in rate of static or propagative Ca²⁺ events in neighboring cells post NT-uncaging in WT and Cx43^{flox^{ed}} mice. Event rate changes were used to calculate the fraction of neighboring cells/FOV responding to NT-uncaging for each condition (Fig. 3.4 h and k and Extended Data Fig. 3.6 e–f).

Genotype	Event Category	NT	N				
			event	cell	FOV	slice	mice
WT	static	GABA	8417	142	28	7	4
		glutamate	6998	120	27	7	4
	propagative	GABA	1358	135	28	7	4
		glutamate	1112	115	27	7	4
Cx43 ^{flox^{ed}}	static	GABA	1566	60	28	14	8
		glutamate	1215	47	23	14	8
	propagative	GABA	487	57	28	14	8
		glutamate	348	47	23	14	8

Extended Data Table 3.10. Statistics for Fig. 3.4f, j and Extended Data Fig. 3.6b–c
 Fold-change in rate of static or propagative Ca²⁺ events among neighboring cells post NT-uncaging in WT and Cx43^{floxed} mice. One-sided permutation test used to identify time bins with static or propagative event rate increases compared to baseline. *p*-values were adjusted across tested time bins using the Benjamini-Hochberg procedure to obtain *q*-values. *q*-values < 0.05 are bold.

Genotype	Event Category	NT	Time relative to uncaging	<i>p</i> -value	<i>q</i> -value
WT	static	GABA	-60–0	1.0	—
			0–30	0.5649435056494350	0.5888411158884110
			30–60	0.5888411158884110	0.5888411158884110
			60–90	0.0560943905609439	0.1121887811218870
			90–120	0.0012998700129987	0.0064993500649935
			120–150	0.0150984901509849	0.0377462253774622
		glutamate	-60–0	1.0	—
			0–30	0.2686731326867310	0.3735876412358760
			30–60	0.0066993300669933	0.0223311002233110
			60–90	0.1374862513748620	0.2291437522914370
			90–120	0.0009999000099990	0.0064993500649935
			120–150	0.2988701129887010	0.3735876412358760
	propagative	GABA	-60–0	1.0	—
			0–30	0.0341965803419658	0.0683931606839316
			30–60	0.6876312368763120	0.7640347076403470
			60–90	0.2723727627237270	0.3404659534046590
			90–120	0.0726927307269273	0.1211545512115450
			120–150	0.9524047595240470	0.9524047595240470
		glutamate	-60–0	1.0	—
			0–30	0.0071992800719928	0.0179982001799820
			30–60	0.0071992800719928	0.0179982001799820
			60–90	0.0000999900009999	0.0004999500049995
			90–120	0.0000999900009999	0.0004999500049995
			120–150	0.2249775022497750	0.3213964317853920
Cx43 ^{floxed}	static	GABA	-60–0	1.0	—
			0–30	0.961603839616038	0.995600439956004
			30–60	0.698030196980302	0.995600439956004
			60–90	0.859614038596140	0.995600439956004
			90–120	0.198480151984801	0.995600439956004
			120–150	0.874012598740125	0.995600439956004
		glutamate	-60–0	1.0	—
			0–30	0.559344065593440	0.995600439956004
			30–60	0.995600439956004	0.995600439956004
			60–90	0.915308469153084	0.995600439956004
			90–120	0.700929907009299	0.995600439956004
			120–150	0.798820117988201	0.995600439956004
	propagative	GABA	-60–0	1.0	—
			0–30	0.812918708129187	0.933684409336844

Genotype	Event Category	NT	Time relative to uncaging	<i>p</i>-value	<i>q</i>-value
			30–60	0.939206079392060	0.939206079392060
			60–90	0.444755524447555	0.933684409336844
			90–120	0.830316968303169	0.933684409336844
			120–150	0.813818618138186	0.933684409336844
		glutamate	-60–0	1.0	—
			0–30	0.793020697930207	0.933684409336844
			30–60	0.834616538346165	0.933684409336844
			60–90	0.397960203979602	0.933684409336844
			90–120	0.379562043795620	0.933684409336844
			120–150	0.840315968403159	0.933684409336844

Extended Data Table 3.11. N for Fig. 3.4m

Fraction of neighboring cells responding to NT-uncaging with propagative event frequency increases separated by baseline activity levels. “All” (static and propagative) events were used to calculate overall baseline event rate and fraction of propagative events in the baseline period to separate cells into “low” and “high” overall baseline activity or “low” and “high” baseline propagation, respectively. Propagative events were used to categorize cells as “responders” or “non-responders” to NT-uncaging.

Event Category	NT	N				
		event	cell	FOV	slice	mice
all	GABA	9775	142	28	7	4
	glutamate	8110	120	27	7	4
propagative	GABA	1358	135	28	7	4
	glutamate	1112	115	27	7	4

Extended Data Table 3.12. Statistics for Extended Data Fig. 3.4a

Fold change in individual Ca²⁺ events features compared to baseline. Two-sided permutation testing was used to identify time bins with changes in event features compared to baseline. *p*-values were adjusted across tested time bins using the Benjamini-Hochberg procedure to obtain *q*-values. *q*-values < 0.05 are bold.

Event Feature	NT	Time relative to uncaging	<i>p</i> -value	<i>q</i> -value	
Area	GABA	-60-0	1.0	—	
		0-30	0.2707292707292700	0.3867561010418150	
		30-60	0.7262737262737260	0.8069708069708070	
		60-90	0.5004995004995000	0.6256243756243750	
		90-120	0.1428571428571420	0.2380952380952380	
		120-150	0.0159840159840159	0.0474525474525474	
	glutamate	-60-0	1.0	—	
		0-30	0.0099900099900100	0.0474525474525474	
		30-60	0.0709290709290709	0.1418581418581410	
		60-90	0.0189810189810189	0.0474525474525474	
		90-120	0.0019980019980020	0.0199800199800199	
		120-150	0.9890109890109890	0.9890109890109890	
	Perimeter	GABA	-60-0	1.0	—
			0-30	0.2907092907092900	0.4152989867275580
30-60			0.8021978021978020	0.8021978021978020	
60-90			0.3806193806193800	0.4273504273504270	
90-120			0.1398601398601390	0.2331002331002330	
120-150			0.0619380619380619	0.1238761238761230	
glutamate		-60-0	1.0	—	
		0-30	0.0189810189810189	0.0632700632700632	
		30-60	0.0359640359640359	0.0899100899100899	
		60-90	0.0059940059940060	0.0299700299700299	
		90-120	0.0009990009990010	0.0099900099900100	
		120-150	0.3846153846153840	0.4273504273504270	
Circularity		GABA	-60-0	1.0	—
			0-30	0.3686313686313680	0.4095904095904090
	30-60		0.3276723276723270	0.4095904095904090	
	60-90		0.3266733266733260	0.4095904095904090	
	90-120		0.1928071928071920	0.3213453213453210	
	120-150		0.5244755244755240	0.5244755244755240	
	glutamate	-60-0	1.0	—	
		0-30	0.0369630369630369	0.0739260739260739	
		30-60	0.0089910089910090	0.0299700299700299	
		60-90	0.0089910089910090	0.0299700299700299	
		90-120	0.0009990009990010	0.0099900099900100	
		120-150	0.0249750249750249	0.0624375624375624	
	Peak ΔF/F	GABA	-60-0	1.0	—
			0-30	0.7932067932067930	0.8813408813408810
30-60			0.6193806193806190	0.8728771228771220	
60-90			0.9460539460539460	0.9460539460539460	

Event Feature	NT	Time relative to uncaging	<i>p</i> -value	<i>q</i> -value		
		90–120	0.3456543456543450	0.8641358641358640		
		120–150	0.0079920079920080	0.0399600399600399		
	glutamate	-60–0	1.0	—		
		0–30	0.6983016983016980	0.8728771228771220		
		30–60	0.2247752247752240	0.7492507492507490		
		60–90	0.6513486513486510	0.8728771228771220		
		90–120	0.5284715284715280	0.8728771228771220		
		120–150	0.0009990009990010	0.0099900099900100		
Fall time	GABA	-60–0	1.0	—		
		0–30	0.9150849150849150	0.9150849150849150		
		30–60	0.0789210789210789	0.1578421578421570		
		60–90	0.0549450549450549	0.1373626373626370		
		90–120	0.0079920079920080	0.0266400266400266		
		120–150	0.0009990009990010	0.0049950049950050		
	glutamate	-60–0	1.0	—		
		0–30	0.2287712287712280	0.3812853812853810		
		30–60	0.5644355644355640	0.6271506271506270		
		60–90	0.3876123876123870	0.4845154845154840		
		90–120	0.3426573426573420	0.4845154845154840		
		120–150	—	—		
		Rise time	GABA	-60–0	1.0	—
				0–30	0.1798201798201790	0.1998001998001990
30–60	0.1088911088911080			0.1361138861138860		
60–90	0.0109890109890109			0.0156985871271585		
90–120	0.0019980019980020			0.0049950049950050		
120–150	0.6643356643356640			0.6643356643356640		
glutamate	-60–0		1.0	—		
	0–30		0.0109890109890109	0.0156985871271585		
	30–60		0.0049950049950050	0.0099900099900100		
	60–90		0.0009990009990010	0.0033300033300033		
	90–120		0.0009990009990010	0.0033300033300033		
	120–150		0.0009990009990010	0.0033300033300033		
Decay time constant	GABA	-60–0	1.0	—		
		0–30	0.8951048951048950	0.8951048951048950		
		30–60	0.1318681318681310	0.3216783216783210		
		60–90	0.1608391608391600	0.3216783216783210		
		90–120	0.0199800199800199	0.0666000666000666		
		120–150	—	—		
	glutamate	-60–0	1.0	—		
		0–30	0.3766233766233760	0.5380333951762520		
		30–60	0.7402597402597400	0.8225108225108220		
		60–90	0.3686313686313680	0.5380333951762520		
		90–120	0.4775224775224770	0.5969030969030960		
		120–150	—	—		
		Duration (10% peak)	GABA	-60–0	1.0	—
				0–30	0.5714285714285710	0.7842157842157840
30–60	0.6273726273726270			0.7842157842157840		

Event Feature	NT	Time relative to uncaging	<i>p</i>-value	<i>q</i>-value
		60–90	0.9650349650349650	0.9650349650349650
		90–120	0.8731268731268730	0.9650349650349650
		120–150	—	—
	glutamate	-60–0	1.0	—
		0–30	0.0409590409590409	0.0999000999000999
		30–60	0.0499500499500499	0.0999000999000999
		60–90	0.0239760239760239	0.0799200799200799
		90–120	0.0639360639360639	0.1065601065601060
		120–150	—	—

Extended Data Table 3.13. Statistics for Extended Data Fig. 3.4b

Change in probability of Ca²⁺ events growing or shrinking in the indicated direction compared to baseline. Two-sided permutation testing was used to identify time bins with changes in propagation probability compared to baseline. *p*-values were adjusted across tested time bins using the Benjamini-Hochberg procedure to obtain *q*-values. *q*-values < 0.05 are bold.

Propagation direction	NT	Time relative to uncaging	<i>p</i> -value	<i>q</i> -value		
Growth toward pia	GABA	-60-0	1.0	—		
		0-30	0.4575424575424570	0.6978735550164120		
		30-60	0.3976023976023970	0.6978735550164120		
		60-90	0.5764235764235760	0.7159507159507160		
		90-120	0.7182817182817180	0.7182817182817180		
		120-150	0.4885114885114880	0.6978735550164120		
	glutamate	-60-0	1.0	—		
		0-30	0.0009990009990010	0.0099900099900100		
		30-60	0.0149850149850149	0.0374625374625374		
		60-90	0.0049950049950050	0.0166500166500166		
		90-120	0.0019980019980020	0.0099900099900100		
		120-150	0.6443556443556440	0.7159507159507160		
		Growth away from pia	GABA	-60-0	1.0	—
				0-30	0.6063936063936060	0.6063936063936060
30-60	0.1988011988011980			0.2840017125731410		
60-90	0.5224775224775220			0.5805305805305800		
90-120	0.2367632367632360			0.2959540459540450		
120-150	0.0529470529470529			0.1323676323676320		
glutamate	-60-0		1.0	—		
	0-30		0.0179820179820179	0.0899100899100899		
	30-60		0.0929070929070929	0.1858141858141850		
	60-90		0.0139860139860139	0.0899100899100899		
	90-120		0.0319680319680319	0.1065601065601060		
	120-150		0.1368631368631360	0.2281052281052280		
	Growth right		GABA	-60-0	1.0000000000000000	—
				0-30	0.6513486513486510	0.7237207237207230
30-60		0.4195804195804190		0.5994005994005990		
60-90		0.8341658341658340		0.8341658341658340		
90-120		0.3056943056943050		0.5094905094905090		
120-150		0.0119880119880119		0.0599400599400599		
glutamate		-60-0	1.0	—		
		0-30	0.0009990009990010	0.0099900099900100		
		30-60	0.0609390609390609	0.1523476523476520		
		60-90	0.0229770229770229	0.0765900765900765		
		90-120	0.0829170829170829	0.1658341658341650		
		120-150	0.6493506493506490	0.7237207237207230		
		Growth left	GABA	-60-0	1.0	—
				0-30	0.1148851148851140	0.1914751914751910
30-60	0.3736263736263730			0.4895104895104890		
60-90	0.3916083916083910			0.4895104895104890		

Propagation direction	NT	Time relative to uncaging	<i>p</i> -value	<i>q</i> -value		
	glutamate	90–120	0.4835164835164830	0.5372405372405370		
		120–150	0.0609390609390609	0.1298701298701290		
		-60–0	1.0	—		
		0–30	0.0569430569430569	0.1298701298701290		
		30–60	0.0479520479520479	0.1298701298701290		
		60–90	0.0389610389610389	0.1298701298701290		
		90–120	0.0649350649350649	0.1298701298701290		
		120–150	0.9230769230769230	0.9230769230769230		
Shrinking away from pia	GABA	-60–0	1.0	—		
		0–30	0.6213786213786210	0.7170607170607170		
		30–60	0.4595404595404590	0.6564863707720850		
		60–90	0.9120879120879120	0.9120879120879120		
		90–120	0.1958041958041950	0.3916083916083910		
		120–150	0.1328671328671320	0.3321678321678320		
	glutamate	-60–0	1.0	—		
		0–30	0.0809190809190809	0.3321678321678320		
		30–60	0.0309690309690309	0.3096903096903090		
		60–90	0.2447552447552440	0.4079254079254070		
		90–120	0.1268731268731260	0.3321678321678320		
		120–150	0.6453546453546450	0.7170607170607170		
		Shrinking away from deeper layers	GABA	-60–0	1.0	—
				0–30	0.6793206793206790	0.7472527472527470
30–60	0.2237762237762230			0.4475524475524470		
60–90	0.6083916083916080			0.7472527472527470		
90–120	0.7472527472527470			0.7472527472527470		
120–150	0.0339660339660339			0.1898101898101890		
glutamate	-60–0		1.0	—		
	0–30		0.0569430569430569	0.1898101898101890		
	30–60		0.3356643356643350	0.5594405594405590		
	60–90		0.0419580419580419	0.1898101898101890		
	90–120		0.2097902097902090	0.4475524475524470		
	120–150		0.4985014985014980	0.7121449978592830		
	Shrinking away from right		GABA	-60–0	1.0000000000000000	1.0000000000000000
				0–30	0.6383616383616380	0.6383616383616380
30–60		0.3776223776223770		0.5394605394605390		
60–90		0.4615384615384610		0.5769230769230760		
90–120		0.1898101898101890		0.3796203796203790		
120–150		0.2517482517482510		0.4195804195804190		
glutamate		-60–0	1.0	—		
		0–30	0.0799200799200799	0.3796203796203790		
		30–60	0.1718281718281710	0.3796203796203790		
		60–90	0.1528471528471520	0.3796203796203790		
		90–120	0.1018981018981010	0.3796203796203790		
		120–150	0.5754245754245750	0.6383616383616380		
		GABA	-60–0	1.0	—	
			0–30	0.6963036963036960	0.8191808191808190	
30–60	0.1238761238761230		0.2397602397602390			

Propagation direction	NT	Time relative to uncaging	<i>p</i>-value	<i>q</i>-value
Shrinking away from left		60–90	0.7372627372627370	0.8191808191808190
		90–120	0.2047952047952040	0.2925645782788640
		120–150	0.1438561438561430	0.2397602397602390
	glutamate	-60–0	1.0	—
		0–30	0.0849150849150849	0.2397602397602390
		30–60	0.0499500499500499	0.2397602397602390
		60–90	0.0179820179820179	0.1798201798201790
		90–120	0.1348651348651340	0.2397602397602390
		120–150	0.8341658341658340	0.8341658341658340

Extended Data Table 3.14. Statistics for Extended Data Fig. 3.7d

Change in event frequency in neighboring cells during multiple rounds of glutamate uncaging or in RuBi-glutamate uncaging controls. Permutation testing used to identify time-points with changes in event frequency greater than chance for each condition. *p*-values corrected for multiple comparisons using Benjamini-Yekutieli procedure with $FDR \leq 0.05$. Adjusted *p*-values < 0.05 are bold.

Dataset	Round	Time relative to uncaging	<i>p</i> -values (raw)	<i>p</i> -values (adjusted)
Multi-round glutamate uncaging	Round 1	0–30	0.107389261073893	0.482586244333393
		30–60	0.497850214978502	1.86436755938545
		60–90	0.373962603739626	1.48280689599646
		90–120	0.101789821017898	0.482586244333393
		120–150	0.613638636136386	2.17703012457662
		150–180	0.00779922007799220	0.0438102037453499
		180–210	0.0619938006199380	0.321447648782449
		210–240	0.00389961003899610	0.0238964747701909
		240–270	0.135986401359864	0.572902664362268
		270–300	0.00119988001199880	0.00898670846058460
		300–330	0.000199980001999800	0.00192572324155384
		330–360	0.000799920007999200	0.00674003134543845
		360–390	0.00289971002899710	0.0195460909017715
		390–420	9.99900009999000e-05	0.00112333855757308
		420–450	9.99900009999000e-05	0.00112333855757308
		450–480	9.99900009999000e-05	0.00112333855757308
		480–510	9.99900009999000e-05	0.00112333855757308
		510–540	9.99900009999000e-05	0.00112333855757308
	540–570	9.99900009999000e-05	0.00112333855757308	
	Round 2	0–30	0.104989501049895	0.505502350907884
		30–60	0.379962003799620	1.58866503536305
		60–90	0.679432056794321	2.41044805222391
		90–120	0.561243875612439	2.10176644121922
		120–150	0.363463653634637	1.58866503536305
		150–180	0.0125987401259874	0.0943604388361383
		180–210	0.0209979002099790	0.141540658254208
		210–240	0.400659934006599	1.58866503536305
		240–270	0.0349965003499650	0.214455542809405
		270–300	0.103689631036896	0.505502350907884
		300–330	0.0536946305369463	0.301616402708371
		330–360	0.000199980001999800	0.00168500783635961
		360–390	9.99900009999000e-05	0.000962861620776922
390–420		9.99900009999000e-05	0.000962861620776922	
420–450	9.99900009999000e-05	0.000962861620776922		
450–480	9.99900009999000e-05	0.000962861620776922		

Dataset	Round	Time relative to uncaging	<i>p</i> -values (raw)	<i>p</i> -values (adjusted)
		480–510	9.99900009999000e-05	0.000962861620776922
		510–540	9.99900009999000e-05	0.000962861620776922
		540–570	9.99900009999000e-05	0.000962861620776922
	Round 3	0–30	0.684231576842316	2.71306085275502
		30–60	0.654234576542346	2.71306085275502
		60–90	0.806319368063194	3.01953404275643
		90–120	0.357364263573643	1.85299015604593
		120–150	0.244075592440756	1.49567422856502
		150–180	0.354064593540646	1.85299015604593
		180–210	0.622237776222378	2.71306085275502
		210–240	0.904009599040096	3.20719070495311
		240–270	0.0222977702229777	0.187878373754097
		270–300	0.479252074792521	2.30749787419189
		300–330	0.135886411358864	1.01774473316121
		330–360	0.210678932106789	1.42012460448388
		360–390	0.00909909009099090	0.0876204074906999
		390–420	0.000599940005999400	0.00674003134543845
		420–450	9.99900009999000e-05	0.00168500783635961
		450–480	9.99900009999000e-05	0.00168500783635961
		480–510	0.000499950004999500	0.00674003134543845
		510–540	9.99900009999000e-05	0.00168500783635961
540–570	9.99900009999000e-05	0.00168500783635961		
RuBi-glutamate uncaging control	Round 1	0–30	0.982401759824018	3.53816171786332
		30–60	0.778222177782222	3.08574493891456
		60–90	0.0261973802619738	0.346630183479692
		90–120	0.00819918008199180	0.276341285162977
		120–150	0.392460753924608	1.83778188018955
		150–180	0.997300269973003	3.53816171786332
		180–210	0.408959104089591	1.83778188018955
		210–240	0.601639836016398	2.53467303784395
		240–270	0.0212978702129787	0.346630183479692
		270–300	0.211778822117788	1.18961553246989
		300–330	0.103589641035896	0.634788406715840
		330–360	0.0359964003599640	0.346630183479692
		360–390	0.0818918108189181	0.552008567191409
		390–420	0.0743925607439256	0.552008567191409
		420–450	0.00609939006099390	0.276341285162977
		450–480	0.0521947805219478	0.439787045289859
		480–510	0.0229977002299770	0.346630183479692
		510–540	0.0346965303469653	0.346630183479692
		540–570	0.267973202679732	1.38948338505962
	Round 2	0–30	0.0592940705929407	1.75240814981400

Dataset	Round	Time relative to uncaging	<i>p</i>-values (raw)	<i>p</i>-values (adjusted)
		30–60	0.604039596040396	2.85187576303865
		60–90	0.0238976102389761	1.61086749155979
		90–120	0.121987801219878	1.75240814981400
		120–150	0.916208379162084	3.25046880096066
		150–180	0.847915208479152	3.17530365607323
		180–210	0.755224477552245	2.99455627953510
		210–240	0.137786221377862	1.75240814981400
		240–270	0.155984401559844	1.75240814981400
		270–300	0.676932306769323	2.85187576303865
		300–330	0.207279272072793	1.99601213987056
		330–360	0.479252074792521	2.69208085322388
		360–390	0.116288371162884	1.75240814981400
		390–420	0.341065893410659	2.55447187992117
		420–450	0.324367563243676	2.55447187992117
		450–480	0.666833316668333	2.85187576303865
		480–510	0.419858014198580	2.57285378359055
		510–540	0.604739526047395	2.85187576303865
	540–570	0.381361863813619	2.57064795515023	
	Round 3	0–30	0.593640635936406	2.66770440652454
		30–60	0.869013098690131	3.36402453374550
		60–90	0.287671232876712	2.66770440652454
		90–120	0.0991900809919008	1.67152777366874
		120–150	0.327267273272673	2.66770440652454
		150–180	0.999100089991001	3.54454701071690
		180–210	0.505849415058494	2.66770440652454
		210–240	0.406459354064594	2.66770440652454
		240–270	0.0353964603539646	1.19298554814261
		270–300	0.515848415158484	2.66770440652454
		300–330	0.357564243575642	2.66770440652454
		330–360	0.0989901009899010	1.67152777366874
		360–390	0.572942705729427	2.66770440652454
		390–420	0.465453454654535	2.66770440652454
		420–450	0.859514048595141	3.36402453374550
450–480		0.206879312068793	2.66770440652454	
480–510	0.00809919008099190	0.545942538980515		
510–540	0.431456854314569	2.66770440652454		
540–570	0.898310168983102	3.36402453374550		

References

1. Poskanzer, K. E. & Yuste, R. Astrocytes regulate cortical state switching in vivo. *Proc Natl Acad Sci USA* **113**, E2675-84 (2016).
2. Mariotti, L., Losi, G., Sessolo, M., Marcon, I. & Carmignoto, G. The inhibitory neurotransmitter GABA evokes long-lasting Ca(2+) oscillations in cortical astrocytes. *Glia* **64**, 363–373 (2016).
3. Bindocci, E. *et al.* Three-dimensional Ca²⁺ imaging advances understanding of astrocyte biology. *Science* **356**, (2017).
4. Di Castro, M. A. *et al.* Local Ca²⁺ detection and modulation of synaptic release by astrocytes. *Nat. Neurosci.* **14**, 1276–1284 (2011).
5. Vaidyanathan, T. V., Collard, M., Yokoyama, S., Reitman, M. E. & Poskanzer, K. E. Cortical astrocytes independently regulate sleep depth and duration via separate GPCR pathways. *eLife* **10**, (2021).
6. Perea, G. & Araque, A. Properties of synaptically evoked astrocyte calcium signal reveal synaptic information processing by astrocytes. *J. Neurosci.* **25**, 2192–2203 (2005).
7. Panatier, A. *et al.* Astrocytes are endogenous regulators of basal transmission at central synapses. *Cell* **146**, 785–798 (2011).
8. Perea, G. *et al.* Activity-dependent switch of GABAergic inhibition into glutamatergic excitation in astrocyte-neuron networks. *eLife* **5**, (2016).
9. Gordon, G. R. J. *et al.* Astrocyte-mediated distributed plasticity at hypothalamic glutamate synapses. *Neuron* **64**, 391–403 (2009).
10. Poskanzer, K. E. & Yuste, R. Astrocytic regulation of cortical UP states. *Proc Natl Acad Sci USA* **108**, 18453–18458 (2011).

11. Kang, J., Jiang, L., Goldman, S. A. & Nedergaard, M. Astrocyte-mediated potentiation of inhibitory synaptic transmission. *Nat. Neurosci.* **1**, 683–692 (1998).
12. Pasti, L., Volterra, A., Pozzan, T. & Carmignoto, G. Intracellular calcium oscillations in astrocytes: a highly plastic, bidirectional form of communication between neurons and astrocytes in situ. *J. Neurosci.* **17**, 7817–7830 (1997).
13. Farhy-Tselnicker, I. *et al.* Activity-dependent modulation of synapse-regulating genes in astrocytes. *eLife* **10**, (2021).
14. Srinivasan, R. *et al.* New transgenic mouse lines for selectively targeting astrocytes and studying calcium signals in astrocyte processes in situ and in vivo. *Neuron* **92**, 1181–1195 (2016).
15. Serrano, A., Haddjeri, N., Lacaille, J.-C. & Robitaille, R. GABAergic network activation of glial cells underlies hippocampal heterosynaptic depression. *J. Neurosci.* **26**, 5370–5382 (2006).
16. Schweitzer, C. *et al.* Characterization of [(3)H]-LY354740 binding to rat mGlu2 and mGlu3 receptors expressed in CHO cells using semliki forest virus vectors. *Neuropharmacology* **39**, 1700–1706 (2000).
17. Mutel, V. *et al.* Characterization of [(3)H]Quisqualate binding to recombinant rat metabotropic glutamate 1a and 5a receptors and to rat and human brain sections. *J. Neurochem.* **75**, 2590–2601 (2000).
18. Tang, W. *et al.* Stimulation-evoked Ca²⁺ signals in astrocytic processes at hippocampal CA3-CA1 synapses of adult mice are modulated by glutamate and ATP. *J. Neurosci.* **35**, 3016–3021 (2015).

19. Sun, W. *et al.* Glutamate-dependent neuroglial calcium signaling differs between young and adult brain. *Science* **339**, 197–200 (2013).
20. Wang, Y. *et al.* Accurate quantification of astrocyte and neurotransmitter fluorescence dynamics for single-cell and population-level physiology. *Nat. Neurosci.* **22**, 1936–1944 (2019).
21. Harada, K. *et al.* Red fluorescent protein-based cAMP indicator applicable to optogenetics and in vivo imaging. *Sci. Rep.* **7**, 7351 (2017).
22. Moldrich, R. X., Apricó, K., Diwakarla, S., O’Shea, R. D. & Beart, P. M. Astrocyte mGlu(2/3)-mediated cAMP potentiation is calcium sensitive: studies in murine neuronal and astrocyte cultures. *Neuropharmacology* **43**, 189–203 (2002).
23. Oe, Y. *et al.* Distinct temporal integration of noradrenaline signaling by astrocytic second messengers during vigilance. *Nat. Commun.* **11**, 471 (2020).
24. Kellner, V. *et al.* Dual metabotropic glutamate receptor signaling enables coordination of astrocyte and neuron activity in developing sensory domains. *Neuron* **109**, 2545–2555.e7 (2021).
25. Hirono, M., Yoshioka, T. & Konishi, S. GABA(B) receptor activation enhances mGluR-mediated responses at cerebellar excitatory synapses. *Nat. Neurosci.* **4**, 1207–1216 (2001).
26. New, D. C., An, H., Ip, N. Y. & Wong, Y. H. GABAB heterodimeric receptors promote Ca²⁺ influx via store-operated channels in rat cortical neurons and transfected Chinese hamster ovary cells. *Neuroscience* **137**, 1347–1358 (2006).
27. Zeng, W. *et al.* A new mode of Ca²⁺ signaling by G protein-coupled receptors: gating of IP₃ receptor Ca²⁺ release channels by Gbetagamma. *Curr. Biol.* **13**, 872–876 (2003).

28. Durkee, C. A. *et al.* Gi/o protein-coupled receptors inhibit neurons but activate astrocytes and stimulate gliotransmission. *Glia* **67**, 1076–1093 (2019).
29. Matsuzaki, M. *et al.* Dendritic spine geometry is critical for AMPA receptor expression in hippocampal CA1 pyramidal neurons. *Nat. Neurosci.* **4**, 1086–1092 (2001).
30. Higley, M. J. & Sabatini, B. L. Competitive regulation of synaptic Ca²⁺ influx by D2 dopamine and A2A adenosine receptors. *Nat. Neurosci.* **13**, 958–966 (2010).
31. Araya, R., Vogels, T. P. & Yuste, R. Activity-dependent dendritic spine neck changes are correlated with synaptic strength. *Proc Natl Acad Sci USA* **111**, E2895-904 (2014).
32. Kwon, T. *et al.* Ultrastructural, molecular and functional mapping of gabaergic synapses on dendritic spines and shafts of neocortical pyramidal neurons. *Cereb. Cortex* **29**, 2771–2781 (2019).
33. Bernardinelli, Y. *et al.* Activity-dependent structural plasticity of perisynaptic astrocytic domains promotes excitatory synapse stability. *Curr. Biol.* **24**, 1679–1688 (2014).
34. Filevich, O. & Etchenique, R. RuBiGABA-2: a hydrophilic caged GABA with long wavelength sensitivity. *Photochem. Photobiol. Sci.* **12**, 1565–1570 (2013).
35. Peterka, D. S. *et al.* Fast two-photon neuronal imaging and control using a spatial light modulator and ruthenium compounds. in *Photonic Therapeutics and Diagnostics VI* (eds. Kollias, N. *et al.*) vol. 7548 75484P (SPIE, 2010).
36. Fino, E. *et al.* RuBi-Glutamate: Two-Photon and Visible-Light Photoactivation of Neurons and Dendritic spines. *Front. Neural Circuits* **3**, 2 (2009).
37. Zheng, K. *et al.* Time-Resolved Imaging Reveals Heterogeneous Landscapes of Nanomolar Ca(2+) in Neurons and Astroglia. *Neuron* **88**, 277–288 (2015).

38. Marvin, J. S. *et al.* An optimized fluorescent probe for visualizing glutamate neurotransmission. *Nat. Methods* **10**, 162–170 (2013).
39. Rouach, N., Koulakoff, A., Abudara, V., Willecke, K. & Giaume, C. Astroglial metabolic networks sustain hippocampal synaptic transmission. *Science* **322**, 1551–1555 (2008).
40. Papouin, T., Dunphy, J. M., Tolman, M., Dineley, K. T. & Haydon, P. G. Septal Cholinergic Neuromodulation Tunes the Astrocyte-Dependent Gating of Hippocampal NMDA Receptors to Wakefulness. *Neuron* **94**, 840-854.e7 (2017).
41. Chever, O., Dossi, E., Pannasch, U., Derangeon, M. & Rouach, N. Astroglial networks promote neuronal coordination. *Sci. Signal.* **9**, ra6 (2016).
42. Han, Y. *et al.* Astrocyte-restricted disruption of connexin-43 impairs neuronal plasticity in mouse barrel cortex. *Eur. J. Neurosci.* **39**, 35–45 (2014).
43. Paukert, M. *et al.* Norepinephrine controls astroglial responsiveness to local circuit activity. *Neuron* **82**, 1263–1270 (2014).
44. Nimmerjahn, A., Mukamel, E. A. & Schnitzer, M. J. Motor behavior activates Bergmann glial networks. *Neuron* **62**, 400–412 (2009).
45. Ding, F. *et al.* α 1-Adrenergic receptors mediate coordinated Ca²⁺ signaling of cortical astrocytes in awake, behaving mice. *Cell Calcium* **54**, 387–394 (2013).
46. King, C. M. *et al.* Local resting ca²⁺ controls the scale of astroglial ca²⁺ signals. *Cell Rep.* **30**, 3466-3477.e4 (2020).
47. Rupprecht, P. *et al.* Centripetal integration of past events by hippocampal astrocytes and its regulation by the locus coeruleus.
<https://www.biorxiv.org/content/10.1101/2022.08.16.504030v2.full.pdf> (2023).

48. Gerstner, W., Lehmann, M., Liakoni, V., Corneil, D. & Brea, J. Eligibility Traces and Plasticity on Behavioral Time Scales: Experimental Support of NeoHebbian Three-Factor Learning Rules. *Front. Neural Circuits* **12**, 53 (2018).
49. Goldman, M. S., Compte, A. & Wang, X. J. Neural Integrator Models. in *Encyclopedia of Neuroscience* 165–178 (Elsevier, 2009). doi:10.1016/B978-008045046-9.01434-0.
50. Deemyad, T., Lüthi, J. & Spruston, N. Astrocytes integrate and drive action potential firing in inhibitory subnetworks. *Nat. Commun.* **9**, 4336 (2018).
51. Doron, A. *et al.* Hippocampal astrocytes encode reward location. *Nature* **609**, 772–778 (2022).
52. Mu, Y. *et al.* Glia Accumulate Evidence that Actions Are Futile and Suppress Unsuccessful Behavior. *Cell* **178**, 27-43.e19 (2019).
53. Arizono, M. *et al.* Structural basis of astrocytic Ca²⁺ signals at tripartite synapses. *Nat. Commun.* **11**, 1906 (2020).
54. Brunskine, C., Passlick, S. & Henneberger, C. Structural heterogeneity of the gabaergic tripartite synapse. *Cells* **11**, (2022).
55. Michaluk, P., Heller, J. P. & Rusakov, D. A. Rapid recycling of glutamate transporters on the astroglial surface. *eLife* **10**, (2021).
56. Batiuk, M. Y. *et al.* Identification of region-specific astrocyte subtypes at single cell resolution. *Nat. Commun.* **11**, 1220 (2020).
57. Bayraktar, O. A. *et al.* Astrocyte layers in the mammalian cerebral cortex revealed by a single-cell in situ transcriptomic map. *Nat. Neurosci.* **23**, 500–509 (2020).
58. Toyofuku, T. *et al.* Intercellular calcium signaling via gap junction in connexin-43-transfected cells. *J. Biol. Chem.* **273**, 1519–1528 (1998).

59. Venance, L., Stella, N., Glowinski, J. & Giaume, C. Mechanism involved in initiation and propagation of receptor-induced intercellular calcium signaling in cultured rat astrocytes. *J. Neurosci.* **17**, 1981–1992 (1997).
60. Khodakhah, K. & Ogden, D. Functional heterogeneity of calcium release by inositol trisphosphate in single Purkinje neurones, cultured cerebellar astrocytes, and peripheral tissues. *Proc Natl Acad Sci USA* **90**, 4976–4980 (1993).
61. Wiencken-Barger, A. E., Djukic, B., Casper, K. B. & McCarthy, K. D. A role for Connexin43 during neurodevelopment. *Glia* **55**, 675–686 (2007).
62. Yang, Y. *et al.* Molecular comparison of GLT1+ and ALDH1L1+ astrocytes in vivo in astroglial reporter mice. *Glia* **59**, 200–207 (2011).
63. Wang, Y. *et al.* SynQuant: an automatic tool to quantify synapses from microscopy images. *Bioinformatics* **36**, 1599–1606 (2020).
64. Dubbs, A., Guevara, J. & Yuste, R. moco: Fast Motion Correction for Calcium Imaging. *Front. Neuroinformatics* **10**, 6 (2016).
65. Fedchyshyn, M. J. & Wang, L.-Y. Activity-dependent changes in temporal components of neurotransmission at the juvenile mouse calyx of Held synapse. *J Physiol (Lond)* **581**, 581–602 (2007).
66. Martínez-Cagigal, V. Multiple Testing Toolbox, 1.1.0. MATLAB Central File Exchange <https://www.mathworks.com/matlabcentral/fileexchange/70604-multiple-testing-toolbox> (2021).
67. Groppe, D. fdr_bh, 2.3.0.0. MATLAB Central File Exchange https://www.mathworks.com/matlabcentral/fileexchange/27418-fdr_bh (2010).

68. Phipson, B. & Smyth, G. K. Permutation P-values should never be zero: calculating exact P-values when permutations are randomly drawn. *Stat. Appl. Genet. Mol. Biol.* **9**, Article39 (2010).
69. Seabold, S. & Perktold, J. Statsmodels: Econometric and Statistical Modeling with Python. in *Proceedings of the 9th Python in Science Conference* 92–96 (SciPy, 2010). doi:10.25080/Majora-92bf1922-011.
70. Virtanen, P. *et al.* SciPy 1.0: fundamental algorithms for scientific computing in Python. *Nat. Methods* **17**, 261–272 (2020).
71. Kingston, A. E. *et al.* LY341495 is a nanomolar potent and selective antagonist of group II metabotropic glutamate receptors. *Neuropharmacology* **37**, 1–12 (1998).

Chapter 4:

A Photoactivatable Norepinephrine for Probing Adrenergic Neural Circuits

Abstract

Norepinephrine (NE) is a critical neuromodulator that mediates a wide range of behavior and neurophysiology, including attention, arousal, plasticity, and memory consolidation. A major source of NE is the brainstem nucleus the locus coeruleus (LC), which sends widespread projections throughout the central nervous system (CNS). Efforts to dissect this complex noradrenergic circuitry have driven the development of many tools that detect endogenous NE or modulate widespread NE release via LC activation and inhibition. While these tools have enabled research that elucidates physiological roles of NE, additional tools to probe these circuits with a higher degree of spatial precision could enable a finer delineation of function. Here, we describe the synthesis and chemical properties of a photo-activatable NE, $[\text{Ru}(\text{bpy})_2(\text{PMe}_3)(\text{NE})]\text{PF}_6$ (RuBi-NE). We validate the one-photon (1P) release of NE using whole-cell patch clamp electrophysiology in acute mouse brain slices containing the LC. We show that a 10 ms pulse of blue light, in the presence of RuBi-NE, briefly modulates the firing rate of LC neurons via α -2 adrenergic receptors. The development of a photo-activatable NE that can be released with light in the visible spectrum provides a new tool for fine-grained mapping of complex noradrenergic circuits, as well as the ability to probe how NE acts on non-neuronal cells in the CNS.

Introduction

The neuromodulator norepinephrine (NE) plays fundamental roles in the nervous system by mediating attention¹⁻³, plasticity^{4,5}, and memory consolidation⁶. Further, an imbalance in NE levels has been implicated in both attention-deficit/hyperactivity disorder^{7,8} and depression⁹⁻¹¹. NE performs this wide range of neuromodulatory functions by acting on a number of receptors across diverse cell types in the central nervous system, including neurons, astrocytes, and microglia¹²⁻²⁰. Given both the fundamental roles of NE in the central nervous system (CNS) and the diversity of its cellular targets, tools to dissect this complex neuromodulatory system are critical to understand its many functions. A recent push to dissect noradrenergic circuit logic has led to the development of NE-based tools both to detect endogenous NE activity and to experimentally stimulate or inhibit NE release. Development of fluorescent sensors for NE, such as GRAB_{NE}²¹ and a carbon nanotube-based NE nanosensor²², allow for *in vivo* detection of endogenous NE release. In an effort to manipulate noradrenergic circuits, a number of groups have optogenetically activated or inhibited the locus coeruleus (LC) to either stimulate²³⁻²⁵ or inhibit^{23,26} NE release throughout the CNS. While optogenetic activation of the LC provides a physiologically relevant spatial pattern of release, this spatial pattern is inherently widespread, targeting many regions of the CNS²⁷⁻²⁹. Due to their highly collateralized nature, even targeted stimulation of a single axon or neuron may result in NE release across a relatively broad field^{29,30}. Additionally, it has been shown that LC neurons have the capacity to co-release dopamine along with NE³¹. Thus, to provide a tool to probe noradrenergic circuits with a higher degree of spatial precision and to isolate the specific action of NE on cells and circuits, we have developed a photoactivatable NE.

Photoactivatable compounds have proven to be powerful tools for mapping functional connectivity of GABAergic and glutamatergic circuits³²⁻³⁴, receptor localization³⁵, and locations of synaptic inputs onto subcellular compartments of neurons³⁶. A photoactivatable compound is a molecule “caged within” a protecting group that is released upon absorption of light. This reaction occurs quickly, and the amount of molecule released can be scaled by altering light intensity and beam size. Thus, photoactivatable compounds make it possible to release molecules in a temporally and spatially precise manner, without mechanically disturbing the preparation. A photoactivatable NE has previously been developed³⁷. However, it is activated by light in the UV spectrum, which can be damaging to, and have difficulty penetrating into, biological tissue. Thus, a new photoactivatable NE, activated by light in the visible spectrum, would greatly improve our ability to probe noradrenergic circuits in the same way that photoactivatable glutamate and GABA have enabled a detailed mapping of their respective circuits and receptors.

Ruthenium-bipyridine caged compounds were first presented two decades ago³⁸ as a new way to extend the activation spectrum to longer wavelengths. These cages are comprised of a ruthenium core coordinated to one or two bipyridines or analogue molecules, and one or two monodentate ligands. These complexes show a strong absorption in the visible region (usually blue-to-green), corresponding to a ¹MLCT charge transfer band³⁹. Upon irradiation of such band, in a fast sequence that occurs in tens of nanoseconds, a dissociative d-d state is populated, which leads to the release of one of the monodentate ligands, usually the molecule of interest. The remaining monodentate ligand can be used to tune the chemical and photochemical properties of the complex.

Here, we describe the synthesis and chemical properties of RuBi-NE, which releases NE upon absorption of visible light. Additionally, we demonstrate its use in a biological system by

modulating the firing rate of locus coeruleus (LC) neurons, neurons known to be autoregulated by NE^{40,41}. In the future, RuBi-NE allows for the stimulation of cells and circuits with NE in a spatially and temporally precise manner. Targeted release of NE will allow for a fine-grained mapping of the functional connectivity of noradrenergic circuits, as well as an ability to probe how NE acts on non-neuronal cells in the CNS. The ability to dissect noradrenergic circuits with this level of precision will help to move the field toward a deeper understanding of how NE performs its wide range of neuromodulatory functions.

Results

Although the synthesis of RuBi caged compounds is straightforward⁴², special care must be taken to obtain RuBi-NE, due to the tendency of free NE phenol groups to undergo oxidation in the basic media needed for coordination. Thus, the synthesis must be performed in deep anaerobic conditions using Schlenk procedures (see Methods). Once obtained, RuBi-NE is a stable solid that can be stored at room temperature, although a -15°C freezer is preferable for long-term storage. RuBi-NE is a +2 charged cation at low pH, although in physiological conditions its phenol groups can be partially deprotonated.

To confirm the biocompatibility of the RuBi-NE complex and evaluate its performance as a NE phototrigger, a series of electrophysiology experiments in acute brain slices containing LC were performed. First, we identified LC neurons for recording by crossing a mouse line that expresses Cre in LC neurons (*TH-Cre*) with a Cre-inducible fluorescent reporter line (*Ail4*) to drive expression of the red-shifted fluorescent molecule TdTomato specifically in LC neurons (Fig. 4.1a). These fluorescently labeled neurons exhibited the stereotypical large morphology of LC neuronal somata. Next, we targeted these cells for whole-cell patch-clamp recordings,

including Alexa dye in the pipette solution to confirm that the correct cell was patch-clamped (Fig. 4.1a). Patched cells were held in the current clamp configuration, and we observed that these neurons spontaneously fired action potentials (APs), as has been described previously^{43–46}. We took advantage of the fact that LC neurons themselves express α_2 adrenergic receptors (ARs), and NE activation of these receptors acts to inhibit AP firing of these cells⁴¹. We confirmed this cellular behavior by bathing the slice with 30 μ M NE, and observed a marked decrease in AP firing, as expected (Fig. 4.1b). We thus reasoned that any increase in NE at the patched cell would decrease AP firing.

To test whether photoactivation of RuBi-NE causes increased local NE, we added RuBi-NE to the bath in standard artificial cerebrospinal fluid (ACSF), without any additional NE. We first confirmed that RuBi-NE in the bath solution did not change cellular activity of the patched neuron, with AP firing rate unchanged between the two conditions (ACSF: 1.94 ± 0.31 spikes/s and RuBi-NE: 2.09 ± 0.10 spikes/s, $p = 0.60$, unpaired t-test). However, upon one-photon (1P) activation (10 ms) using 446–486 nm blue light, we observed a consistent decrease in AP firing rate (Fig. 4.1c, d [top], e [middle]), indicating that NE was indeed photoreleased. The blue light itself did not have any effect on AP firing, since the same effect was not observed when RuBi-NE was not added to the bath (Fig. 4.1e, left). Next, to confirm that the change in AP firing was due to release of NE and activation of ARs, we carried out the same 1P-photoactivation but added the α_2 AR antagonist (idazoxan, 2 μ M) to the bath along with RuBi-NE. Upon blue-light activation in these experiments, we no longer observed a change in AP firing (Fig. 4.1d [bottom], e [right]), although idazoxan itself increased firing rate, as previously^{43,47}. These data indicate that RuBi-NE photoactivation specifically increases local NE concentration.

To demonstrate the temporal dynamics of the NE photoactivation on LC neurons, we also calculated the interspike interval (ISI) between the APs occurring before and after the 10 ms blue-light pulse. When quantifying the ISI, we detected no significant difference among conditions before the blue light photoactivation (RuBi-NE: 0.5151 ± 0.0082 s, 0.4984 ± 0.007 s, ACSF: 0.5992 ± 0.0578 s, 0.6453 ± 0.0545 s and RuBi-NE + idazoxan: 0.3794 ± 0.1227 s, 0.3071 ± 0.0473 s, for each of the two ISIs, respectively, immediately preceding the light pulse), but a significant delay between spikes after the pulse with RuBi-NE in the bath compared to the ACSF condition (RuBi-NE: 5.1641 ± 0.7551 s, 9.2122 ± 0.8788 s, 2.45165 ± 0.1469 s, ACSF: 0.6735 ± 0.0454 s, 0.6549 ± 0.0424 s, 0.6708 ± 0.0516 s and RuBi-NE + idazoxan: 0.2201 ± 0.0109 s, 0.1901 ± 0.051 s, 0.2252 ± 0.0226 s, for each of the three ISIs respectively, including and immediately following the light pulse. Two-way ANOVA followed by Bonferroni test determine significant pairwise comparisons between conditions and ISIs; $p = 0.0492$ between RuBi-NE and ACSF between spikes 1:2 following the light pulse) (Fig. 4.1f, green). These ISI delays were not observed when the experiment was carried out in ACSF only (Fig. 4.1f, black), or when idazoxan was applied to the bath with RuBi-NE (Fig. 4.1f, pink). Similarly, when we quantify the absolute time of each AP from the light pulse, we find that a 10 ms photo-release of RuBi-NE significantly delays the firing of subsequent APs, such that the second and third AP after the light pulse occurs 14.0546 ± 0.9813 s and 16.47 ± 1.0317 s after the light stimulation (Fig. 4.1g, green), while the control APs after the pulse occurred at 1.05 ± 0.0603 s and 1.73 ± 0.1042 s, and 0.3068 ± 0.1407 s and 0.53 ± 0.1633 s (Fig. 4.1g, black and pink, respectively, two-way ANOVA followed by Bonferroni test determine significant pairwise comparisons between conditions and APs; $p = 0.0044$ and $p = 0.00040$ between RuBi-NE and ACSF at spike +2 and +3, respectively). In all, these data indicate that RuBi-NE acts as a robust, specific phototrigger for NE.

Discussion

Here, we introduce the development of $[\text{Ru}(\text{bpy})_2(\text{PMe}_3)(\text{Norepinephrine})]^{n+}$ (RuBi-NE), a photoactivatable NE releasable with light in the visible spectrum. We validate the release of NE with one-photon uncaging in acute mouse brain slices containing the LC. We find that uncaging RuBi-NE, with a brief pulse of blue light, temporarily slows the rate of LC action potentials via α -2 adrenergic receptors. This new tool will allow for the temporally and spatially precise release of NE without mechanical disturbance of tissue, which itself can modulate cellular activity⁴⁸.

Our validation of 1P NE uncaging releases NE over a large field-of-view, the size of the uncaging light beam. This widespread release of NE is physiologically relevant given the extensive projections of LC neurons throughout the brain, which release NE via volume transmission^{49,50}. While this spatially diffuse uncaging allows for investigation of the specific action of NE isolated from any potential co-release from synaptic terminals, validation of the two-photon compatibility of RuBi-NE, as demonstrated for other RuBi subtypes^{51,52}, will be needed to map noradrenergic circuitry with subcellular spatial precision. Synthesis and validation of this photoactivatable compound adds NE to the suite of neurotransmitters and neuromodulators that can now be caged within a ruthenium-bipyridine backbone, expanding the toolkit available to map functional circuitry and receptor localization of neuronal and non-neuronal cells in the central nervous system.

Methods

RuBi-NE synthesis

All chemicals were purchased from Sigma-Aldrich and used as received without further purification. Ru(bpy)₂Cl₂ was synthesized according to literature⁵³. From this, [Ru(bpy)₂(PMe₃)(Cl)]PF₆ was obtained as previously described⁵⁴. For synthesis of [Ru(bpy)₂(PMe₃)(Norepinephrine)]²⁺, 300 mg of [Ru(bpy)₂(PMe₃)(Cl)]PF₆ was dissolved in 3 ml acetone and 15 ml water was added. The mixture was stirred overnight with mesylate-loaded Dowex-22 ion exchange resin. After evaporation of acetone, the resultant solution of [Ru(bpy)₂(PMe₃)(H₂O)]Mes₂ was separated from the resin. From this point all procedures were performed under N₂, with the solution previously degassed with Ar or N₂. 450 mg of norepinephrine hydrochloride was introduced into a Schlenk flask, and the pH was raised to 9–10 by adding 2 mL of 1 M NaOH. When the formation of the NE complex was confirmed by UV-visible spectroscopy, the mixture was cooled in an ice bath, and 1 M acetic acid was added to lower the pH and prevent possible oxidation of NE by air during the subsequent procedures. The solution was filtered, and after the addition of 2 mL of 0.5 M KPF₆, the complex [Ru(bpy)₂(PMe₃)(NE)](PF₆)₂ precipitated as an orange powder. For a more soluble preparation, a further ion-exchange with mesylate-loaded Dowex 22 resin can be made.

Slicing and electrophysiology

Horizontal brain slices (350 μm) at the level of the pons in the brainstem containing the LC were prepared from P28–P34 TH-Cre⁺; Ai14⁺ and TH-Cre⁺; Ai9^{+/-} female mice using a vibratome (VT1200; Leica). Slicing solution was chilled at -20°C and contained (in mM): 222 sucrose, 27 NaHCO₃, 2.6 KCl, 2 MgSO₄, 2 CaCl₂, 1.5 NaH₂PO₄, bubbled with 95% O₂/ 5% CO₂. Slices were

incubated in artificial cerebrospinal fluid (ACSF) at 35°C for 30 min and then held at room temperature until the time of recording. Recording ACSF contained (in mM): 123 NaCl, 26 NaHCO₃, 10 dextrose, 3 KCl, 2 MgSO₄, 2 CaCl₂, 1 NaH₂PO₄, bubbled with 95% O₂/5% CO₂.

Neurons were visualized using DODT contrast microscopy on an upright microscope (Bruker) and fluorescently labeled tdTomato-positive LC neurons were identified using an EXFO X-Cite 120 epifluorescent lamp (Excelitas) coupled to a red filter cube (TRITC-B-000, Semrock). Neurons were visualized using a NIR Apo 40X/0.80W objective (Nikon) and an infrared CCD real-time camera (IR-2000, DAGE-MTI). Recordings were made using a Multiclamp 700B (Molecular Devices) amplifier and acquired at a rate of 10 kHz with Prairie View 5.4 software. Patch pipettes (6–7 MΩ tip resistance, borosilicate glass, outer diameter 1.5 mm, inner diameter 0.86 mm, Sutter Instruments) were filled with the following internal solution (in mM): 135 K-methylsulfate, 10 KCl, 10 HEPES, 5 NaCl, 0.025 Alexa 594, pH 7.3 (adjusted with KOH). Series resistance ranged between 15–30 MΩ, and pipette capacitance was compensated. Neurons were recorded in current clamp configuration. With no injected current, neurons had a resting membrane potential (V_m) ~ -50mV.

RuBi-NE uncaging

Once the neuron was in whole-cell patch clamp configuration, all lights were turned off and a stock solution of 10mg/mL RuBi-NE in ACSF was added to the bath solution for a final RuBi-NE concentration of 300 μM. While recording, RuBi-NE was photolyzed by 1P excitation with a single 10 ms pulse of blue light (446–486 nm) using an EXFO X-Cite 120 epifluorescent lamp (Excelitas) coupled with a 466/40 nm single-band bandpass filter (BrightLine, Semrock) at an approximate power of 14.3mW. Idazoxan hydrochloride (Sigma Aldrich, 2 μM) was added to the

ACSF bath solution to confirm that RuBi-NE was acting on the neurons via α_2 adrenergic receptors.

Statistics

Averages are reported as mean \pm SEM. Average firing rates before the light pulse were calculated by taking the mean firing rate across pulses. An unpaired t-test was used to calculate the p-value to compare the average firing rate before the light pulse between the ACSF and RuBi-NE conditions. The remaining p-values were calculated using two-way ANOVAs followed by Bonferroni tests determine significant pairwise comparisons between conditions and time points.

Figures

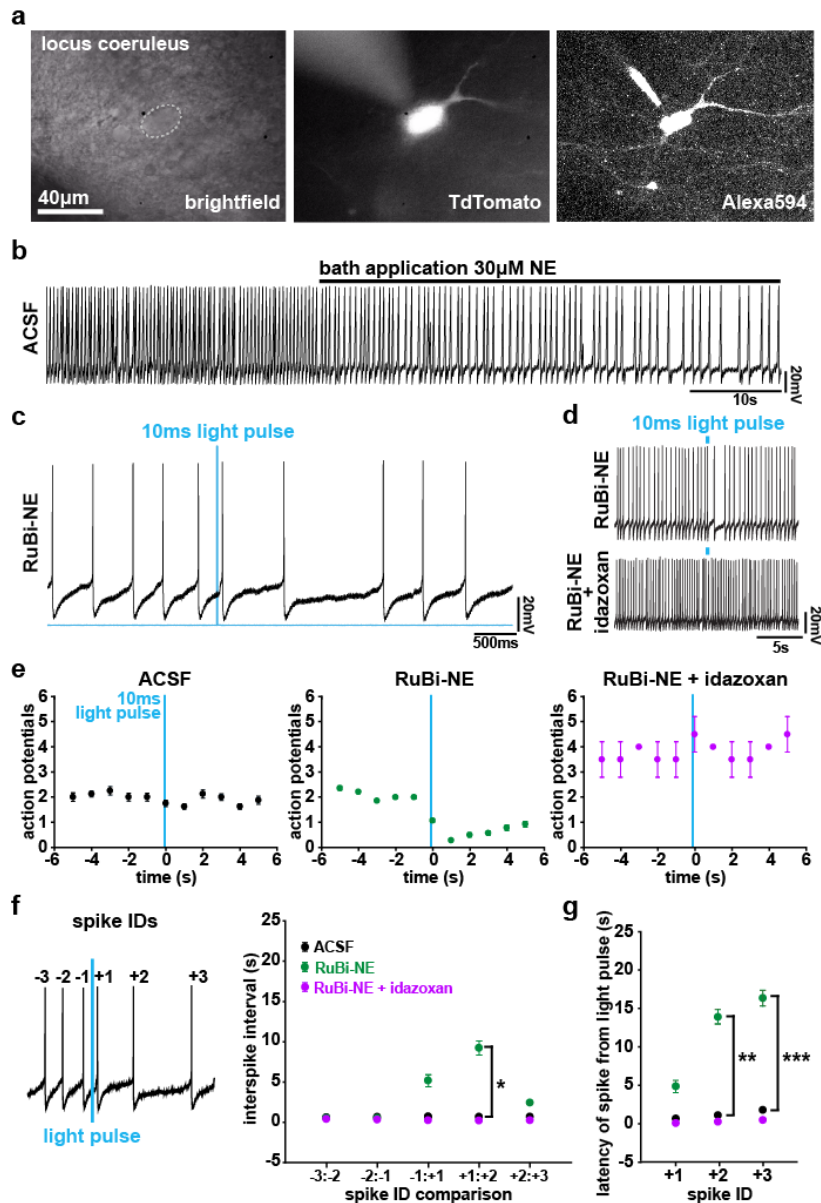


Figure 4.1: Photorelease of RuBi-NE specifically increases local [NE].

(a) Representative image of a LC neuron identified for recording. Left: DODT contrast image of an LC neuron before recording; dotted line marks soma. Center: 1P image of tdTomato⁺ LC neuron before whole-cell patch-clamp configuration. Right: 2P image of the same LC neuron in whole-cell patch-clamp configuration, dialyzed with Alexa 594. Patch pipette shown on the upper left border of the cell. (b) Representative trace of spontaneous AP firing pattern of LC neuron in current clamp configuration. Bath application of NE (30 µM) occurs 30 s into the trace (black bar). (c) Representative activity of an LC neuron before and after uncaging RuBi-NE. Blue line marks 10 ms blue-light uncaging pulse. (d) Zoomed out representative activity before and after RuBi-NE uncaging before (top) and during (bottom) blockade of α_2 ARs with idazoxan

Figure 4.1 continued on next page

Figure 4.1 continued

(2 μ M). Blue rectangles mark 10 ms blue-light pulse. (e) Average APs/s for an LC neuron in ACSF (n = 8 pulses in 2 cells, left), in 300 μ M RuBi-NE (n = 14 pulses in 4 cells, center), and in 300 μ M RuBi-NE + 2 μ M idazoxan (n = 2 pulses in 1 cell, right). *Time 0* denotes the second in which the light pulse occurred. (f) Left: Example trace showing spike IDs relative to the light pulse. Right: Average ISI calculated for LC neurons in ACSF (n = 8 pulses in 2 cells), RuBi-NE (n = 14 pulses in 4 cells) and RuBi-NE + idazoxan (n = 2 pulses in 1 cell). *-1:+1* is the ISI during which uncaging occurs. Two-way ANOVA grouped by condition and ISI number followed by Bonferroni test to determine significant pairwise comparisons, * p < 0.05. (g) Average absolute time of the first three spikes following blue-light pulse in ACSF, RuBi-NE, and RuBi-NE + idazoxan. Two-way ANOVA grouped by condition and spike number followed by Bonferroni test to determine significant pairwise comparisons, ** p < 0.01 and *** p < 0.001.

References

1. Aston-Jones, G. Behavioral functions of locus coeruleus derived from cellular attributes. *Psychobiology* **13**, 118–126 (1985).
2. Coull, J. T., Büchel, C., Friston, K. J. & Frith, C. D. Noradrenergically mediated plasticity in a human attentional neuronal network. *Neuroimage* **10**, 705–715 (1999).
3. Mair, R. D., Zhang, Y., Bailey, K. R., Toupin, M. M. & Mair, R. G. Effects of clonidine in the locus coeruleus on prefrontal- and hippocampal-dependent measures of attention and memory in the rat. *Psychopharmacology (Berl)* **181**, 280–288 (2005).
4. Gelinas, J. N. & Nguyen, P. V. Beta-adrenergic receptor activation facilitates induction of a protein synthesis-dependent late phase of long-term potentiation. *J. Neurosci.* **25**, 3294–3303 (2005).
5. Straube, T., Korz, V., Balschun, D. & Frey, J. U. Requirement of beta-adrenergic receptor activation and protein synthesis for LTP-reinforcement by novelty in rat dentate gyrus. *J Physiol (Lond)* **552**, 953–960 (2003).
6. Gibbs, M. E., Hutchinson, D. S. & Summers, R. J. Noradrenaline release in the locus coeruleus modulates memory formation and consolidation; roles for α - and β -adrenergic receptors. *Neuroscience* **170**, 1209–1222 (2010).
7. Spencer, T. *et al.* Effectiveness and tolerability of tomoxetine in adults with attention deficit hyperactivity disorder. *Am. J. Psychiatry* **155**, 693–695 (1998).
8. Palumbo, D. R. *et al.* Clonidine for attention-deficit/hyperactivity disorder: I. Efficacy and tolerability outcomes. *J. Am. Acad. Child Adolesc. Psychiatry* **47**, 180–188 (2008).
9. Maan, J. S., Rosani, A. & Saadabadi, A. Desipramine. in *StatPearls* (StatPearls Publishing, 2023).

10. Weinshenker, D., White, S. S., Javors, M. A., Palmiter, R. D. & Szot, P. Regulation of norepinephrine transporter abundance by catecholamines and desipramine in vivo. *Brain Res.* **946**, 239–246 (2002).
11. Simson, P. E. & Weiss, J. M. Altered activity of the locus coeruleus in an animal model of depression. *Neuropsychopharmacology* **1**, 287–295 (1988).
12. Devilbiss, D. M. & Waterhouse, B. D. Norepinephrine exhibits two distinct profiles of action on sensory cortical neuron responses to excitatory synaptic stimuli. *Synapse* **37**, 273–282 (2000).
13. Bevan, P., Bradshaw, C. M. & Szabadi, E. The pharmacology of adrenergic neuronal responses in the cerebral cortex: evidence for excitatory alpha- and inhibitory beta-receptors. *Br. J. Pharmacol.* **59**, 635–641 (1977).
14. Frohman, E. M., Vayuvegula, B., Gupta, S. & van den Noort, S. Norepinephrine inhibits gamma-interferon-induced major histocompatibility class II (Ia) antigen expression on cultured astrocytes via beta-2-adrenergic signal transduction mechanisms. *Proc Natl Acad Sci USA* **85**, 1292–1296 (1988).
15. Bekar, L. K., He, W. & Nedergaard, M. Locus coeruleus alpha-adrenergic-mediated activation of cortical astrocytes in vivo. *Cereb. Cortex* **18**, 2789–2795 (2008).
16. Mori, K. *et al.* Effects of norepinephrine on rat cultured microglial cells that express $\alpha 1$, $\alpha 2$, $\beta 1$ and $\beta 2$ adrenergic receptors. *Neuropharmacology* **43**, 1026–1034 (2002).
17. Tanaka, K. F. Existence of Functional Beta1- and Beta2-Adrenergic Receptors on Microglia. *Journal of Neuroscience Research* (2002).

18. Heneka, M. T. *et al.* Locus ceruleus controls Alzheimer's disease pathology by modulating microglial functions through norepinephrine. *Proc Natl Acad Sci USA* **107**, 6058–6063 (2010).
19. Reitman, M. E. *et al.* Norepinephrine links astrocytic activity to regulation of cortical state. *Nat. Neurosci.* **26**, 579–593 (2023).
20. Lu, T.-Y. *et al.* Norepinephrine modulates calcium dynamics in cortical oligodendrocyte precursor cells promoting proliferation during arousal in mice. *Nat. Neurosci.* **26**, 1739–1750 (2023).
21. Feng, J. *et al.* A genetically encoded fluorescent sensor for rapid and specific in vivo detection of norepinephrine. *Neuron* **102**, 745-761.e8 (2019).
22. Beyene, A. G. *et al.* Ultralarge Modulation of Fluorescence by Neuromodulators in Carbon Nanotubes Functionalized with Self-Assembled Oligonucleotide Rings. *Nano Lett.* **18**, 6995–7003 (2018).
23. Carter, M. E. *et al.* Tuning arousal with optogenetic modulation of locus coeruleus neurons. *Nat. Neurosci.* **13**, 1526–1533 (2010).
24. Wang, X., Piñol, R. A., Byrne, P. & Mendelowitz, D. Optogenetic stimulation of locus ceruleus neurons augments inhibitory transmission to parasympathetic cardiac vagal neurons via activation of brainstem $\alpha 1$ and $\beta 1$ receptors. *J. Neurosci.* **34**, 6182–6189 (2014).
25. Quinlan, M. A. L. *et al.* Locus Coeruleus Optogenetic Light Activation Induces Long-Term Potentiation of Perforant Path Population Spike Amplitude in Rat Dentate Gyrus. *Front. Syst. Neurosci.* **12**, 67 (2018).

26. Janitzky, K. *et al.* Optogenetic silencing of locus coeruleus activity in mice impairs cognitive flexibility in an attentional set-shifting task. *Front. Behav. Neurosci.* **9**, 286 (2015).
27. Loughlin, S. E., Foote, S. L. & Bloom, F. E. Efferent projections of nucleus locus coeruleus: topographic organization of cells of origin demonstrated by three-dimensional reconstruction. *Neuroscience* **18**, 291–306 (1986).
28. Loughlin, S. E., Foote, S. L. & Grzanna, R. Efferent projections of nucleus locus coeruleus: morphologic subpopulations have different efferent targets. *Neuroscience* **18**, 307–319 (1986).
29. Levitt, P. & Moore, R. Noradrenaline neuron innervation of the neocortex in the rat. *Brain Res* **139**, 219–231 (1978).
30. Descarries, L., Watkins, K. & Lapierre, Y. Noradrenergic axon terminals in the cerebral cortex of rat. III. Topometric ultrastructural analysis. *Brain Res* **133**, 197–222 (1977).
31. Kempadoo, K. A., Mosharov, E. V., Choi, S. J., Sulzer, D. & Kandel, E. R. Dopamine release from the locus coeruleus to the dorsal hippocampus promotes spatial learning and memory. *Proc Natl Acad Sci USA* **113**, 14835–14840 (2016).
32. Callaway, E. M. & Katz, L. C. Photostimulation using caged glutamate reveals functional circuitry in living brain slices. *Proc Natl Acad Sci USA* **90**, 7661–7665 (1993).
33. Dantzker, J. L. & Callaway, E. M. Laminar sources of synaptic input to cortical inhibitory interneurons and pyramidal neurons. *Nat. Neurosci.* **3**, 701–707 (2000).
34. Nikolenko, V., Poskanzer, K. E. & Yuste, R. Two-photon photostimulation and imaging of neural circuits. *Nat. Methods* **4**, 943–950 (2007).

35. Pettit, D. L., Wang, S. S., Gee, K. R. & Augustine, G. J. Chemical two-photon uncaging: a novel approach to mapping glutamate receptors. *Neuron* **19**, 465–471 (1997).
36. Kwon, T. *et al.* Ultrastructural, molecular and functional mapping of gabaergic synapses on dendritic spines and shafts of neocortical pyramidal neurons. *Cereb. Cortex* **29**, 2771–2781 (2019).
37. Fernandes, M. J. G., Costa, S. P. G. & Gonçalves, M. S. T. Synthesis and light triggered release of catecholamines from pyrenylmethyl carbamate cages. *New J. Chem* **37**, 2369 (2013).
38. Zayat, L., Calero, C., Alborés, P., Baraldo, L. & Etchenique, R. A new strategy for neurochemical photodelivery: metal-ligand heterolytic cleavage. *J. Am. Chem. Soc.* **125**, 882–883 (2003).
39. Pinnick, D. V. & Durham, B. Photosubstitution reactions of Ru(bpy)₂XYn⁺ complexes. *Inorg. Chem.* **23**, 1440–1445 (1984).
40. Egan, T. M., Henderson, G., North, R. A. & Williams, J. T. Noradrenaline-mediated synaptic inhibition in rat locus coeruleus neurones. *J Physiol (Lond)* **345**, 477–488 (1983).
41. Svensson, T. H., Bunney, B. S. & Aghajanian, G. K. Inhibition of both noradrenergic and serotonergic neurons in brain by the alpha-adrenergic agonist clonidine. *Brain Res.* **92**, 291–306 (1975).
42. Filevich, O. & Etchenique, R. Photochemical biosignaling with ruthenium complexes. in *Advances in inorganic chemistry* vol. 80 321–354 (Elsevier, 2022).

43. Simson, P. E. Blockade of α_2 -adrenergic Receptors Markedly Potentiates Glutamate-evoked Activity of Locus Coeruleus Neurons. *International Journal of Neuroscience* **106**, 95–99 (2001).
44. Andrade, R., Vandermaelen, C. P. & Aghajanian, G. K. Morphine tolerance and dependence in the locus coeruleus: single cell studies in brain slices. *Eur. J. Pharmacol.* **91**, 161–169 (1983).
45. Andrade, R. & Aghajanian, G. K. Locus coeruleus activity in vitro: intrinsic regulation by a calcium-dependent potassium conductance but not alpha 2-adrenoceptors. *J. Neurosci.* **4**, 161–170 (1984).
46. Williams, J. T., Egan, T. M. & North, R. A. Enkephalin opens potassium channels on mammalian central neurones. *Nature* **299**, 74–77 (1982).
47. Simson, P. E. & Weiss, J. M. Alpha-2 receptor blockade increases responsiveness of locus coeruleus neurons to excitatory stimulation. *J. Neurosci.* **7**, 1732–1740 (1987).
48. Charles, A. Intercellular calcium waves in glia. *Glia* **24**, 39–49 (1998).
49. Beaudet, A. & Descarries, L. The monoamine innervation of rat cerebral cortex: synaptic and nonsynaptic axon terminals. *Neuroscience* **3**, 851–860 (1978).
50. Agnati, L. F., Zoli, M., Strömberg, I. & Fuxe, K. Intercellular communication in the brain: wiring versus volume transmission. *Neuroscience* **69**, 711–726 (1995).
51. Fino, E. *et al.* RuBi-Glutamate: Two-Photon and Visible-Light Photoactivation of Neurons and Dendritic spines. *Front. Neural Circuits* **3**, 2 (2009).
52. Araya, R., Andino-Pavlovsky, V., Yuste, R. & Etchenique, R. Two-photon optical interrogation of individual dendritic spines with caged dopamine. *ACS Chem. Neurosci.* **4**, 1163–1167 (2013).

53. Viala, C. & Coudret, C. An expeditious route to cis-Ru(bpy)₂C12 (bpy=2,2'-bipyridine) using carbohydrates as reducers. *Inorg. Chim. Acta* **359**, 984–989 (2006).
54. Salierno, M., Marceca, E., Peterka, D. S., Yuste, R. & Etchenique, R. A fast ruthenium polypyridine cage complex photoreleases glutamate with visible or IR light in one and two photon regimes. *J. Inorg. Biochem.* **104**, 418–422 (2010).

Publishing Agreement

It is the policy of the University to encourage open access and broad distribution of all theses, dissertations, and manuscripts. The Graduate Division will facilitate the distribution of UCSF theses, dissertations, and manuscripts to the UCSF Library for open access and distribution. UCSF will make such theses, dissertations, and manuscripts accessible to the public and will take reasonable steps to preserve these works in perpetuity.

I hereby grant the non-exclusive, perpetual right to The Regents of the University of California to reproduce, publicly display, distribute, preserve, and publish copies of my thesis, dissertation, or manuscript in any form or media, now existing or later derived, including access online for teaching, research, and public service purposes.

DocuSigned by:

Michelle Kimberly Cahill

9B1C2462F32D46E...

Author Signature

12/5/2023

Date